Towards Broadband Communication at 300 GHz in Silicon

Thesis submitted for the degree of
Doktor der Ingenierwissenschaften

at the
University of Wuppertal, Germany
School of Electrical, Information and Media Engineering

by

Thomas Bücher
from Wuppertal, Germany

January 2024

Contents

List of Figures iv

List of Tables viii

List of Abbreviations x

Declaration xii

Acknowledgements xiii

Publications xv

Contribution of others xvii

Abstract xviii

Zusammenfassung xx

1 Introduction 1

1.1 Towards a New Generation . . . 3
1.2 State-of-the-Art . . . 6
1.3 This dissertation . . . 8
1.3.1 Central Research Questions . . . 8
1.3.2 Original Contributions . . . 9
1.3.3 Thesis Structure . . . 10

2 Theoretical Background 11

2.1 Communication . . . 11
2.1.1 Bandwidth . . . 12
2.1.2 Analog Modulation . . . 12
2.1.3 Digital Modulation . . . 13
2.1.4 Pulse Shaping . . . 13
2.1.5 Eye Diagram . . . 14

2.1.6 Error Vector Magnitude . . . 15
2.1.7 Architectures . . . 18
2.1.8 Amplifier-First vs. Mixer-First Receiver . . . 19
2.2 Propagation in Guided Media . . . 20
2.2.1 Single-ended Signaling . . . 21
2.2.2 Differential Signaling . . . 21
2.2.2.1 Even and Odd Mode . . . 22
2.3 Propagation in Unguided Media . . . 23
2.3.1 Polarization . . . 24
2.4 SiGe BiCMOS . . . 26
2.5 Summary and Conclusion . . . 28

3 Broadband Building Blocks 29
3.1 Receiver & Transmitter Implementation . . . 29
3.2 Antenna . . . 32
3.3 Up-/ Downconversion . . . 34
3.3.1 Upconversion . . . 34
3.3.2 Downconversion . . . 38
3.4 RF Power Amplifiers . . . 46
3.4.1 Transformer-based Matching Networks . . . 50
3.4.2 Power Amplifier Measurement . . . 53
3.5 Frequency Generation . . . 57
3.5.1 Phase shifter . . . 61
3.6 Summary and Conclusion . . . 65

4 Packaging 68
4.1 PCB Design . . . 69
4.1.1 Bonding Area . . . 71
4.1.2 Coupled Line Decoupling . . . 73
4.1.3 Connector . . . 74
4.2 Impairements . . . 76
4.2.1 Surface Roughness . . . 76
4.2.2 Surface Finish . . . 77
4.3 Measurement . . . 81
4.4 Summary and Conclusion . . . 84

5 Dual-Polarization MIMO 86
5.1 Antenna Measurement . . . 87
5.2 Receiver . . . 90
5.2.1 Conversion Gain . . . 90
5.2.1.1 RF/LO Bandwidth . . . 90

5.2.1.2 RF/IF Bandwidth 91
5.2.2 Noise Figure 94
5.2.3 IQ Imbalance of the Receiver 96
5.3 Transmitter 98
5.3.1 Compression 98
5.3.1.1 Harmonic Distortion 100
5.3.2 Single Sideband Measurement 102
5.3.3 Harmonic Suppression 110
5.3.4 Group Delay 111
5.4 Power Consumption 112
5.5 Summary and Conclusion 113

6 Back-to-Back Communication 116
6.1 RF Characterization 117
6.2 Link Measurements 118
6.3 Undesired Mixing 125
6.4 Summary and Conclusion 127

7 Conclusions and Outlook 129
7.1 Conclusion 129
7.2 Outlook 131
7.2.1 Short-term outlook 131
7.2.2 Long-term outlook 132

Bibliography 135

List of Figures

1.1 Number of mobile mubscriptions 2
1.2 Mobile traffic data projection up to 2029 2
1.3 Requirements for 6G 3
1.4 Atmospheric attenuation over frequency 4
1.5 Timeline for 6G 5
1.6 State of the art of Power amplifiers until 2017 6

2.1 Eye diagram explanation 15
2.2 Ideal constellation diagram of QPSK 16
2.3 Super heterodyne receiver block diagram 18
2.4 Direct conversion receiver block diagram 19
2.5 Single-ended and differential signaling 20
2.6 Microstrip and coplanar waveguide transmission line 22
2.7 Depiction of Even and Odd Mode Excitation 22
2.8 3 different types of polarized waves 24
2.9 Simulated G_{max} 27

3.1 Block diagram of the receiver 30
3.2 Layout of the dual polarized receiver 30
3.3 Block diagram of the transmitter 31
3.4 Layout of the dual-polarized transmitter 31
3.5 Antenna micrograph 32
3.6 Layout of the three-port Hybrid 33
3.7 Simulation Results of the three-port Hybrid 34
3.8 Schematic of the upconversion mixer 35
3.9 Micrograph of the complete upconversion stage 36
3.10 Gysel power combiner layout. 37
3.11 Gysel power combiner insertion loss and return loss 37
3.12 Schematic of the downconversion mixer 38
3.13 Micrograph of the downconversion stage 39

3.14 Schematic of the implemented TIA 40
3.15 Simulated normalized TIA conversion gain 41
3.16 Insertion loss and phase of the implemented TIA output baseband routing 42
3.17 HFSS View of the cheezed groundplane above the baseband routing . . 43
3.18 Insertion loss and phase of the optimized TIA output baseband routing 44
3.19 Phase difference comparison of the baseband routing 45
3.20 Simulation results of improved transimpedance amplifier 45
3.21 Block diagram and chip micrograph of the 3-stage power amplifier . . . 47
3.22 Full cascode layout 48
3.23 Simulated input S_{11} and output S_{22} for ideal, layout-including and large-signal simulation 49
3.24 Simulation model of the input transformer in the power amplifier . . . 52
3.25 A simplified coupled-line model of the transformer 52
3.26 Simulated S-Parameters of the input iransformer 53
3.27 Measurement setup for both small-signal and large-signal measurements 53
3.28 Measured and simulated small-signal S-parameters of the presented PA 54
3.29 Measured group delay of the amplifier 55
3.30 Large-Signal measurement results at 270 GHz 55
3.31 Saturated output power over frequency 56
3.32 Block diagram of the x9 frequency multiplier 59
3.33 Measurement and simulation results of the frequency multiplier breakout 60
3.34 Schematic of the phase shifter 62
3.35 Chip micrograph of the phase shifter 63
3.36 Measurement results of the phase shifter 63
3.37 Polar constellation Diagram of the phase shifter 64
3.38 Measured group delay of the phase shifter 65

4.1 Lens assembly 69
4.2 HFSS model of baseband section 71
4.3 S-Parameters of bonding area 72
4.4 HFSS model of the differential baseband section 73
4.5 Simulation results of the mode decoupling section 74
4.6 Solderless 2.92 mm connector 74
4.7 Measured and simulated baseband connector response 75
4.8 Measured return loss of the Local Oscillator (LO) feed 76
4.9 Insertion loss of coupled lines with and without surface roughness . . . 77
4.10 Cross section of ENEPIG and DIG surface finish 78
4.11 Skin effect in the PCB trace 78
4.12 Skin depth in PCB materials 79
4.13 Insertion loss dependence on surface finish and surface roughness 80

4.14 PCB test structure 81
4.15 Simulation results of the microstrip test structure 82
4.16 Measured return loss of the single-ended microstrip using short and load termination 82
4.17 Measured insertion loss of the microstrip test structure 83

5.1 Measurement setup for the radiation pattern measurement 87
5.2 Measured radiation pattern at 270 GHz for the both projections 88
5.3 Superposition of the radiation patterns in both projections 89
5.4 Measured antenna directivity for both Transmitter (TX) and Receiver (RX) 89
5.5 Harmonic mixing products of the RX 91
5.6 Conversion gain of the receiver at different LO frequencies 92
5.7 Conversion gain of the receiver at 250 and 260 GHz 93
5.8 Block diagram for noise figure extraction 94
5.9 Single sideband noise figure of the receiver 95
5.10 IF frequency dependent IQ imbalance of the receiver 96
5.11 LO frequency dependent IQ imbalance of the receiver 97
5.12 Large signal Mmasurement results of the at 255 and 260 GHz 99
5.13 Simulated single mixer compression at 260 GHz 100
5.14 Simulated single mixer compression at 260 GHz for artifical mismatch . 101
5.15 IQ imbalance of the TX 104
5.16 Sideband asymmetry of the TX 105
5.17 Conversion gain with constant IF frequency of 2 GHz for SSB and DSB operation 106
5.18 Saturated output Power with constant IF frequency of 2 GHz for SSB and DSB operation 107
5.19 Saturated output power over frequency in SSB operation 107
5.20 Conversion gain of the TX at 250 and 260 GHz 108
5.21 Saturated output power at 270 GHz 109
5.22 Input referred compression point of the transmitter 109
5.23 Upconverted SSB signals for an IF frequency of 33 MHz and varying LO frequency 110
5.24 LO leakage of the different LO harmonics present in the TX 111

6.1 Communication measurement setup 116
6.2 Normalized gain for different LO frequencies 118
6.3 Communication measurement setup 119
6.4 EVM for BPSK modulation 120
6.5 SNR for BPSK modulation 121
6.6 Measured eye diagram at 260 GHz at different data rates 122

6.7 EVM over LO frequency for different symbol rates in QPSK and BPSK 123
6.8 Measured eye diagram at 260 GHz at different data rates in QPSK . . 124

List of Tables

1.1 Silicon based power amplifiers above 200 GHz in silicon technology. . . 7
1.2 Wireless links above 200 GHz in silicon technology 7

5.1 Conversion gain for different LO frequencies in the receiver 93
5.2 Receiver operating above 200 GHz in Silicon 114
5.3 Transmitter operating above 200 GHz in Silicon 115

6.1 Wireless links above 200 GHz in silicon technology 128

List of Abbreviations

5G fifth-generation technology standard for broadband cellular networks introduced in 2019

AC Alternating current

AWG Arbitrary Wave Generator

BiCMOS Bipolar CMOS

BPSK Binary Phase-Shift Keying

CB Common Base

CC Common Collector

CE Common Emitter

CG Conversion Gain

CPW CoPlanar Waveguide

DC Direct current

DIG Direct Immersion Gold

DSB Double Sideband

DUT Device under Test

ENEPIG Electroless Nickel Electroless Palladium Immersion Gold

ENIG Electroless Nickel Immersion Gold

EVM Error Vector Magnitude

GSM Global System for Mobile Communications

HBT heterojunction bipolar transistor

HD Harmonic Distortion

I In-phase

IF intermediate frequency

IM Intermodulation

ISIG Immersion Silver and Immersion Gold

LO Local Oscillator

LSB Lower Side Band

MIMO multiple-input and multiple-output

MOS metal-oxide-semiconductor

PCB Printed Circuit Board

PLL Phase-locked loop

Q Quadrature

QPSK Quadrature Phase-Shift Keying

RF Radio Frequency

RX Receiver

SiGe Silicon germanium

SNR signal-to-noise

SSB Single Sideband

THz Terahertz

TIA Transimpedance Amplifier

TX Transmitter

USB Upper Side Band

Declaration

I, Thomas Bücher, herewith declare that I have produced this thesis without the prohibited assistance of third parties and without making use of aids other than those specified; notions taken over directly or indirectly from other sources have been identifed as such. This work has not previously been presented in identical or similar form to any other German or foreign examination board.

The thesis work was conducted from 2017 to 2023 under the supervision of Prof. Dr. rer. nat. Ullrich R. Pfeiffer at the University of Wuppertal. This work was partially funded by the Bundesministerium für Bildung und Forschung (BMBF) as part of the *Verbundprojekt Elektroniksysteme für Radar- und Kommunikationslösungen der nächsten Generation - TARANTO - TowARds Advanced bicmos NanoTechnology platforms for rf to thz applicatiOns*, and through the Project *THz circuits and systems in ultra-fast SiGe HBT technologies (DotSeven2IC)* funded by the German Research Foundation (DFG).

Wuppertal, January 2024

Acknowledgements

First and foremost, I would like to express my gratitude towards my Ph.D. advisor, Prof. Dr. rer. nat. Ullrich Pfeiffer. Having graduated at a different university, he gave me the opportunity to further pursue my academic career and opened up the door to many opportunities from access to numerous silicon technology to measuring circuits at the highest level in a well equipped laboratory and also trusting me to teach students and show them the ropes of RF engineering. This research would not have been possible without his continuous support and guidance.

Furthermore, I would like to thank Dr. Janusz Grzyb for the opportunities to pick his brain and tap into the endless fountain of knowledge. His sharpness and accuracy in every facet of engineering kept me on my toes to finish this research. In addition, special thanks goes to Professor Patrick Reynaert for taking his time and effort to co-examine this thesis. I am also very thankful to the BMBF (Bundesministerium für Bildung und Forschung) and the German Research Foundation (Deutsche Forschungsgesellschaft, DFG) for providing the financial support for this thesis and my research activites in the past years.

Doing research in a laboratory for several years would be an impossible journey if it was not for great colleagues and companions. I would like to express my gratitude to my colleagues and former members of the IHCT. These are (in no particular order): Martina Grabowski, Marc Hannappel, Dr. Pedro Rodriguez Vazquez, Hamadi Sadkaoui, Arjith Chandra Prabhu, Ehsan Hamzeh, Abdulraouf Kutaish, Eamal Ashna, Wolfgang Förster, Dr. Vishal Jagtap, Dr. Ritesh Jain, Utpal Kalita, Dr. Priyansha Kaurav, Dr. Laven Mavarani and Dr. Robin Zatta. While not having worked closely will all of them, they created an inspiring environment. Special thanks to Marcel Andree and Hans M. Keller for taking their time in proofreading this work. Further, I would like to thank Dr. Pedro Rodriguez Vazquez for his continuing support in understanding communication and Dr. Philipp Hillger and Dr. Stefan Malz for teaching and challenging me in the endless design processes over the years.

In addition, I also had the opportunity to supervise several students in their final thesis. Here, I would like to especially thank Kilian Hafer, Florian Heinrichsmeyer and Melissa Hadzikadunic for trusting my guidance and allowing me to grow into the role as their supervisor.
A special 'thank you' to Daniel for always disccussing the weirdest mathematical integrals with me, to Oskar for all the hours beneath the auditorium and Tae-Hun for the helpful advices along the way.

Last but not least, I would like to thank my parents and my sister for their continuous support over all these years as well as the friends and communities I have found during my time in Wuppertal, you have created a new home for me.

Publications

Journal Publications

1. L. Mavarani, P. Hilllger, **T. Bücher**, J. Grzyb, U. R. Pfeiffer, Q. Cassar, A. Al-Ibadi, T. Zimmer, J. Guillet, P. Mounaix, G. MacGrogan, "NearSense - Advances Towards a Silicon-Based Terahertz Near-Field Imaging Sensor for Ex Vivo Breast Tomour Identification", in Frequenz Band 72 Heft 3-4, March 2018, doi:10.1515/freq-2018-0016

2. U. R. Pfeiffer, P. Hillger, R. Jain, J. Grzyb, **T. Bücher**, Q. Cassar, G. MacGrogan, J. Guillet, P. Mounaix, T. Zimmer, "Ex vivo breast tumor identification: Advances toward a silicon-based terahertz near-field imaging sensor", in IEEE Microwave Magazine Volume 20, Issue 9, Pages 32-47, August 2019, doi: 10.1109/MMM.2019.2922119

3. **T. Bücher**, S. Malz, K. Aufinger, U. R. Pfeiffer, "A 210-291-GHz (8×) frequency multiplier chain with low power consumption in 0.13-µm SiGe", in IEEE Microwave and Wireless Components Letters, Volume 30, Issue 5, Pages 512-515, April 2020, doi: 10.1109/LMWC.2020.2979715

4. Q. Cassar, S. Caravera, G. MacGrogan, **T. Bücher**, P. Hillger, U. Pfeiffer, T. ZImmer, J. Guillet, P. Mounaix, "Terahertz refractive index-based morphological dilation for breast carcinoma delineation" in Scientific reports, Volume 11, Issue 1, Article number: 6547, March 2021, doi: 10.1038/s41598-021-85853-8

5. **T. Bücher**, J. Grzyb, P. Hillger, H. Rücker, B .Heinemann, U. R. Pfeiffer, "A broadband 300 GHz power amplifier in a 130 nm SiGe BiCMOS technology for communication applications", in IEEE Journal of Solid-State Circuits, Volume 57, Issue 7, Pages 2024-2034, April 2022, doi: 10.1109/JSSC.2022.3162079

Conference Publications

1. M. M. Tarar, **T. Bücher**, S. Qayyum, R. Negra, "Efficient 2-16 GHz flat-gain stacked distributed power amplifier in 0.13 µm CMOS using uniform distributed topology", 2017 IEEE MTT-S International Microwave Symposium (IMS), Pages 27-30, June 2017, doi: 10.1109/MWSYM.2017.8059102

2. P. Hillger, R. Jain, J. Grzyb, L. Mavarani, **T. Bücher**, U. R. Pfeiffer, G. Mac Grogan, P. Mounaix, J. Guillet, "A solid-state 0.56 THz near-field array for µm-scale surface imaging", 2018 43rd International Conference on Infrared, Millimeter, and Terahertz Waves (IRMMW-THz), Pages 1-2, Septembert 2018, doi: 10.1109/IRMMW-THz.2018.8509876

3. S. Malz, P. Hillger, **T. Bücher**, R. Jain, U. R. Pfeiffer, "A 108 GHz up-conversion mixer in 22 nm FDSOI", 2020 German Microwave Conference (GeMiC), Pages: 84-87, March 2020,

4. Q. Cassar, S. Caravera, G. MacGrogan,**T. Bücher** , P. Hillger, U. R. Pffeifer, T. Zimmer, J. Guillet, P. Mounaix, "Association of the terahertz refractive index and morphological dilation operations for breast carcinoma detection", 2021 46th International Conference on Infrared, Millimeter and Terahertz Waves (IRMMW-THz), August 2021, doi: 10.1109/IRMMW-THz50926.2021.9567087

5. **T. Bücher**, J. Grzyb, P. Hillger, H. Rücker, B. Heinemann, U. R. Pfeiffer, "A 239–298 GHz power amplifier in an advanced 130 nm SiGe BiCMOS technology for communications applications", ESSCIRC 2021-IEEE 47th European Solid State Circuits Conference (ESSCIRC), Pages: 369-372, September 2021,doi: 10.1109/ESSCIRC53450.2021.9567853

6. J. Grzyb, M. Andree, P. Hillger, **T. Bücher**, U. R. Pfeiffer, "A Balun-Integrated On-Chip Differential Pad for Full/Multi-Band mmWave/THz Measurements", 2023 IEEE/MTT-S International Microwave Symposium-IMS 2023, Pages: 186-189, June 2023, doi: 10.1109/IMS37964.2023.10187952

7. A. Chandra Prabhu, P. Hillger, J. Grzyb, **T. Bücher**, H. Rücker, U. R. Pfeiffer, "A 300 GHz x9 Multiplier Chain With 9.6 dBm Output Power in SiGe Technology", 2024 IEEE Radio & Wireless Week, January 2024

Contribution of others

This work was conducted at the Institute for High-Frequency and Communication Technology, (IHCT) led by Prof. Dr. rer. nat. Ullrich R. Pfeiffer at the University of Wuppertal. This work would not be possible without the contributions of other group members. Some circuit blocks, passives, and antennas in this thesis are designed by IHCT group members. These other contributions are listed below. The research not included in the following list has been conducted by myself.

Chapter 3 This chapter presents the single building blocks for broadband communication systems operating at 300 GHz. The implemented upconversion mixer was designed by Dr. Pedro Rodriguez-Vazquez, while the downconversion mixer and transimpedance amplifier were designed by Dr. Ritesh Jain. The frequency multiplication stages were implemented by Dr. Philipp Hillger, while the breakout measurements of the first tripler and the full frequency multipliers were conducted by Arjith Chandra Prabhu. The initial transformers and transistor core model for another device size as well as the antenna and the 90°Hybrids were designed by Dr. Janusz Grzyb.

Chapter 4: The improved RF connector/PCB section was designed by Dr. Janusz Grzyb. The findings regarding surface roughness and surface finish were made in close discussion with Dr. Janusz Grzyb.

Abstract

Readily available Communication has been the key ingredient for the rapid technological and societal evolution in the last century. Communication has torn down geographic and political boundaries and has given us the means to share information all over the world in a - metaphorical - blink of an eye. Communication however has not stopped the transmission of written or spoken word, but today we see a high demand for video streaming (e.g. Youtube, Netflix, Twitch) or pure data transmission for cloud computing. These increased demands have led to various communication standards i.e. for wireless communication from Global System for Mobile Communications to now fifth-generation technology standard for broadband cellular networks introduced in 2019 (5G). The exponentially growing data consumption forces research to find new ways to remove bottlenecks and increase possible data rates. One solution to increase the data rates is the use of more bandwidth or in other words occupy larger parts of the frequency spectrum.
This thirst for bandwidth has made mmWave communications attractive and it is expected that the operation frequencies and bandwidth will continue to increase for the next decades. For the next generation of wireless communication (Beyond5G or 6G), carrier frequencies up to 300 GHz have become interesting for research and development. However, research in this frequency range approaches the technological limit of existing semiconductor technologies.

This thesis focuses on the implementation of a dual-polarized transmitter and receiver operating up to 300 GHz. This allows to access an untapped frequency range which has already be envisioned as a potential solution for high-frequency communication by the IEEE. For this, the individual components were designed from scratch to achieve high bandwidth at the technological limit of Silicon germanium (SiGe) heterojunction bipolar transistor (HBT)s.

For this thesis, a dual-polarized transmitter and receiver were developed in an advanced 0.13 µm SiGe Bipolar CMOS (BiCMOS) technology. Within the scope of this thesis, the individual building blocks in the form of up- and downconversion mixers, power amplifiers, and the LO generation path are presented with their individual measurement results. These building blocks are integrated into the respective transmitter and receiver implementations. To connect the transmitter and receiver to the laboratory equipment, a broadband, high-frequency packaging is designed.

The transmitter and receiver are individually characterized for their Radio Frequency (RF) performance. In addition, back-to-back RF link performance is shown as well as actual communication over a distance of 60 cm.

The presented transmitter and receiver present the first fundamentally operated communication link in silicon at 300 GHz. With the frequency scaling and added circuit complexity of the dual-polarized communication system, limitations in both circuit design and packaging are investigated which limit the currently achievable data rate to 40 GBit/s in Quadrature Phase-Shift Keying (QPSK).

In conclusion, it is shown that silicon technologies will be able to meet the vision of both industry and standardization committees in achieving Terahertz (THz) communication. Throughout this thesis, several future improvements and concepts are introduced and discussed to show the potential of THz communication.

Zusammenfassung

Leicht zugängliche Kommunikation war der Schlüssel für die rasante technologische und gesellschaftliche Entwicklung im letzten Jahrhundert. Kommunikation hat geografische und politische Grenzen niedergerissen und uns die Möglichkeit gegeben, Informationen über die ganze Welt in einem - methaporischen - Wimpernschlag auszutauschen. Kommunikation hat jedoch nicht bei der Übermittlung des geschriebenen oder gesprochenen Wortes aufgehört, so dass wir heute eine hohe Nachfrage nach Videostreaming - in Form von Youtube, Netflix, Twitch etc. - und reiner Datenübertragung für beispielsweise Cloud Computing sehen.

Diese gestiegenen Anforderungen haben zu verschiedenen Kommunikationsstandards und ihrer Evolution geführt, z.B. für die drahtlose Kommunikation von GPRS bis zum heutigen 5G. Der exponentiell Datenverbrauch zwingt die Forschung, neue Wege zu finden, um Engpässe zu beseitigen und Datenraten zu erhöhen. Eine Lösung zur Erhöhung der Datenraten ist die Nutzung von mehr Bandbreite oder mit anderen Worten die Belegung größerer Teile des Frequenzspektrums.

Durch diesen unstillbaren Durst nach Bandbreite wird Millimeterwellen-Kommunikation zunehmend attraktiv und es wird erwartet, dass die Betriebsfrequenzen und die Bandbreite in den nächsten Jahrzehnten weiter zunehmen werden. Für die nächste Generation der drahtlosen Kommunikation (Beyond5G oder 6G) sind Trägerfrequenzen bis zu 300 GHz für Forschung und Entwicklung interessant geworden. Allerdings stößt die Forschung in diesem Frequenzbereich an die technologischen Grenzen der bestehenden Halbleitertechnologien.

Diese Dissertation befasst sich mit der Implementierung von dual-polarisierten Sendern und Empfängern bei Betriebsfrequenzen bis zu 300 GHz. Eine erfolgreiche Implementierung erlaubt die Addressierung eines bisher ungenutzen Frequenzbandes, welches durch das IEEE als potentielle Lösung für breitbandige, kabellose Kommunikation gesehen wird. Hierfür müssen zunächst die einzelnen Bestandteile des Senders und Empfängers von Grund auf neu entwickelt werden, um die entsprechende Bandbreite an der technologischen Grenze zu erreichen.

Im Rahmen dieser Dissertation wurde ein dual-polarisierter Sender und Empfänger in einer fortgeschrittenen 0,13 µm Silicon germanium (SiGe) BiCMOS Technologie verwendet. Im Verlauf der Dissertation werden zunächst die einzelnen Grundbausteine, hier im speziellen die beiden Mischer, der Leistungsverstärker und die Trägerfrequenzgenerierung beschrieben und ihre Messergebnisse präsentiert. Daraufhin werden die Grundbausteine zu vollständigen Sender und Empfängern zusammengesetzt, welche gefertigt wurden. Um die Sender und Empfänger zu charakterisieren wurden spezielle Leiterplatten entwickelt, die einen breitbandigen Zugriff auf die eigentlichen integrierten Schaltungen ermöglichen.

Sowohl Sender als auch Empfänger werden zunächst einzeln charakterisiert, um so die Leistungsmetriken wie Ausgangsleistung und Bandbreite zu extrahieren. Zusätzlich werden Sender und Empfänger in einer Distanz von 60 cm zueinander aufgebaut und die eigentliche Funkstrecke charakterisiert. Zusätzlich zur reinen, ideallen Messung werden über den aufgebauten Kanal Daten übertragen, um das Potenzial des Kommunikationssystems zu erfassen. Im Rahmen des Enticklungsprozesses und der Charakterisierung werden einzelne Problemstellungen diskutiert, welche sich aus der Frequenzskalierung und der erhöhten Systemkomplexität ergeben. Entsprechende Lösungsansätze werden hierbei auch diskutiert.

Die hier präsentierten Sender und Empfänger stellen den ersten rein auf Silizium basierten Kommunikationskanal da, welcher bei Trägerfrequenzen bis zu 300 GHz eine erfolgreiche Datenübertragung erlaubt. Die aktuell bestehenden Limitierungen durch den Aufbau und des Empfängers schränken die maximale Datenrate auf 40 GBit/s in einer QPSK-Modulation ein.

Alles in allem zeigt diese Dissertation, dass siliziumbasierte Kommunikation bei 300 GHz möglich ist und Silizium somit als potentieller Lösungsansatz für zukünftige Terahertz Kommunikation geeignet ist.

Chapter 1

Introduction

Communication systems are an integral part of our daily lives and have been a driving force behind economic and societal development in the last century. Communication has evolved from speech transmission and has become the backbone of our multimedia everyday life. Mobile communication, in particular, has grown significantly in the last 30 years, connecting people in even the most remote areas of the world with a global community. Especially, in developing countries in Africa, Asia and Southern America, the access to the internet is oftentimes only achieved through mobile communication as landline infrastructure is often not existent. The increasing connectivity has resulted in a steady rise in mobile subscriptions, which is projected to align with the global population growth (see Fig. 1.1). However, mobile data consumption is growing exponentially due to the introduction of new applications almost every day (Fig. 1.2). Here, technological trends such as artificial intelligence, autonoumos driving, remote working but also the now ever so present video streaming and cloud computing has accelerated the data consumption and with it its toll on the communications infrastructure.

To meet these demands, communication must constantly evolve. For mobile communication, this evolution has grown available data rates from 22.8 kbit/s in Global System for Mobile Communications (GSM) to currently up to 20 Gbit/s in 5G [2]. However, it is expected that this peak data rate of 20 Gbit/s will not be sufficient for the next decades. Therefore, research constantly has to find new ways to increase data rates. One popular way to increase the data rate has been the use of more bandwidth. However, for low frequencies, the absolute achievable bandwidth is limited and therefore operating frequencies have moved to the millimeter wave region with the current

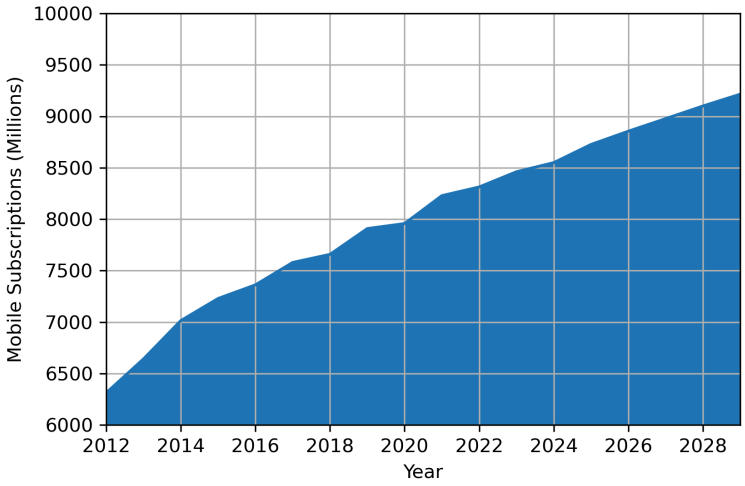

Figure 1.1: Number of mobile subscriptions up to 2029. The total number is expected to converge towards the global population [1].

5G standard which has maximum operating frequencies at 39 GHz. However, it can already be projected that this is only a temporary solution and the frequency spectrum has to be further explored.

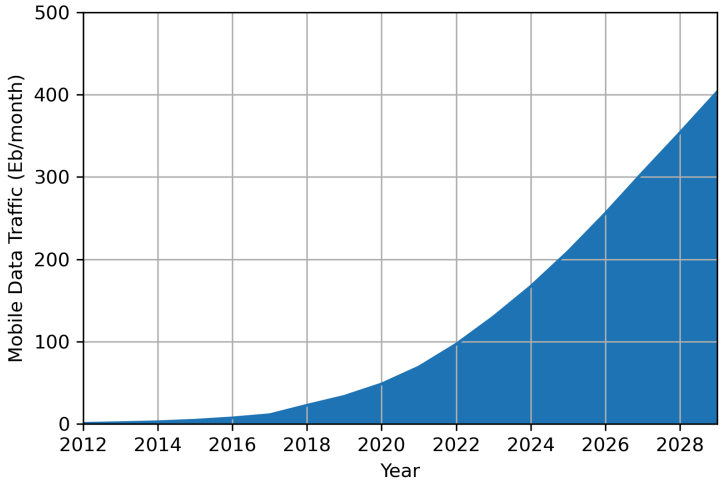

Figure 1.2: Mobile traffic data projection up to 2029 [1]. Here, an exponential growth is expected.

However, frequency bands are not readily available for communication as it is only one of many high-frequency applications and therefore has to share its spectrum with other technologies such as radar, imaging but also restricted communication. As a result, the implementation of a new communication generation is preceded by a long phase of vision and requirement definition before new frequency bands can be used. Furthermore, it is expected that the data rates in wireless communication will con-

verge with those in wired communication around 2030, as the former are increasing at a faster rate [3]. For numerous applications, wireless communication will become an appealing substitute for fixed-location communication.

One example of such an application is the backhaul, which acts as the intermediary link between the cell site and its core network. This allows the radio masts, which are commonly visible, to connect to the internet or to isolated mobile networks. The backhaul collects the cumulative data of each network subscriber and transmits it through a single broadband data link to the core network. The peak data rate of 20 Gbit/s in 5G was defined with this application in mind. However, the increasing generation of data may soon cause the peak data rate to become a bottleneck for 5G connectivity. The constant evolution towards the next generation of wireless mobile communication is already underway.

1.1 Towards a New Generation

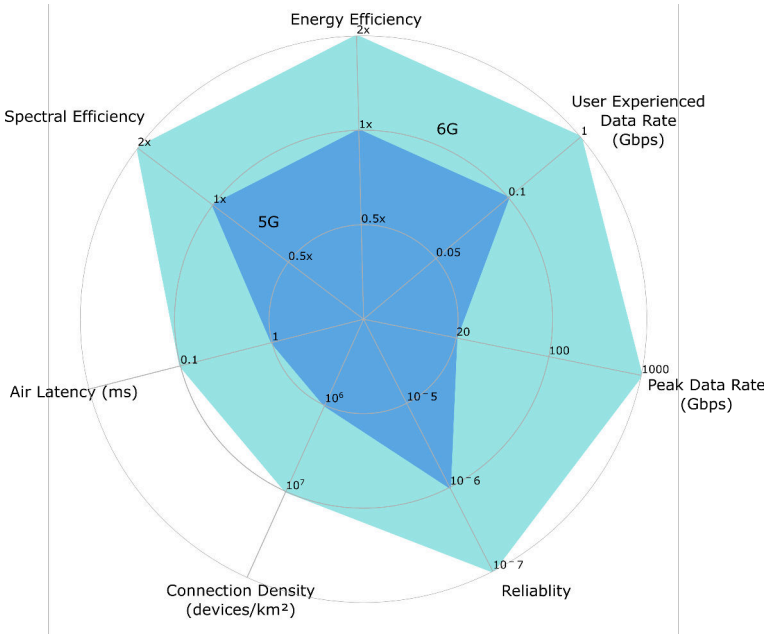

Figure 1.3: Requirements for 6G [2]. It is expected that the peak data rate will increase by a factor of 50.

Several companies and standardization councils have identified the major requirements and challenges for the next wireless communication generation as shown in Fig. 1.3. According to consumer electronics manufacturers such as Samsung, the next generation of wireless communication should aim for a peak data rate of 1000 GB/s and a user-experienced data rate of 1 GB/s [2] to meet the demands of the coming years.

Similarly, it is desired that the air latency reduces by a factor of 10, which is of high importance for Autonoumos Driving, as it ensures that cars can react to an ever-changing environment in traffic.

This latency is also of interest for applications such as augmented and virtual reality as it allows for a smooth operation experience for the customers.

In multiple white papers by several companies [1], [2], but also in the 6G flagship project in Finland or the multiple 6G research hubs in germany (6GEM, 6G-RIC, 6G-life, Open6GHub), the adoption of Terahertz frequencies is discussed as a potential option to further increase the data rates.

At the same time, it should be noted that communication systems operating above 200 GHz will very likely not be available in smartphones or for regular users, as they are faced by several physical limitations which limit their operation to short range line-of-sight communication.

One of these limitations is the atmospheric attenuation which describes the frequency dependence of the attenuation of electrical waves in a media, in our case air. This frequency dependence is shown for radio frequencies up to 1 THz in Figure 1.4. Here, several resonances in the spectrum can be seen which are related to water vaper absorption caused by different resonant effects in water molecules. However, with increasing frequency, a window can be identified between 200 and 300 GHz where no resonance is present and the attenuation increases slowly over frequency.

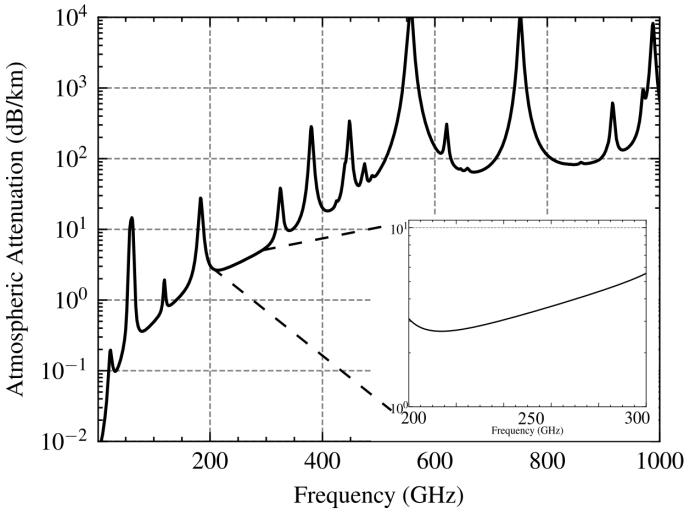

Figure 1.4: Atmospheric attenuation over frequency. Different resonance effects in the atmosphere cause local maxima.

Due to this atmospheric window, communication above 200 GHz becomes attractive as it presents a broadband frequency range where communication can be established.

At the same time, this frequency range presents a challenge for electrical circuits as the transistor performance decreases with frequency, resulting in a further decreasing output power at high frequencies. Here, the technological development of transistor technology might set the ultimative limit to high-frequency communication.

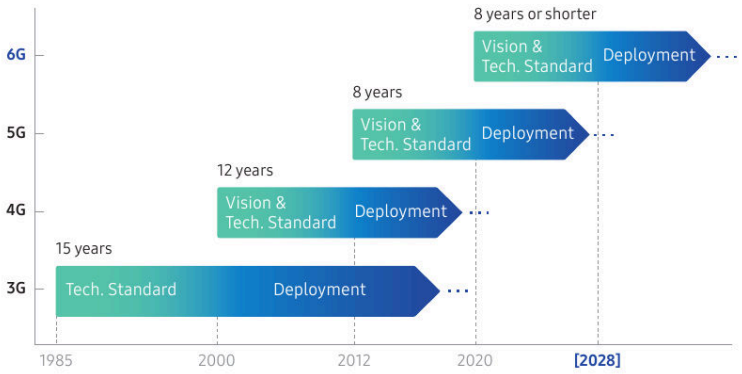

Figure 1.5: Timeline for 6G [2]. The time to deployment has become shorter with each generation.

As shown in the timeline for the expected 6G development (Fig. 1.5), 6G right now is in its definition phase. Thereby, it is up to research to show where the physical limitations are and provide hope to the vision for 6G.

In 2017, an initial standard for Terahertz Communication was released [4] which defined potential carrier frequencies and bandwidths in a frequency range between 250 and 325 GHz. Here, the envisioned carrier frequencies start at 255 GHz and move up to 320 GHz, while channel bandwidths ranging from 2.16 GHz to 69 GHz.

In addition, it was already expected that THz communication at this frequency will be restricted to point-to-point communication which is seen as a reaction to the increased attenuation but also to the decreased output power of electronic devices.

In the following, the state-of-the-art will be reviewed to define the challenges for communication according to the IEEE Std. 802.15.3d-2017 or more general for communication with carrier frequencies up to 300 GHz.

1.2 State-of-the-Art

The State-of-the-Art in this dissertation can be divided into two fields. One is the generation of high-frequency signals with high output power and the other field is the implementation of such generation in complete communication links.

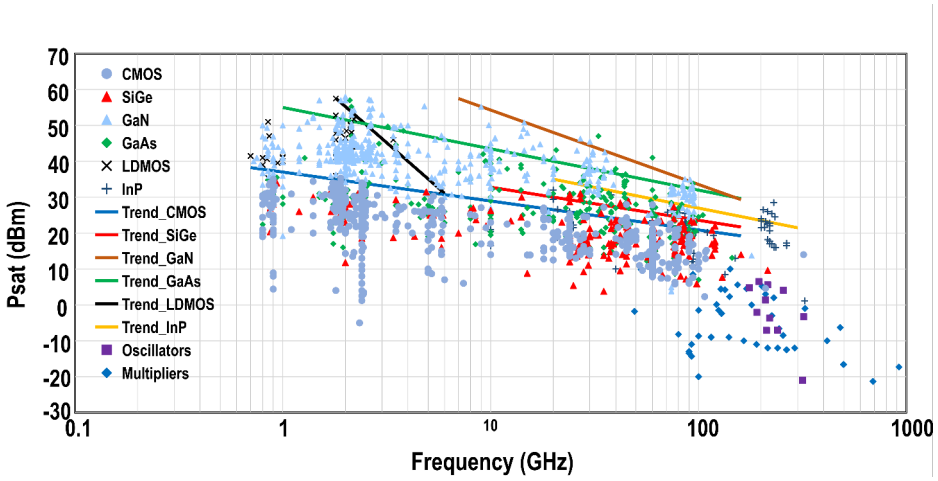

Figure 1.6: State of the art of Power amplifiers until 2017 for different semiconductor technologies [5].

For the output power, the PA survey can be taken into consideration, as shown in Fig. 1.6 [5], which shows the maximum output power in combination with center operating frequencies of power amplifiers. In the presented overview, the data points of power amplifiers published after 2017 were removed to show the lack of data points above 100 GHz at the start of the research activity for this dissertation.

In this overview, research's focus on frequencies below 100 GHz becomes clear as the available transistor technologies set an upper limit for output power which is marked by the lines in the Figure 1.6. A further advancement in operating and design frequencies therefore must always be accompanied by a development of faster transistors, as it has been visible in the past for D-Band communication and communication around 240 GHz. These were the results of the EU projects dotfive and Dot7, which resulted in an increased f_{max} for SiGe transistors and enabled further research at higher frequencies.

After 2017, further amplifiers operating above 200 GHz were developed as shown in Table 1.1. Only [10], [12]–[14] address larger parts of the envisioned frequency band above 250 GHz. However, the high output power [12], [13] is achieved through power combining leading to an undesired large circuit size which is disadvantageous for integration in complete communication systems.

Table 1.1: Silicon based power amplifiers above 200 GHz in silicon technology

Ref	Technology	Frequency (GHz)	Small Signal BW (GHz)	S21 (dB)	P_{sat} (dBm)	P_{dc} (mW)
[6]	130nm SiGe	228 - 256	28	10	5.5	400
[7]	130nm SiGe	200 - 255	55	12.5	13.5	740
[8]	130nm SiGe	247 - 314	67	15	5	268
[9]	130nm SiGe	209 - 244	35	21.8	3	66
[10]	130nm SiGe	260	16.5	15	-	112
[11]	65nm CMOS	195 - 209	14	19.5	9.4	732
[12]	130nm SiGe	305	15	14.5	7.5	1008
[13]	130nm SiGe	242-275	33	21.4	12.5	-

Therefore, an ideally compact power amplifier should be designed to cover the unexplored frequency range for silicon-based communication systems.

For communication systems, the state-of-the-art for link operation can be seen in Table 1.2. The decreased output power of CMOS-based communication systems can be seen by the reduced link distance of a few centimetres. Nonetheless, only CMOS-based communication systems [3], [15], [16] have been able to address frequency bands as definied in the IEEE standard [4]. SiGe-based solutions so far have not surpassed 260 GHz as their carrier frequency.

While more receivers operating up to 290 GHz have been reported [22], [23], only their individual performance without a communication link have been shown and therefore will not be discussed in this state-of-the-art. The receiver and transmitter state-of-the-art will be discussed in the conclusion of Chapter 5 where they are compared to the measured RX and TX.

Table 1.2: Wireless links above 200 GHz in silicon technology.

Ref	Technology	Frequency (GHz)	Modulation	Data-rate (Gbps)	P_{DC} (W)	Distance (cm)
[17]	130nm SiGe	190	BPSK	50	0.154	0.6
[18]	40nm CMOS	290	16-QAM	32	2.05	1
[19]	130nm SiGe	220-260	32-QAM	90	1.96/0.98	100
[20]	130nm SiGe	240	BPSK	25	0.95	15
[6]	130nm SiGe	220-255	16-QAM	100	1.41/0.55	100
[15]	40nm CMOS	290	16-QAM	32	0.65	1
[16]	40nm CMOS	265.58	16-QAM	80	0.89/0.88	3
[21]	130nm SiGe	235	QPSK	65	1.41/0.98	100

1.3 This dissertation

In the preceding introduction, preliminary insight into broadband communication based on the technological development in the last decade was built up. By reviewing the state-of-the-art in THz communication, it is pointed out that the initial standardization of a possible THz communication band is more optimistic for high-frequency operation than the existing implementations of silicon-based communication systems. Due to this, the dissertation will focus on answering the following research questions.

1.3.1 Central Research Questions

The research questions that are sought to be answered are listed below. The related original contributions of this work are given.

Central Research Question

Can silicon-based communication systems achieve broadband communication at 300 GHz?

Previous research on RF front-ends has shown that communication around 240 GHz is feasible. However, the standardization has introduced carrier frequencies beyond this, which had not been reached using silicon technology. This work aims to push the circuit design to the current physical limit while also highlighting the advantages of high-frequency communication. For this, the bandwidth generation in several building block is to be maximized.

Following additional research questions arise in the progression of the dissertation:

- Is Broadband Communication solely a challenge for the RF domain or does baseband design and packaging create additional challenges?
- Can existing transistor technologies be used for future communication applications at carrier frequencies around 300 GHz?
- Can the bandwidth requirements be fulfilled for RF power amplifiers?
- Will mixer-first receivers improve a 300 GHz communication link?

For this, the performance of single circuit blocks such as the broadband power amplifier and frequency multipliers is evaluated at on-wafer level. The building blocks are then integrated into a full system which is characterized on both RF level and through communication demonstrations.

1.3.2 Original Contributions

This dissertation focuses on the design and measurement of a broadband communication system with carrier frequencies up to 300 GHz. For this, this thesis introduces the individual building blocks for both transmitter and receiver. As the operating frequencies of the communication system are increased, the LO frequency generation and power amplifiers were designed with this application in mind. Furthermore, power amplifiers are benchmark circuits for technological capabilities, highlighting the potential for various applications such as imaging and ranging. Here, novel matching structures in the form of asymmetric coupled-line transformers are introduced to provide broadband matching and power generation in combination with a new generation of SiGe BiCMOS transistors. Through this, a power amplifier with a 3-dB bandwidth ranging from 239 to 302 GHz was designed with a peak P_{sat} of 9.7 dBm.

Furthermore, this dissertation presents the first silicon-based wireless communication link using carrier frequencies up to 300 GHz with fundamentally driven mixers. Based on broadband amplifier and LO generation, the communication system allows for a wide range in LO frequency allocation due to the high RF/LO bandwidth of 62 GHz (243-305 GHz) for the receiver and 53 GHz (243-296 GHz) for the transmitter. Both transmitter and receiver have an individual baseband bandwidth of 8 GHz, which is limited by the Printed Circuit Board (PCB) packaging, while the total link bandwidth is extended up to 13 GHz.

Through this, maximum data rates of 30 Gbit/s for BPSK and 40 Gbit/s for QPSK were measured. For a carrier frequency of 300 GHz, the measured data rate is limited to 20 Gbit/s in BPSK due to the limited SNR and bandwidth at this frequency.

1.3.3 Thesis Structure

This thesis is divided into multiple chapters, following the journey to ultra-wideband RF frontends. The thesis is organized as follows:

Chapter 1: Provides an introduction into the presented disseration giving its motivation and an initial state-of-the-art. The research question and the structure of the dissertation is presented as well.

Chapter 2: Describes the theoretical background needed for Top Level System analysis and implementation and states the advantages and disadvantages of different communication system topologies. For circuit implementation, the different signaling principles are introduced.

Chapter 3: Discusses the circuit level design of both transmitter and receiver. Following the block diagram of TX and RX, the different building blocks are introduced with their simulated performance and the measured results of the power amplifier and frequency multiplication stages.

Chapter 4: Discusses the packaging, with its challenges and solutions needed for ultra-wideband communiation.

Chapter 5: Describes the RF characterization of fully integrated and packaged transmitter and receiver.

Chapter 6: Discusses the back-to-back characterization of the transmitter and receiver in both RF characterization and data transmission in a link over a distance of 60 cm.

Chapter 7: Concludes the dissertation by summarizing the previous chapters and giving an outlook for future improvements and directions for broadband THz communication.

Chapter 2

Theoretical Background

This chapter introduces digital communication and its performance metrics as the final application of the circuits and systems discussed in this dissertation. Basic concepts of communication systems are also introduced to explain the design choices made in the later presented communication system (Chapter 3). Furthermore, this chapter discusses signal propagation in guided and unguided media, as communication involves at least one information source and one recipient. The chapter concludes with a discussion on semiconductor technologies that enable communication at 300 GHz.

2.1 Communication

Communication is a key application of electrical circuits and has been a driving force behind globalization and the third and fourth industrial revolutions. It constantly evolves to meet the needs of a continuously growing consumer market. This section will discuss bandwidth, which is directly linked to the amount of data transmitted simultaneously. Furthermore, this text will cover the topics of analogue and digital modulation, as well as introduce common performance metrics for communication.

2.1.1 Bandwidth

In communication, a link is ultimately defined by the channel capacity. The channel capacity **C** is the upper limit for the transmitted data rate. The definition of this channel capacity was developed in the 1940s by Claude Shannon and Ralph Hartley and is still valid to this day[24]. The equation shown below defines the relation between the channel capacity **C** and bandwidth **B** in Hertz and the Signal-to-Noise-Ratio **SNR** of the channel.

$$C = B \log_2 \left(1 + \frac{S}{N}\right) \tag{2.1}$$

With a theoretically constant SNR, the maximum achievable data rate is directly proportional to the used channel bandwidth. The equation also shows that bandwidth alone has a higher impact on data rate than increased signal power or reduced noise levels. For a sufficiently large SNR ($\gg 1$), $\log_2 \left(1 + \frac{S}{N}\right)$ can be approximated by $log_2 \left(\frac{S}{N}\right) \approx 3.32 \cdot \log_{10} \left(\frac{S}{N}\right)$. This is called the bandwidth-limited regime with

$$C \approx 0.332 \cdot B \cdot SNR. \tag{2.2}$$

Bandwidth is an analog concept that describes the frequency range used for communication. It is important for both analog and digital communication as signals must be transmitted through purely analog channels such as air or transmission lines. The bandwidth in the spectrum is not an occupied rectangle and is highly independent of the modulation schemes and pulse shaping used.

2.1.2 Analog Modulation

Analog modulation is the process of encoding information into a signal for transmission through a desired channel. As digital signals, i.e. ones and zeroes, cannot be wirelessly transmitted, data must be transformed into an analog representation and modulated into a carrier signal. There are different types of analog modulation, including amplitude, phase, and frequency modulation. In phase and frequency modulation, the information causes a change in the phase or frequency of the modulated sinusoidal wave. In amplitude modulation, the amplitude of the sinusoidal wave is directly proportional to the transmitted information.

Amplitude and phase modulation, as well as their combination, quadrature amplitude modulation, are the most common forms of modulation used in modern communication. Quadrature amplitude modulation allows for high spectral densities but is sensitive to signal-to-noise ratio and the linearity of transmitters and receivers. In contrast, phase shift keying is independent of amplitude and thus more robust at low signal power levels.

However, it is important to note that data is mostly digital these days. Therefore, it is necessary to discuss digital modulation as the ability of the presented communication links to discriminate between ones and zeroes will ultimately be evaluated.

2.1.3 Digital Modulation

In contrast to analog modulation, digital modulation is based on discrete events and thus can be described as a sequence of discrete pulses in time

$$u(t) = \sum_{n=1}^{\infty} b[n] * p(t - nT).$$

Here, $b[n]$ is a discrete sequence of bits while p(t) is a pulse with a defined length. Digital modulation provides several advantages over analog modulation, including better noise immunity, higher spectral efficiency, and the ability to incorporate error correction techniques. As a result, digital modulation is widely used in modern communication systems, including digital radio, television, satellite communication, and various wireless technologies.

2.1.4 Pulse Shaping

Pulse shaping is used in digital modulation to control the shape and duration of the transmitted pulses. The primary reasons for using pulse shaping in digital modulation include:

- **Increasing Bandwidth Efficiency:** Pulse shaping reduces the occupied bandwidth of the transmitted signal by appropriately shaping the pulses. This minimizes the spectral width of the signal, which is crucial in bandwidth-efficient systems as it allows for more efficient use of the available frequency spectrum.
- **Improving Signal-to-Noise Ratio (SNR):** Pulse shaping can optimize the trade-off between bandwidth and power, enhancing the robustness of the signal in the presence of noise and improving the signal-to-noise ratio (SNR) of the transmitted signal.

- **Reducing Intersymbol Interference (ISI):** In digital communication systems, information is transmitted as a sequence of symbols. Improperly shaped pulses can cause intersymbol interference (ISI) by spreading into adjacent symbol intervals. Pulse shaping minimizes ISI by controlling pulse duration and preventing pulse overlap.

2.1.5 Eye Diagram

The eye diagram is a graphical representation of a digital signal's behavior over multiple sampling periods. It is created by overlaying a series of consecutive signal traces, sampled at regular intervals, and aligned to a common time axis. The resulting plot resembles an "eye" shape, hence its name. The eye diagram visualizes the signal's amplitude, timing, and noise characteristics, allowing for the evaluation of its quality and performance.

The eye-opening represents the dynamic range of the signal, indicating the margin for successful detection by the receiver. The vertical and horizontal cursors enable measurements of various parameters, including voltage levels, rise and fall times, jitter, and eye height and width. These measurements help quantify the signal's quality and identify potential impairments or distortions.

Eye diagrams are a valuable tool in characterizing the response of a channel in high-speed digital communication systems. They aid in identifying sources of signal degradation, such as intersymbol interference, noise, and timing errors. Additionally, they are useful in evaluating the performance of clock recovery circuits, data transmission links, and serial interfaces. The clock recovery circuit is not part of the implemented receiver, however the internal clock recovery in the used oscilloscopes can directly point to potential noise and timing errors in the transmission.

The eye diagram is a useful tool for analyzing the quality and characteristics of a digital signal. It provides valuable insights into the signal's behavior, including its amplitude, timing, and noise characteristics.

- Signal Amplitude: The eye diagram enables the observation of the signal's amplitude levels, which are represented by the size of the eye opening. A larger eye opening indicates a higher signal quality and better noise immunity, providing a larger margin for successful signal detection by the receiver.

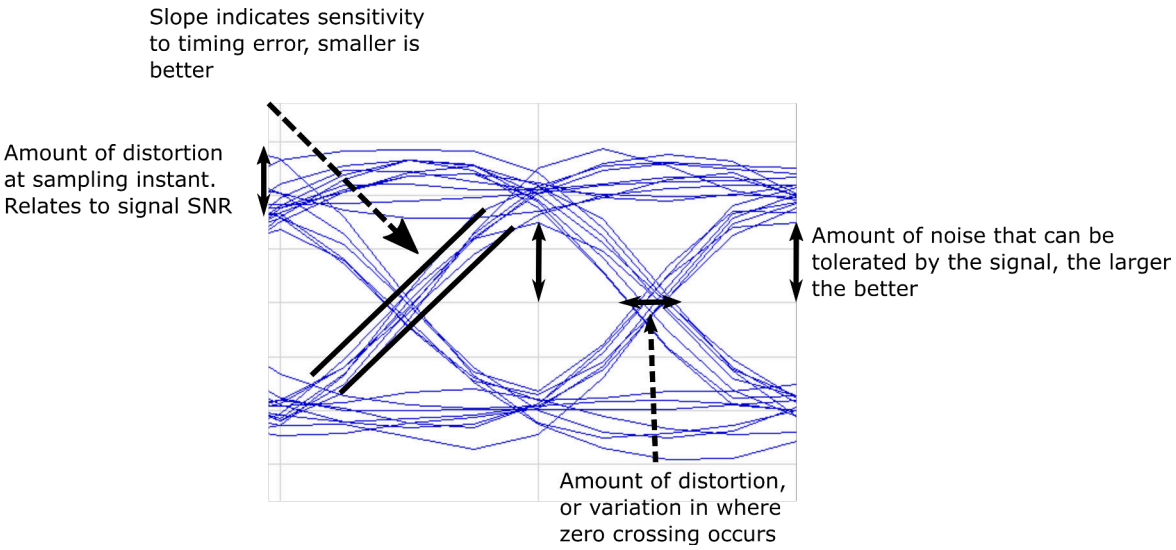

Figure 2.1: Exemplary eye diagram. The different effects on the eye diagram are indicated.

- Timing and Jitter: The eye diagram analysis allows for the assessment of the timing accuracy and jitter characteristics of the signal. Timing parameters, such as rise and fall times, can be measured using the horizontal cursors on the eye diagram. Jitter, which represents timing variations, can be evaluated by examining the spread of the eye diagram's traces.

- Noise and Distortion: The eye diagram shows the presence of noise and distortion in the signal. By analyzing the noise patterns or blurring of the eye opening, various types of noise, such as random noise, crosstalk, and inter-symbol interference (ISI), can be identified. Irregularities within the eye diagram also reveal distortions, such as reflections or amplitude fluctuations.

- Channel and System Impairments: The eye diagram is a useful tool for identifying and diagnosing impairments in communication channels or systems. It can visualize reflections or distortions caused by impedance mismatches or transmission line effects. Furthermore, anomalies in the eye opening can reveal non-idealities in transmitters, receivers, equalizers, or clock recovery circuits.

2.1.6 Error Vector Magnitude

The Error Vector Magnitude (EVM) is a key performance metric for communication links as it describes the derivation of an actual communication link from the ideal. The EVM is derived from the description of modulation schemes in their constellation diagrams as seen for a QPSK modulation with 4 symbols as shown in Fig. 3.37.

For a perfect ideal transmission, the constellation diagram has clearly defined states that the combinations of the two I/Q streams and their respective amplitudes describe.

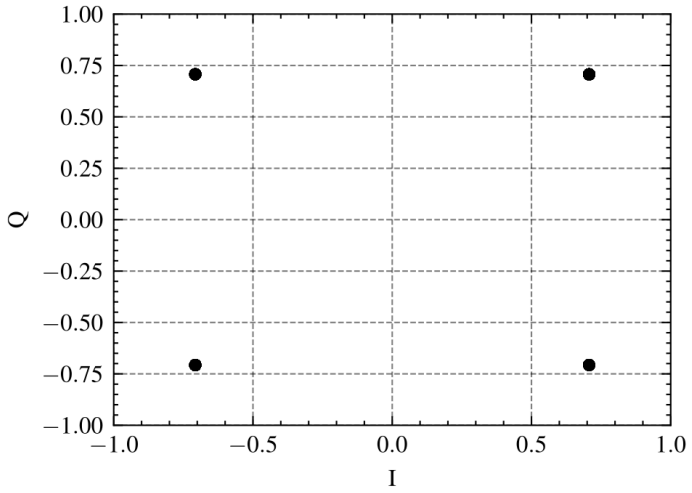

Figure 2.2: Ideal constellation diagram of a QPSK modulation.

The EVM here describes the percentual derivation of a real combination to its ideal value. Each point on the ideal constellation diagram can be described by the ideal transmitted vector E_t, whereas the real received symbol is described by the vector E_r. The resulting error vector E_{err} including the linear, non-linear distortion and added noise is described as

$$E_{err} = E_r - E_t \tag{2.4}$$

This vector allows the calculation of the variance σ_{Err} as:

$$\sigma_{Err} = \frac{1}{I}\sum_{i=1}^{I}|E_{err,i}^2| \tag{2.5}$$

with I being the total number of received signal vectors and i being the individual received signal vector.

The actual EVM calculation can be made based on two differing definitions [25]. For one definition, the power of the longest ideal constellation vector $|E_{t,m}|^2$ is used for normalization.

$$EVM_m = \frac{\sigma_{Err}}{|E_{t,m}|} \tag{2.6}$$

In contrast to this, EVM_a is normalized to the average power $|E_{t,a}^2|$ of all symbol vectors within a given constellation.

$$EVM_a = \frac{\sigma_{Err}}{|E_{t,a}|}\, with |E_{t,a}| = \frac{1}{M}\sum_{i=1}^{M}E_t^2. \tag{2.7}$$

Both definitions' relationship can be described by a factor k, depending on the modulation scheme. Resulting in

$$EVM_a = k \cdot EVM_m \tag{2.8}$$

with

$$k^2 = \frac{|E_{t,m}|^2}{|E_{t,a}|^2} \tag{2.9}$$

In ideal Binary Phase-Shift Keying (BPSK)/QPSK modulation, the two EVM definitions should be identical as the average power ideally is equal to the maximum power. For amplitude modulated signals however, these terms will differ.

In the absence of modulator and demodulator imperfections, the EVM is solely dependent on the signal-to-noise ratio:

$$EVM = \sqrt{\frac{1}{SNR}} \tag{2.10}$$

This simplification, however, is only valid for RMS EVM calculation [26]. For a SNR of 8.4 dB, the corresponding EVM in this case is 38% and therefore would be sufficient for a practically error-free transmission with QPSK modulation. To reach the same conditions with 16-QAM, a SNR of 15 dB would be necessary.

The EVM definition can be extended when taking the quadrature gain imbalance g_{imb} and phase imbalance ϕ_{imb} of the transmitter into consideration under the assumption of an infinite SNR. A 1 dB amplitude imbalance or a 5° phase imbalance causes an EVM_a of 5.74% or 4.36% respectively. With both effects occurring at the same time, the resulting EVM_a is 7.21%. With a typical SNR of 25 dB, the resulting EVM_a would be 9.14%.

$$EVM = \sqrt{\frac{1}{SNR} + 2 - \sqrt{1 + \frac{2g_{imb}}{1+g_{imb}^2} + \cos(\phi_{imb}) + \frac{2g_{imb}}{1+g_{imb}^2} \cdot \cos(\phi_{imb})}} \tag{2.11}$$

Another cause for EVM degradation is the existing zero-mean Gaussian phase noise with its variance σ_{LO}, creating an additional error term resulting in a phase misalignment between transmitter and receiver[25]. With a typical SNR of 25 dB, an LO rms phase error of 1°increases the baseline EVM_a of 5.62% by 0.16%, whereas a phase error of 5°causes an increase of 4.75% of the original EVM_a [25].

$$EVM = \sqrt{\frac{1}{SNR} + 2 - 2 \cdot e^{-\frac{\sigma_{LO}}{2}}} \tag{2.12}$$

This origin of EVM degradation is important in the design of LO frequency generation in this dissertation.

2.1.7 Architectures

Communication receivers can generally be divided into two architectures: direct-conversion and super-heterodyne. Each architecture creates unique requirements for circuit blocks.

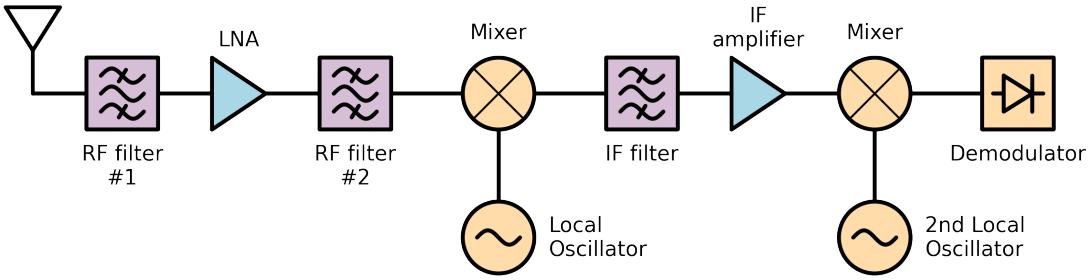

Figure 2.3: Super heterodyne receiver block diagram. This architecture requires two mixers as well as IF signal conditioning.

In a superheterodyne architecture (Fig. 2.3), the local oscillator frequency differs from the carrier frequency. Therefore, in the down-conversion process, the passband shifts by the difference between the carrier frequency and local oscillator frequency to an intermediate frequency. Therefore, the generated IF bandwidth must match the RF bandwidth, which requires broadband IF amplifiers. For communication systems with bandwidths greater than 50 GHz, the center intermediate frequency (IF) must be at least 25 GHz to accommodate the downconverted double sideband spectrum. This creates challenges for the IF amplifier and leaves the IF frequency range at high frequencies that are difficult to convert using digital signal processors. The frequency range of digital signal processors is limited by their sampling rate, which is constrained by the Nyquist-Rate.

Direct-conversion receivers (Fig. (2.4)) require only one mixing stage, reducing circuit complexity compared to superheterodyne receivers. This reduction in components not only reduces the receiver's overall size but also further reduces power consumption. Additionally, the processed bandwidth is only half of the RF bandwidth, making filter design and processing easier. However, the baseband also includes the downconverted LO leakage, making it sensitive to the LO phase noise of both the transmitter and receiver, as well as the $1/f$ noise of the transistors. Therefore, the direct-conversion receiver is typically noisier and less sensitive than a superheterodyne receiver. Additionally, the direct-conversion receiver can suffer from DC offset, I/Q mismatch, LO leakage, and other issues that must be considered during the design process [27].

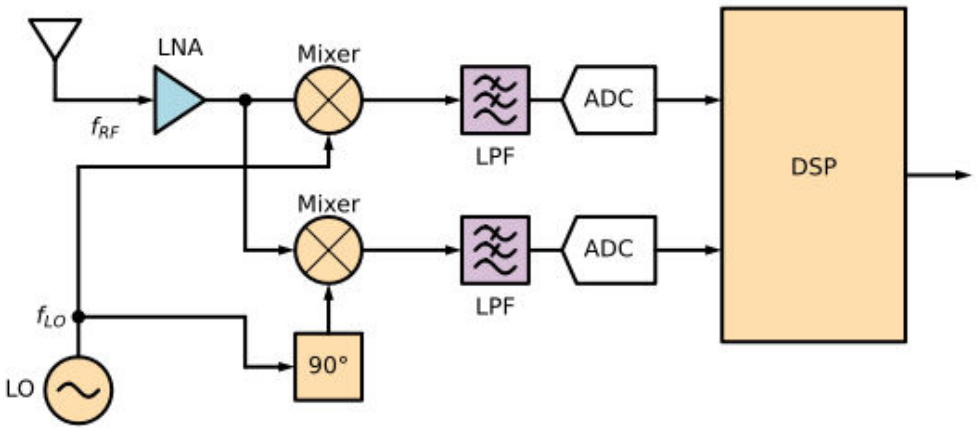

Figure 2.4: Direct conversion receiver block diagram. This architecture only requires one mixer which directly converts the RF signal to the baseband.

In general, transmitters provide identical architectures as receivers. Similar to receivers, direct conversion transmitters share the same advantages of a simplified circuitry due to the lack of the second mixer and additional IF signal conditioning. Given the similarity of these architectures for both receiver and transmitter, only the block diagrams of the receiver architectures are shown.

2.1.8 Amplifier-First vs. Mixer-First Receiver

Independent of the receiver architecture of choice, receivers can further be separated into mixer-first and amplifier-first receivers. While it seems logical to incorporate a LNA as the first block after the antenna based on the Friis-Noise-Formula[28], this approach does not always yield the best results in communication systems. At frequencies around 300 GHz, LNA implementations are rare due to the low available gain and increased noise figure of the existing transistor technologies at this frequencies [29]–[32]. To mitigate the influence of the introduced noise, a broadband high-gain amplifier is needed with a flat gain response. If the gain of the amplifier is not flat, this leads to sideband asymmetry which creates another source for bandwidth reduction in broadband communication systems [33]. In contrast to this, mixer-first receivers can exhibit a broadband response when the antenna is matched to the emitters of a switching quad. Thereby, the sideband asymmetry is reduced leading to an improved performance despite the reduced signal power.

In the presented dissertation, the implemented receivers are mixer-first as no respective LNA operating up to 300 GHz with sufficient bandwidth has been implemented so far. Based on the receiver characterization in Chapter 5, a prediction can be made whether LNAs can further improve the performance of communication systems at

300 GHz except for the possible range extension. For amplifier-first receivers, the LNA's bandwidth should at least match the mixer's bandwidth without introducing additional sideband asymmetry. At the same time, the LNA's noise figure should be lower than the noise figure of the downconversion mixer while having high gain. A high gain does not necessarily improve the performance as communication systems are often not SNR limited, but include many other impairements limiting the maximum data rate [34].

The designed power amplifier shown in Chapter 3 was not used as an amplifier in the RF path of the receiver as the design specifications were focussed on high output power which also lead to a high power consumption while the noise performance was ignored.

2.2 Propagation in Guided Media

To understand several of the design concepts and decisions presented in the following chapters of this dissertation, it is necessary to introduce signaling and explain how signals propagate in guided media, such as those found in integrated circuits and on PCB. The following discussion will focus on single-ended and differential signaling, as these are the two most common types.

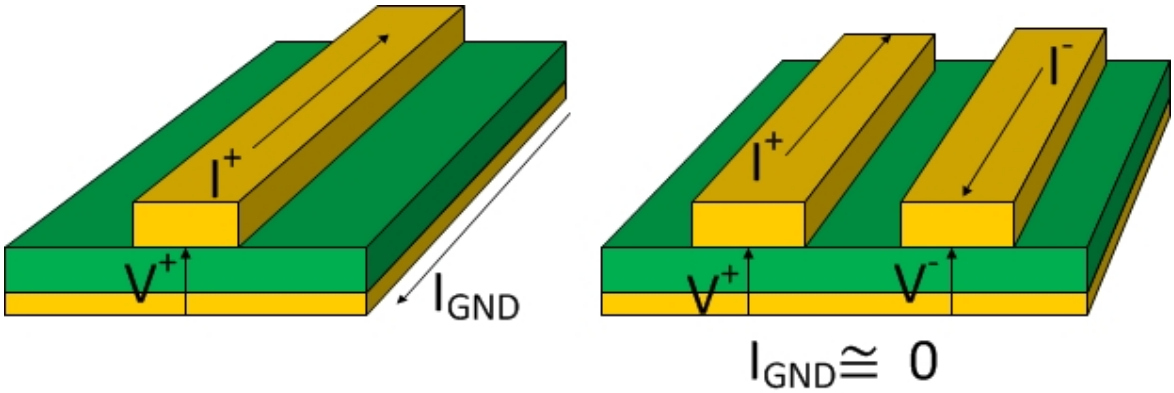

Figure 2.5: Depiction of single-ended (left) and differential signaling (right) on PCB[35]. In single-ended signaling, the current return path is in the ground plane. In differential signaling, the current return path is in the second conducting line.

2.2.1 Single-ended Signaling

Single-ended signaling (see Fig. 2.5) is the most common type of signaling in wired media because it relies on a two-conductor configuration, where one conductor contains the signal - typically time-varying - while the other conductor has a constant voltage level, typically referred to as reference ground. Most instrumentation relies on single-ended signaling, so shielded cables typically have an inner conductor that contains the signal and an outer conductor that is ground. The main advantage of single-ended signaling is its simplicity, especially on PCBs where it is typically found in the form of microstrip transmission lines. However, especially in communications, its susceptibility to noise becomes a problem, making differential signaling more popular, especially for wideband circuits. Another limitation is the geometric feature size, which will be discussed in Chapter 4.

2.2.2 Differential Signaling

Ideal differential signaling is also achieved in a two-wire configuration. Here, both conductors contain the propagating signal, which is described by the difference - hence the name - of the two individual signals. Since the two propagating signals are balanced, with identical amplitude and inverse polarity (see Fig. 2.5), the return currents are also balanced and will combine destructively. For ideal differential signaling, the current flowing in the ground plane is zero. However, the concept of purely differential signaling does not exist in physical systems. It is practically impossible to create and maintain purely differential signals, because it requires a perfectly symmetrical environment. However, especially in active circuits, the presence of transistors, which are never 100% identical, creates impurities and leads to the excitation of the common mode.

For active circuits, the existence of the common mode is often needed, as it allows biasing of differential circuits without changing the differential behavior. Therefore, the more common form of differential signaling is pseudo-differential signaling with the presence of a ground plane to guide the common mode return currents. Differential signaling using coupled lines is discussed below. While differential signaling using coplanar waveguide transmission lines or shielded transmission lines is possible, and even simple microstrips with sufficient spacing can be used as individual single-ended transmission lines with differential propagating signals, the following applies to differential signaling using coupled lines (compare Fig. 2.6), coupled lines allow for differential signal propagation in a highly confined physical space.

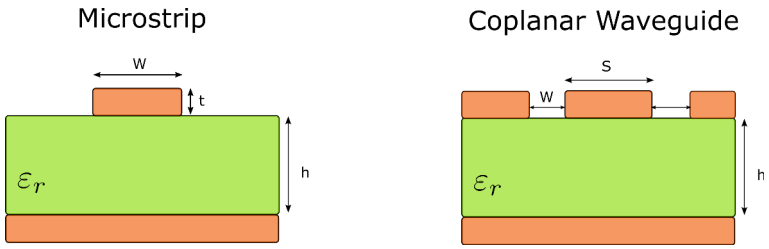

Figure 2.6: Microstrip and coplanar waveguide transmission line. In microstrip transmission lines, the electric field is mostly confined between the conductor and the ground plane. In the coplanar waveguide, the fields are ideally confined between the planar ground and the line when the distance is kept small.

The ground plane here allows for describing and analyzing circuits through the even/odd mode analysis [36]. The even/odd mode analysis is valid for coupled TEM lines in a homogenous medium or for transmission lines with identical dimensions, which is the typical case for single layer PCB [37] as shown in Chapter 4. For asymmetrically coupled lines, the even/odd mode analysis validity is limited to specific cases [38]–[40].

2.2.2.1 Even and Odd Mode

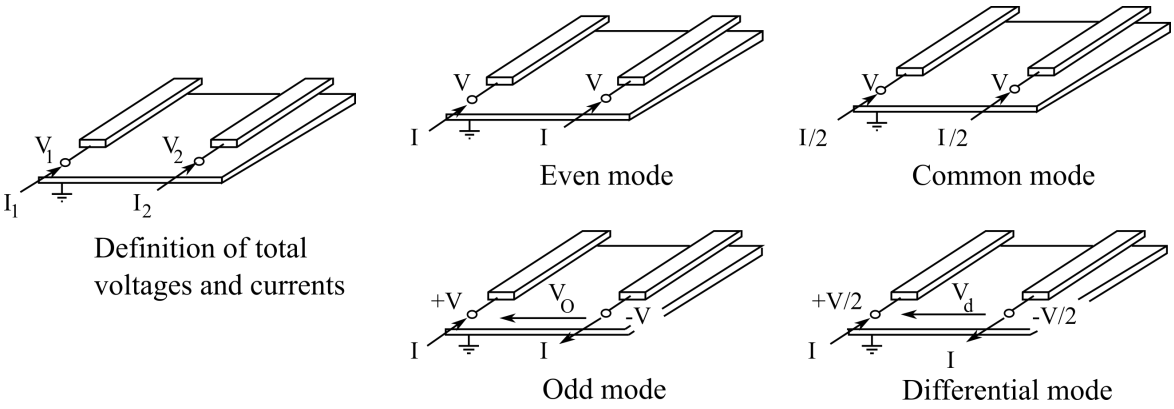

Figure 2.7: Depiction of Even and Odd Mode Excitation [41]. The different conditions for current and voltage are shown.

The even mode as shown in Fig. 2.7 is described by identical current and voltage amplitudes and polarities. In contrast to this, the odd mode is based on inverted voltages and currents. Here, the H-Fields cancel out in the symmetry plane and create a virtual ground.

The Even and Odd mode analysis of coupled lines allows us to derive the differential- and common-mode characteristic impedances directly from the simplified view given by even and odd modes. The even mode voltages and currents are defined as $V_1 = V_2 = V_{even}$ and $I_1 = I_2 = I_{even}$, whereas the common voltage and currents are $V_1 = V_2 =$

V_{common} and $I_1 + I_2 = I_{common}$ Thus, the relationship between even-mode characteristic impedance $Z_{0,even}$ and common-mode characteristic impedance $Z_{0,common}$ is given as:

$$Z_{0,common} = \frac{1}{2} Z_{0,even} \tag{2.13}$$

Similarly, the odd mode voltage and currents are: $V_1 = -V_2 = V_{odd}$ and $I_1 = -I_2 = I_{odd}$, and the differential mode voltages and currents: $V_1 - V_2 = V_{diff}$ & $I_1 = -I_2 = I_{diff}$. Thereby, the relationship between the odd-mode characteristic impedance $Z_{0,odd}$ and the differential characteristic impedance $Z_{0,diff}$ is:

$$Z_{0,diff} = 2Z_{0,odd} \tag{2.14}$$

A major drawback of differential signaling on normal transmission lines is the inaccessibility of the common mode. Typically, transmission lines are used to match the differential circuit while ignoring the common mode. However, especially on transmission lines, the common mode propagates just as well as the differential mode, and thus can create common mode gain and, more critically, common mode instability. One way to handle the common mode in a matching circuit is to use transformers, which typically have symmetry planes and allow common mode termination optimization without degrading the differential matching. These properties are discussed for various examples in Chapter 3, as such transformer-based matching is used in several building blocks of the communication system in this dissertation.

2.3 Propagation in Unguided Media

For wireless communication, the guided signals inside the integrated circuit at one point have to exit the chip. As the term 'wireless' directly implies this is done without a wire and thus the signal propagates unguided through a media which is typically air. For this transition between guided and unguided propagation, antennas are used as interfaces. The simplest view of antennas is the impedance matching of the guided signal to the characteristic impedance of the air. An detailed discussion of antennas is omitted from this dissertation as it would be beyond the scope. Similarly, concepts such as near-field and far-field will not be introduced, these can be found in [36], [42]. In this thesis, only the concept of polarization is discussed because it is closely related to the even/odd mode analysis, and an understanding of polarization is necessary to later understand and analyze the antenna measurements of the polarization diversity MIMO system.

2.3.1 Polarization

In guided media, propagation is described by the orientation of the E-field vector. In a single microstrip transmission line, the E-field is oriented vertically within the substrate, while in differentially coupled lines, the E-field is oriented horizontally between the two conductors. Similar E-field configurations can be found in waveguides with the description of the propagation modes. In unguided media, however, the orientation of the E-field, or rather the existence of E-field vectors along the propagation direction, is called polarization. Polarization is derived from the plane wave generated by an antenna in its far field. In the far field, the E and H field vectors are orthogonal to the propagation vector (Poynting vector).

In a Cartesian coordinate system, the presence of only one E-field vector in the x- or y-axis produces linear polarization. The presence of both vectors at the same time is called circular polarization (for equal vector lengths) or elliptical polarization (for different vector lengths) as shown in Fig. 2.8.

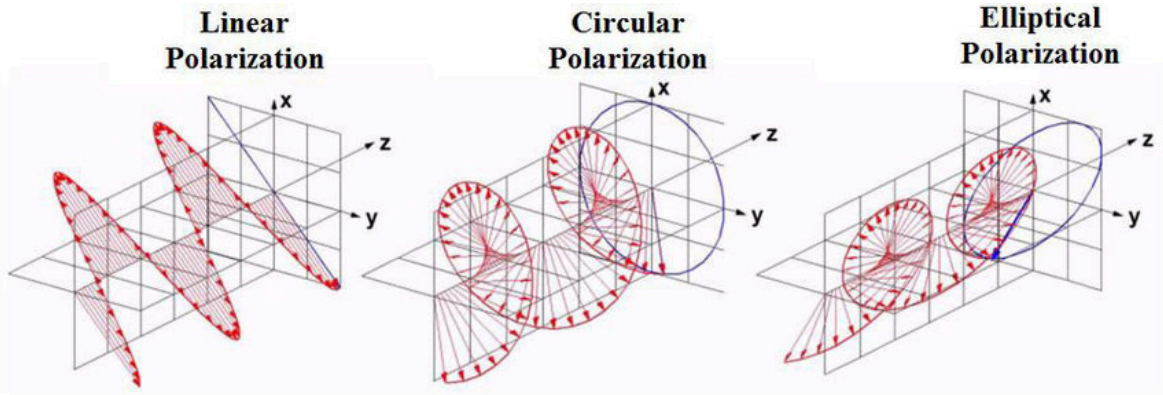

Figure 2.8: The three typical cases of polarized Waves: linear, circular and elliptical.

Since this dissertation focusses on electrically generated communication, the wave polarization is generated by the used antenna. In case of linearly polarized antennas, both receiver and and transmitter antennas should be aligned to avoid polarization losses. This polarization is typically used when the orientation of the antennas is fixed and unlikely to change, e.g. antennas in automotives and FM broadcasting stations. In contrast to this, circular polarization has the advantage of being orientation-independent. In an ideal circular polarized link, both transmitter and receiver can be turned orthogonally to the propagation direction without any first-order losses. Additionally, communication 'partners' using linear polarized antennas can still receive circular polarized waves with a fixed polarization loss of 3 dB as only one vector is received. Due to this orientation independence, circular polarization has a distinct advantage over linear polarized antennas. However, circular polarized antennas have an added level of complexity as both E-Field vectors need to be exited at the same time. For this, typically 90°generators are needed to ensure the orthogonality in the

excitation. The phase difference between the two E-Field vectors also determines the turning direction of the polarization. For a phase difference of 90°between E_y and E_x, the circular polarization is right turning (RCP), while a phase difference of -90°causes a left turning circular polarization (LCP).

Both right and left turning circular polarization can exist at the same time and are ideally isolated from each other due to this phase difference. Optimum isolation is only achieved for ideal circular polarization, any derivation either in phase or amplitude of the two E-Field vectors leads to an elliptical polarization and results in cross-polar leakage.

For communication links with high bandwidth, this ideal state has to be achieved not only for the carrier but across the entire occupied bandwidth creating a big challenge in the antenna design but also assembly of both transmitters and receivers. To determine the quality of the circular/elliptical polarization, the axial ratio r can be measured which is the ratio between the major axis - the axis along which the E-Field vector is the longest - and the minor axis along which the E-Field vector is the shortest (see Fig. 2.8). Major and Minor Axis are always 90°shifted against each other in the rotational plane orthogonal to the propagation direction. For an ideal circular polarization, the axial ratio is 1 as both vector lenths are identical resulting in a unit circle for each rotational angle.

Additionally, the cross-polar discrimination (XPD) can be derived from the axial ratio by

$$XPD = 20 \log \left(\frac{r+1}{r-1} \right) \tag{2.15}$$

Obviously, for $r = 1$, the XPD is infinite, while already an axial ratio of 1.12 which is around 1 dB difference between the major and minor axis results in a XPD of around 25 dB. Since the XPD gives a level of distinction between two polarization, it is inversely proportional to the isolation between the two polarizations.

It should be noted that the antenna characterizations shown in this dissertation in Chapter 5 are performed with linear polarized test antennas in form of a horn antenna. As explained above, a linear polarized antenna is only able to receive one projection of the circular polarized wave at a time, therefore for the characterization of an antenna both major and minor axis need to be measured.

2.4 SiGe BiCMOS

As mentioned in Chapter 1, the existence and performance of electrical circuits approaching 300 GHz is ultimately limited by the used transistor technology. The circuits shown in this disseration are based on an advanced SiGe BiCMOS technology provied by IHP - Leibniz Institute for High Performance Microelectronics. While III-V compound semiconductor such as Indium phosphide (InP) recently have become popular for high frequency applications [43], their usage is limited by the low yield and more challenging integration. In contrast, silicon based technologies such as CMOS and BiCMOS allow the full integration of both digital and analog functions on the same die while producing high yield. As communication is ultimately linked to a high number of deployed devices, silicon technology based solutions make use of the economy of scale resulting in low costs.

The high frequency performance of a transistor technology is typically derived from the measured f_t and f_{max} with

- f_t being the maximum transit frequency, or unity current gain frequency, where the current gain is 1.
- f_{max} being the maximum oscillation frequency, or unity power gain frequency, with the power gain becoming 1.

f_t is derived from the small-signal current gain h_{21}, whereas f_{max} is derived from the unilateral (Mason) gain U. These values are typically verified up to 40 GHz, and then extrapolated to extract the respective f_t and f_{max} values. In circuit design, the upper limit for signal amplification is deemed between $f_{max}/2$ and $2f_{max}/3$, as that frequency region still has sufficient intrinsic gain to overcome the losses of matching networks [44].

With CMOS technology nodes having a f_t/f_{max} around 350/370 GHz for 22 nm FD-SOI [45] and finfet 22 nm CMOS with 300/450 GHz [46], most research using CMOS technologies has been focussed on D-Band communication systems [47]. While CMOS based communication systems operating above 200 GHz exist, the systems are typically operated subharmonicly [48]. As shown in [46], the f_t/f_{max} have their maximum for this transistor size, while the authors do not expect a further increase with future transistor nodes. These findings are also further supported by the amount of research using 45&65 nm CMOS. However, it should be noted that the fabrication costs drastically increase with smaller technology nodes making it increasingly less attractive for research. In contrast, SiGe HBTs have shown f_t/f_{max} frequencies up to 700 GHz, which has been the foundation for recent communication advances operating around 240 GHz [49],[50], [51],[20].

Based on the results of the two european projects DOTFIVE (grant agreement number 217110) and DOTSEVEN (grant agreement number 316755), the currently commercially available SiGe BiCMOS technologies SG13G2 by IHP and B11HFC by Infineon were developed with their respective successors SG13G3 and B12HFC under current development. In comparison to the previously pure SiGe HBT processes, the BiCMOS technologies allow the cointegration of both HBT and regular MOSFETs on the same wafer. This typically comes with the price of reduced f_t/f_{max}, however the detoriation is minor and thus still superior to available CMOS technologies.

The broadband 300 GHz amplifier presented in Chapter 3, the entire communication RF frontends shown in Chapter 5 and the -so far- only simulated results of the broadband TIA presented in Chapter 3 are implemented in a development variant of the SiGe BiCMOS technology SG13G3 of IHP. Due to the scope of this dissertation, a detailed description of this technology is obmitted, but can be found in [52], [53].

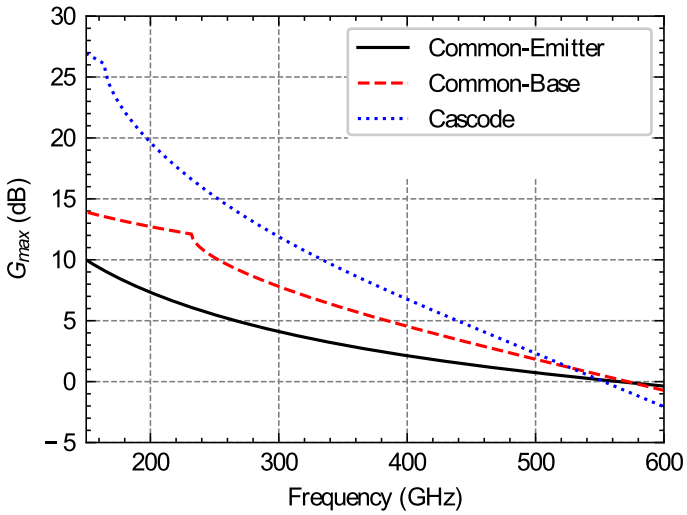

Figure 2.9: Simulated G_{max} of typical differential amplifier topologies. The cascode provides 4 dB more gain at 300 GHz compared to the common-base topology (CB), whereas the gain of the ideal common-emitter (CE) is lower over the entire frequency range due to the increased feedback.

Fig. 2.9 compares the maximum available gain (G_{max}) for different amplifier topologies biased at the f_{max} current density with devices sized to generate 10 dBm of saturated output power at 300 GHz. With a G_{max} of 12 dB, the cascode configuration (without inductive peaking) provides sufficient gain headroom at 300 GHz in this technology for power amplifier implementation given following implementation losses.

The improved f_{max} performance in comparison to the commercially available SG13G2 leads to a high maximum available gain at 300 GHz (see Fig. 2.9), especially in the cascode configuration (12 dB), which is commonly used for high frequency amplifiers [8], [54], [55] due to its improved gain and isolation. Based on these results, an implementation of communication systems operating at 300 GHz using this technology

is viable. The required LO and RF amplifiers can be implemented due to the high available gain. The other circuits needed in the transmitter and receiver design such as the LO frequency generation and the up- and downconversion mixers rely on the non-linearity of the used devices. In general, the non-linearity of SiGe HBT is higher than in CMOS FETs and it is expected to not be the limiting factor. The additional baseband circuits i.e. the transimpedance amplifier in the downconversion path operates at low frequencies where the transistor gain is very high.

2.5 Summary and Conclusion

This chapter reviews the basics of communication and its implementations in integrated circuits. Based on the Shannon-Hartley theorem, it is shown that bandwidth directly improves the channel capacity and thus the maximum data rates that can be achieved in a communication link. Considering both superheterodyne and direct conversion receivers, it can be seen that bandwidth improvements can most likely be achieved by using a direct-conversion receiver as the IF filtering bandwidth and amplification does not scale as fast as baseband bandwidth. However, when approaching carrier frequencies of 300 GHz, it also becomes clear that existing silicon-based technologies come to their limits, showing the need for advanced BiCMOS technologies. Similarly, as efficient matching becomes increasingly important at high frequencies and high bandwidth, on-chip signaling is reviewed.

Based on this, the following Chapter 3 will discuss the implementation of the required circuits for a broadband direct conversion transmitter and receiver operating at 300 GHz using the SG13G3 technology provided by IHP.

Chapter 3

Broadband Building Blocks

In this chapter, the implemented dual polarized transmitter and receiver are introduced. First, the general topologies of these is explained. Based on the block diagrams, the individual building blocks are discussed. First, the up- and downconversion mixers and their respective baseband amplification is presented. The transimpendance amplifier in the downconversion path is identified as a potential bottleneck and further improvements to this building block are shown. Continuing on this, the power amplifier is discussed, which is used in both the LO generation paths and the RF path of the transmitter. Finally, the LO frequency generation utilizing frequency multiplier stages and bandpass filtering for harmonic suppression is presented.

3.1 Receiver & Transmitter Implementation

As described in Chapter 2, the direct conversion receiver has advantages over its superheterodyne counterpart in its complexity, size and power consumption. By relying on a single downconversion stage, challenging IF filtering and amplification is removed. Thereby, the total bandwidth of a Zero-IF receiver is defined by its RF receive path i.e. the matching between the antenna and the downconversion mixer and the baseband amplification. The receivers block diagram is shown in Fig. 3.1, with the respective TX block diagram shown in Fig. 3.3.

The implemented receiver utilizes polarization diversity for MIMO application similar to [56]. The here presented receiver uses a shared LO generation path for both left and right turning circular polarization which is in contrast to the implementation

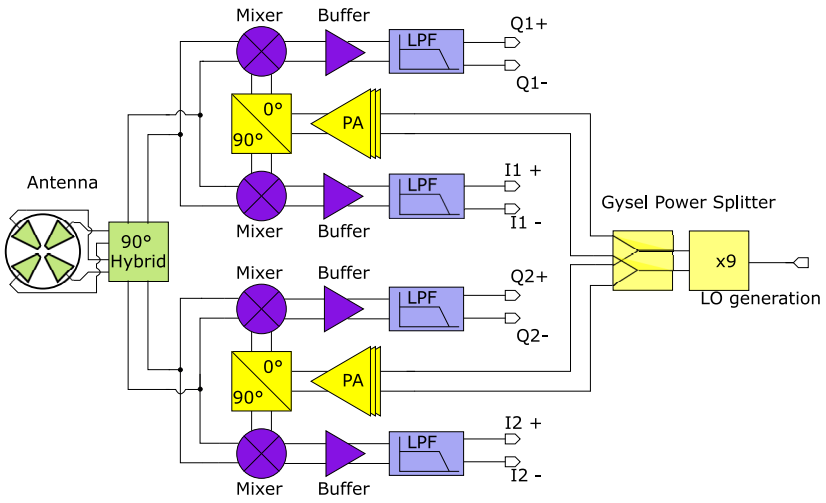

Figure 3.1: Block diagram of the receiver. The different parts are colored accordingly. The dual-polarized antenna is set in green with the downconversion mixers set in purple. The LO generation is yellow, while the baseband section blue.

in [56] with two independent frequency multiplication chains. As the receiver receives both left and right turning circular polarization (as defined in Chapter 2), the downconversion is separated accordingly, creating a vertical symmetry plane in the receiver layout. This symmetry plane creates a natural boundary in the layout for signal routing which will further be explained in the next section discussing the downconversion path.

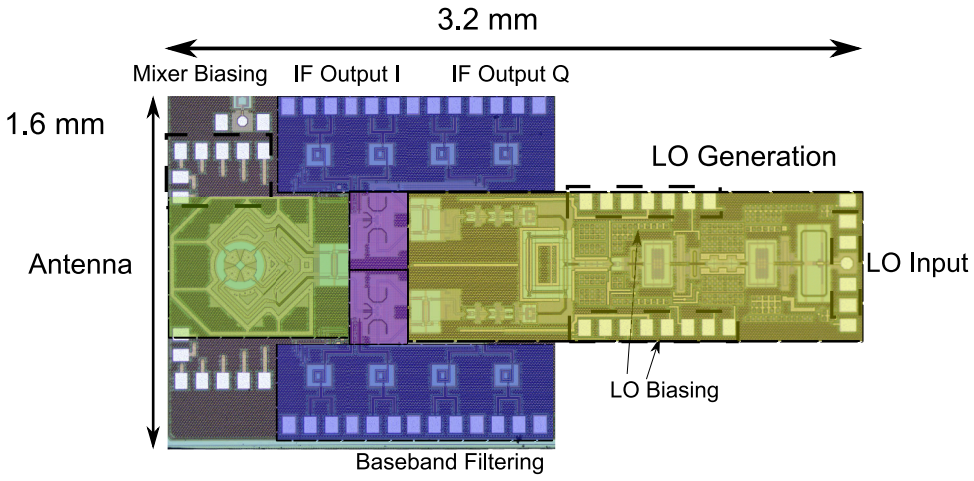

Figure 3.2: Layout of the dual-polarized receiver. Similar to the transmitter, the different parts are colored for optical guidance. The dual polarized antenna (green) is directly connected to the downconversion mixers (purple). Their output is fed to the baseband filtering (blue), while the LO generation (yellow) is routed into the base of the switching quad. The total size of the receiver is 5.12 mm^2.

In contrast to the receiver, the transmitter implementation is independent to the architectural decision of the receiver. Therefore, the block diagram itself is a modification of the well-known transmitter block diagram with added complexity due to the polarization diversity (see Fig. 3.3). Similar to the receiver, the transmitter's upconversion path is separated in left and right turning circular polarization. In the following, first the antenna creating two independent circular polarized waves is described as its design is identical for both transmitter and receiver.

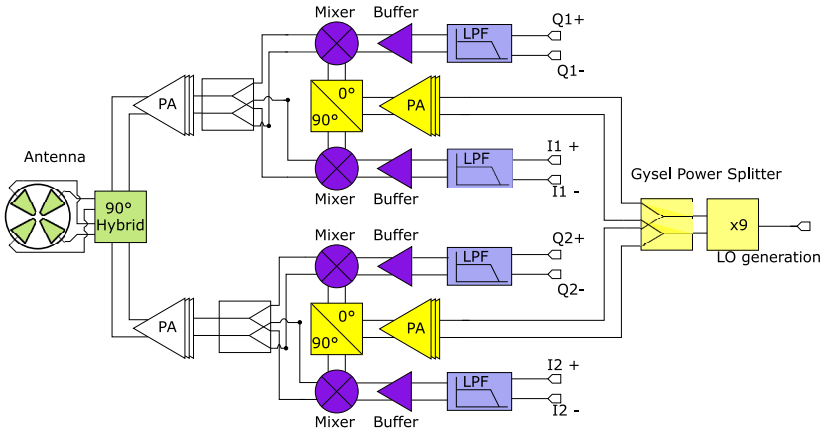

Figure 3.3: Block diagram of the transmitter. The different parts are colored accordingly. The dual-polarized antenna is set in green with the upconversion mixers and their combiner set in purple. The LO generation is yellow, while the baseband section blue.

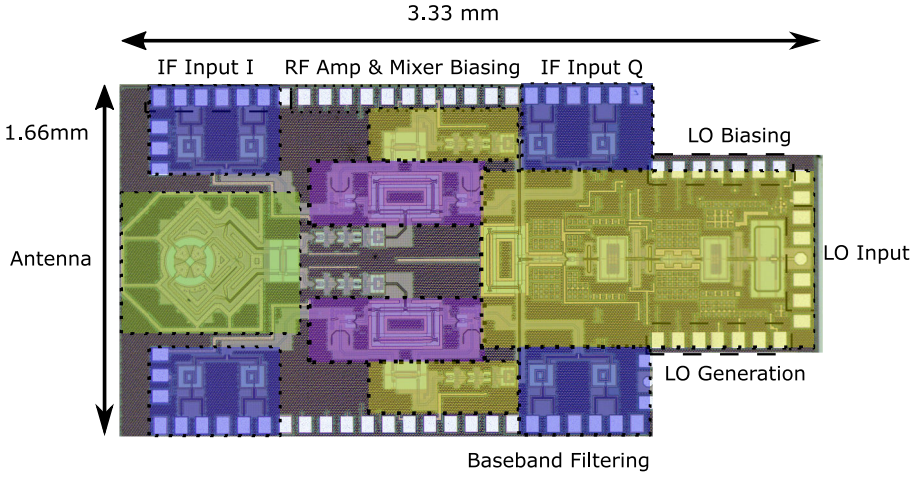

Figure 3.4: Layout of the dual-polarized transmitter. The different parts are colored accordingly. The dual polarized antenna is set in green with the upconversion mixers and their combiner set in purple. The major area of the transmitter is made up by the LO generation (yellow), while the baseband section (blue) will be discussed in the next chapter. The total size of the transmitter is 5.53 mm^2.

3.2 Antenna

Due to the decreased wavelength in the mmWave frequency range, on-chip integrated antennas are feasible. The decreased wavelength shrinks the antennas down to a size comparable to the connected integrated circuit. However, the BEOL sets limitations to the antenna integration and oftentimes - in case of patch antennas - leads to a low radiation efficiency.

To overcome the unfavorable properties of the silicon stack, lens-integrated antennas have been implemented in the past [57]. In this dissertation, transmitter and receiver use a circular polarized lens-integrated dipol antenna similar to [56] as shown in Fig. 3.5. The radiator design is similar to [58], for circular polarization however the two radiators must be excited with a phase difference of 90°. As the antenna is fed through differential transmission lines, a differential coupled-line 90° hybrid is used (see Fig. 3.5). Contrary to regular 90° hybrids, the isolation port is replaced by another differential input. Thereby, both positive and negative phase differences of 90° can be generated allowing for simultaneous generation of both left and right turning polarization.

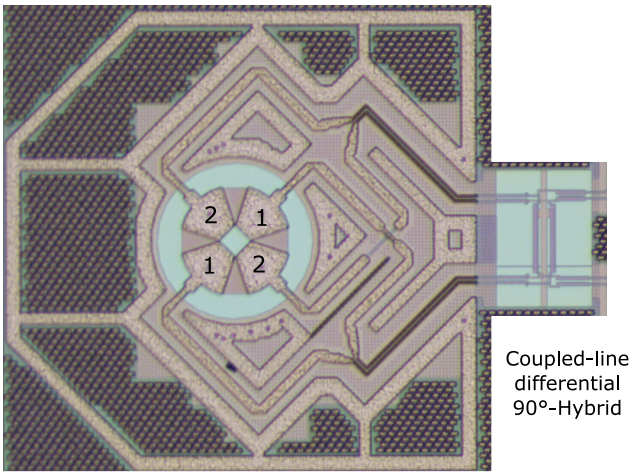

Figure 3.5: Antenna micrograph. The antenna consists of two orthogonal linear radiators marked with 1 and 2 and the coupled-line differential 90°-Hybrid.

Due to the intrinsic power splitting, the antenna has an increased resistive loss in comparison to its linear polarized counterpart. For reduced complexity, the resulting simulated S-parameters of the regular three-port hybrid (Fig. 3.6) are shown which is also used in the LO generation to provide the orthogonal LO signals for the I and Q mixers.

The simulated S-parameters of the three port 90° Hybrid can be seen in Fig. 3.7. The return losses (S_{11}, S_{22} & S_{33}) are below -15 dB in the entire observed frequency range. The phase difference between the two outputs shows a perfect 90° phase differ-

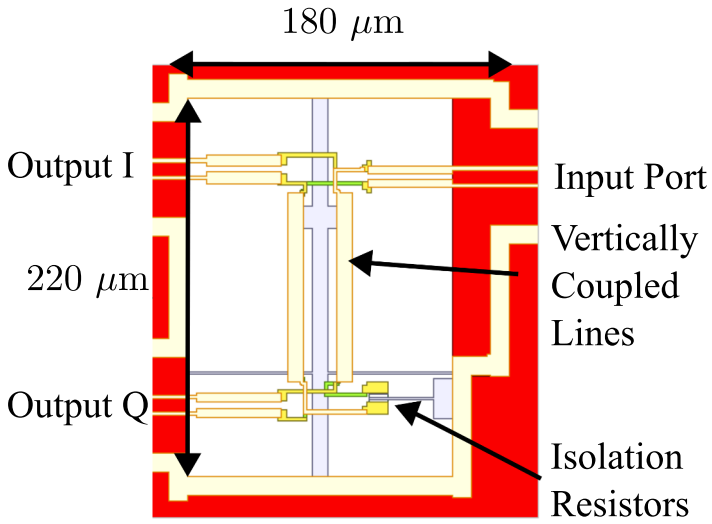

Figure 3.6: Layout of the three-port coupled-line hybrid as used in the LO generation. To generate the dual polarization in combination with the linear radiators of the antenna, the isolation resistor is replaced by an additional input port.

ence starting from 250 GHz. In the antenna, a non-ideal phase difference would cause potential leakage between the two circular polarizations as it can directly be converted to an imperfect relation between the two excitations, therefore this hybrid is optimized for maximum amplitude and phase stability.

In the assembly process, the backside of TX and RX chipset is glued to the flat surface of a hyper-hemispherical silicon lens. By using a silicon lens interfacing with the thinned subtrate of the chipset a steady media transition between the substrate and the silicon lens is achieved. This reduces reflections created by chip to lens interface. The chipsets main radiation is directed through its substrate and silicon-lens and thereby called backside radiation. The curvature of the lens here helps to reduce surface currents at the outer boundary of the lens, again reducing possible reflections.

For the lens-integrated antennas, hyper-hemispherical lenses with a diameter of 9 mm and an extension length of 1.2 mm are used. Alternatively, a lens extension length of 1.4 mm can be used which leads to an increased directivity. The lens extension creates a focal spot of the lens which is ideally in the integrated circuit. For circular-polarized antennas, the antenna center must be placed at the center of the lens for both cartesian directions to ensure maximum circularity.

The simulated results of the antenna can be found in [56], whereas the measured directivity is later shown in Chapter 5.

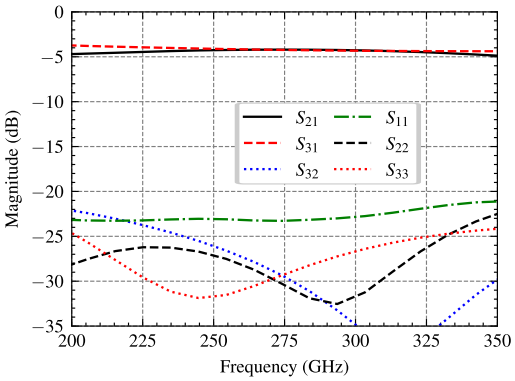

(a) Simulated S-Parameters of the Hybrid.

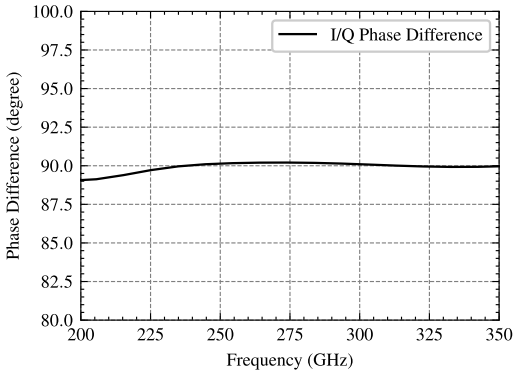

(b) Phase Difference between the orthogonal outputs of the Hybrid.

Figure 3.7: Simulated S-Parameters of the three-port coupled-line 90° Hybrid. Each input and output shows a broadband match over the entire observed frequency range. The S_{21} and S_{31} traces show the expected insertion loss behavior associated with coupled-line couplers. The phase difference between S_{21} and S_{31} show a perfect 90° phase shift starting from 250 GHz.

3.3 Up-/ Downconversion

Up- and Downconversion is the essential part in a communication part as it allows for modulation and demodulation of the carrier frequency with the baseband information stream. In the upconversion, the broadband baseband signal is mixed with the LO signal to achieve a double sideband signal in the desired RF channel. To achieve this mixing, the following upconversion stage is used.

3.3.1 Upconversion

In the implemented transmitter, the upconversion mixer is based on an active mixer topology called Gilbert Cell [59] as shown in Fig. 3.8. Here, the mixer consists of two parts, the switching quad & transconductance pair. The mixing of the applied LO signal and IF signal takes place in the switching quad which is alternately switched on and off by the provided LO swing.

The IF signal is provided by the transconductance pair converting the applied signal into the shared collector/emitter current. The transconductance stage by itself acts as a buffer amplifier. In addition to this, a emitter-follower (common-collector) is used to create a broadband match between the signal pads which will later be shown in Chapter 4 and the base of the transconductance stage. For optimum match, the emitter-follower uses a pulldown resistor creating the desired input resistance.
The emitter-follower and transconductance pair here are responsible for the linearity

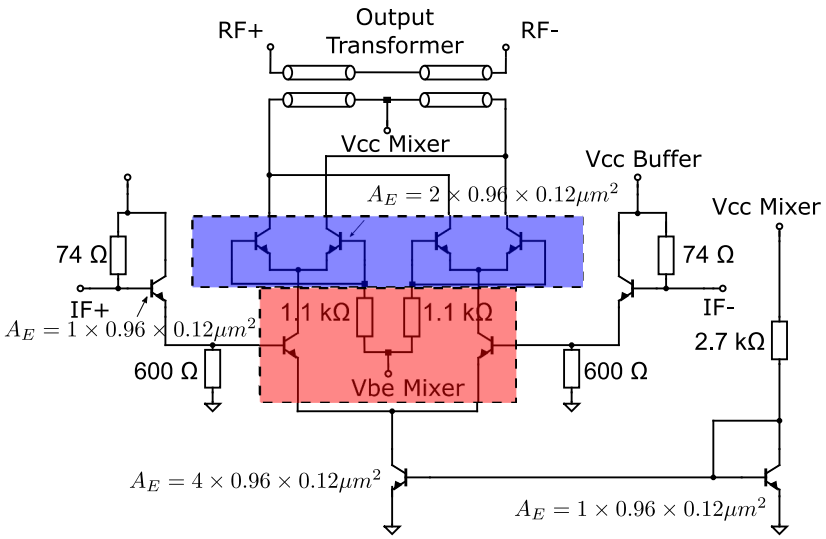

Figure 3.8: Schematic of the upconversion mixer. The transistors in both the switching quad (red) and transconductance stage (blue) have the identical emitter area of $A_E = 2 \times 0.96 \times 0.12\ \mu m^2$.

which is later measured and discussed in Chapter 5. The differential architecture of the switching quad and transconductance pair allows for 'natural' suppression of the even harmonics generated by both the LO generation path and the nonlinearity of the transconductance pair.

The implemented transmitter uses quadrature upconversion. In this case, two independent upconversion mixers are used to generate both I and Q passband signals that are combined in phase and then fed into a shared power amplifier as shown in the layout (Fig. 3.9). For output matching of the upconversion mixer to the RF frequency, a asymmetric coupled-line transformer is used similar to the one used in the power amplifier output as presented later in this chapter and in [own1]. As the transistor size of the switching quad transistors is smaller than the one used in the power amplifier, the output transformer is adapted to the provided output impedance of the transistors. As stated in [own1], the output transformer provides high common-mode rejection in the amplifier, with a similar rejection expected for the mixer output.

As the I and Q passband signals are ideally perfectly orthogonal to each other, the two signals and mixers should not interfere with each other. Due to this, I and Q recombination is often found in form of current combining [60]. However, with increased design frequency, the passband generation derivates from its ideal operation. With increased frequency, the transistors in the switching quad do not operate as ideal switches as the required square waves cannot be generated leading to a limited slew rate. Therefore, the switching quad has no clearly defined on and off state causing undesired signal leakage.

Similarly, the output impedance of the switching quad is not constant as ideally only two transistors should conduct current in a half-cycle while in general the isolation of the transistors also decreases.

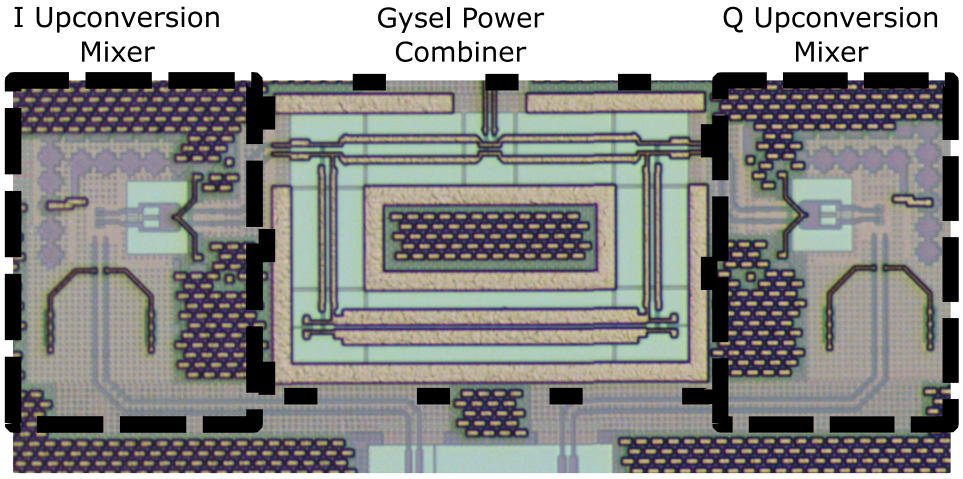

Figure 3.9: Micrograph of the two upconversion mixers with the Gysel power combiner in between.

To mitigate these effects, a Gysel power combiner is used to combine the I and Q passband signals as shown in the micrograph of the upconversion section (Fig. 3.9). In contrast to current combining, the Gysel power combiner offers high isolation between the two inputs which is expected to reduce potential leakage between the two mixers. The Gysel power combiner is chosen for power combining as it can be implemented differentially [60] which is challenging for the more common Wilkinson power combiner in its single-ended configuration.

In contrast to current combining however, a Gysel power combiner has an increased insertion loss which is here traded against the increased isolation of between the two mixers. The layout of the Gysel power combiner can be seen in detail in Fig. 3.10. Similar to branchline hybrids, the Gysel power combiner relies on the destructive and constructive interference of the individual branches for in-phase power combination. In addition, isolation resistors are placed at the respective shorter branches to provide a termination for undesired signal propagation inside the combiner.

The respective insertion and return loss of the Gysel power combiner can be seen in Fig. 3.11. While both input signals are transmitted to the output, the power combiner contributes additional losses. At the same time, the two inputs (Port 1 & Port 2) are isolated from each other in the center of the frequency band by >20 dB. As visible in the return loss, the Gysel power combiner provides a broadband match at each port.

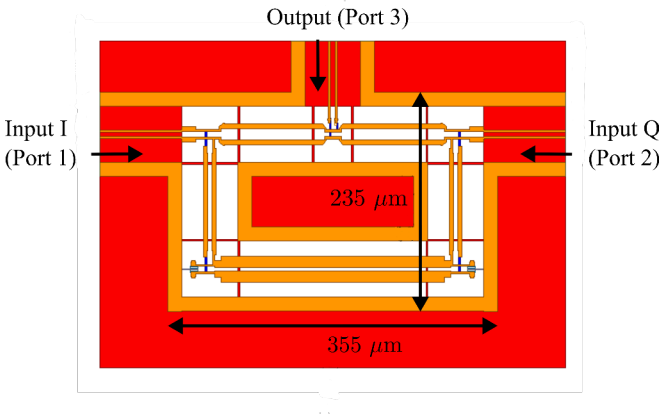

Figure 3.10: Gysel power combiner layout.

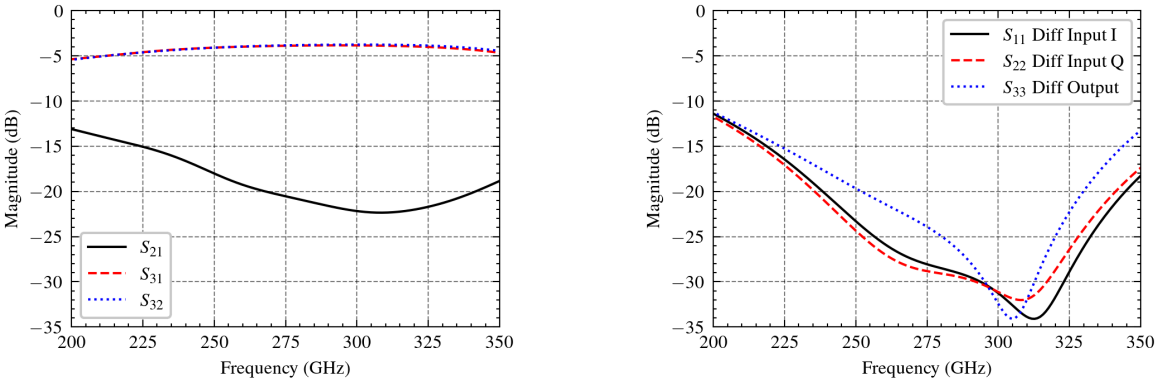

(a) Insertion loss of the Gysel power combiner.

(b) Return loss of the Gysel power combiner.

Figure 3.11: Gysel power combiner insertion loss and return loss. The respective input ports (Port 1 & Port 2) are located on the sides, with the output port (Port 3) at the center. The Gysel power combiner provides a low insertion loss on the power combining paths (a) while each individual port is well matched to the 100 Ω differential port impedance.

The here presented Gysel power combiner is not only used for the power combination of the outputs of the I/Q mixers. As the two polarizations in the dual-polarized TX and RX share the same frequency multiplication stages, the LO signal is split at the output of the final frequency tripler. As the Gysel power combiner is purely passive, it can be used reciprocally.

3.3.2 Downconversion

For Downconversion, the received RF signal from the antenna is fed into the emitter of the switching quad as shown in Figure 3.12. The LO signal generated by the LO frequency multiplication stages is applied to the base of the switching quad, while the downconverted IF signal is extracted at the collector. The emitter is chosen as the RF interface as its low Q-Factor allows for broadband matching. However, the antenna does not provide a DC ground path for the downconversion mixer, therefore the RF matching includes transmission line stubs for DC grounding. The transistors in the switching quad have an emitter area of $A_E = 2 \times 0.96 \times 0.12\ \mu m^2$ similar to the upconversion mixers.

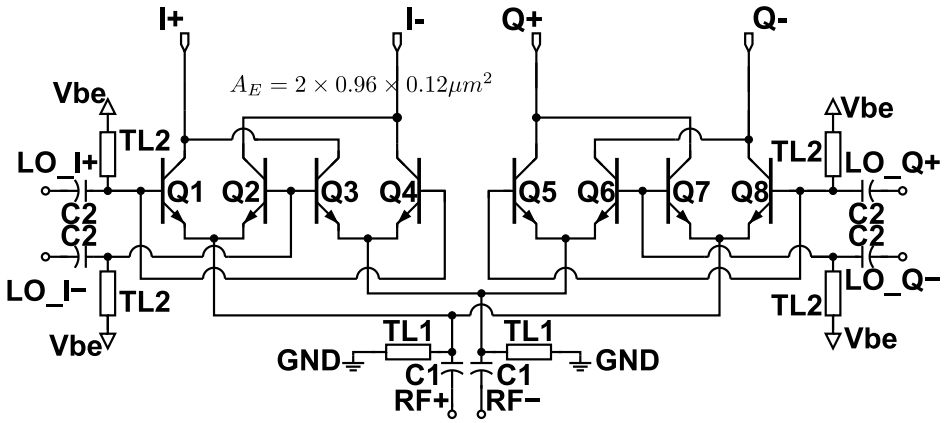

Figure 3.12: Schematic of the downconversion mixer. The received RF signal is fed into the emitter of the switching quad. To provide the required DC ground, the RF matching includes transmission line stubs for grounding. The LO signals are fed into the base, while the downconverted baseband signal is extracted at the collector and fed into the following Transimpedance Amplifier (TIA).

In receivers, the down-converted signal is generated by applying a load to the IF output of the down-conversion mixer. In previous designs [61], [60] a real, purely resistive load was connected to the output of the down-conversion mixer to generate the down-converted signal, which is then fed into an emitter-follower for matching to the IF pads and PCB. This purely resistive termination leads to low Conversion Gain (CG) of the down-conversion mixer. By connecting a TIA to the output of the switching quad [33], CG can be improved. Thereby, CG is then limited by the gain-bandwidth product of the TIA.

The implementation of the TIA is made under spacial constrains as shown in Fig. 3.13. The amplifier should be placed as close as possible to the switching quad for minimum on-chip loss. However, switching quad also is connected to the antenna and LO generation. For optimum isolation between the RF and LO path operating at sim-

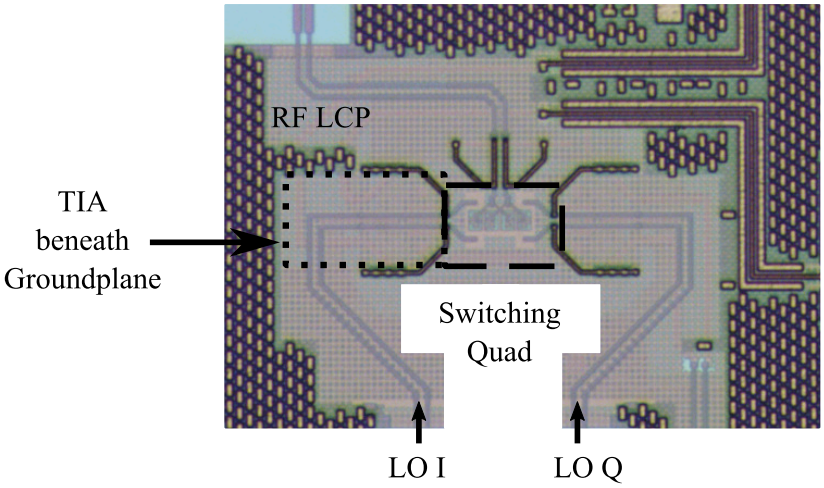

Figure 3.13: Micrograph of the downconversion stage. The switching quad is indicated in the center of the micrograph. The two orthogonal I/Q LO signals are fed along the horizontal axis, while the RF signals is fed from the antenna connected at the top. Thereby, both RF and LO paths are orthogonal to each other for minimal coupling. The baseband TIA is placed beneath the groundplane to reduce its influence on the high-frequency routing.

ilar frequencies, these paths should be routed orthogonal to each other on the topmost layers inside the transistor technologies back-end-of-line (BEOL) as the topmost layers are optimized for on-chip signal propagation as shown in the micrograph (Fig. 3.13). At the same time, the implemented receiver is divided into two polarizations along its vertical axis, in the shown micrograph this forces the baseband outputs to be routed to the right side. Therefore, the RF routing and the dual-polarization forces a TIA implementation below the groundplane. The presence of the groundplane on top of the transimpedance amplifier also prohibits the use of inductors as part of the matching circuits. Thereby, broadband amplifier topologies such as distributed amplifiers [own2] are not feasible as they require inductors for matching.

Therefore, a baseband amplifier relying on purely resistive matching has to be implemented. In Fig. 3.14, the implemented feedback transimpedance amplifier is shown. Similar to previous designs [33], the generated collector current of the switching quad is shared with the input of the TIA. For direct-conversion receivers, this is necessary as DC blocking between these two stages creates a bandpass response and - depending on the used modulation scheme and data - can cut off low frequency components of the received analog signal. This causes intersymbol interference which eventually leads to EVM detoriation.

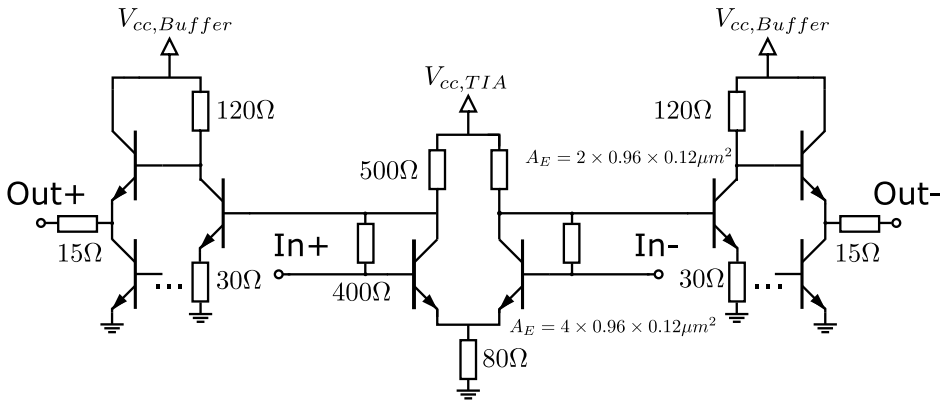

Figure 3.14: Schematic of the implemented TIA. The downconverted baseband signal is fed into the two transistors at the center. The feedback loop is used to improve the bandwidth in comparison to a regular resistive load. For broadband matching, an additional buffer stage is implemented. TIA and buffer amplifier have separate bias voltages. The current sources for biasing are omitted from this schematic for increased visibility.

Transimpedance amplifiers are an extensive research topic and thereby will not be described here in detail. For a general discussion, the transimpedance provided by the amplifier and its bandwidth create a tradeoff similar to the gain/bandwidth tradeoff [62]. In case of the transimpedance amplifier in a receiver, this tradeoff is between the possible conversion gain and its overall bandwidth. As described in Chapter 2, in a direct-conversion communication system the bandwidth of the baseband circuits is half of the used RF bandwidth. The largest bandwidth in the IEEE Standard is given with 69 GHz, thereby ideally the baseband bandwidth should be 34 GHz.

In the implemented TIA, a baseband bandwidth of >30 GHz is shown in Fig. 3.15. The displayed CG is identical for both sidebands, indicating that the designed baseband bandwidth closely matches to the required 34 GHz. In receivers, an increased LO signal power or an increased base-emitter voltage of the switching quad should ideally lead to a higher CG. Both LO signal power and base-emitter voltage cause a higher collector current, which is then applied to the TIA. At the same time, the LO power is generated by nonlinear circuits, therefore its output power cannot be varied linearily. Therefore, the operation of the downconversion mixer in combination with frequency multiplication stages is challenging due to the multiple variables influencing both conversion gain and bandwidth.

In the implemented TIA, the TIA is not able to handle variations in the LO power. Here, the increased collector current breaks the feedback loop and eventually decreases the conversion gain and the generated bandwidth as shown in Fig. 3.15. For single-polarized receiver implementations, the LO power generated by the frequency multipler stages and following power amplifier is up to 9.8 dBm [own1], for this LO power levels,

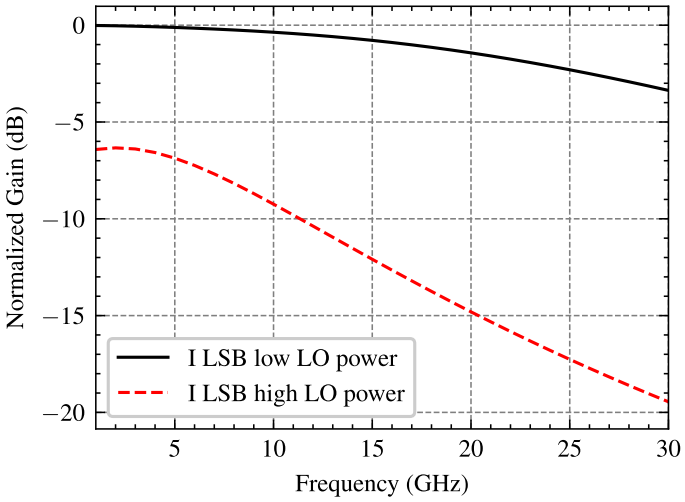

Figure 3.15: Simulated normalized TIA conversion gain for high (8 dBm) and low (4 dBm) LO power. The TIA is simulated in combination with the down-conversion mixer and an ideal power source at 260 GHz. While a 3-dB baseband bandwidth of 30 GHz can be achieved in the regular operation, the limited power handling drastically reduces the bandwidth down to 12 GHz.

the TIA is not able to provide gain. Therefore, the conversion gain of the receiver is limited by the baseband TIA and not by the LO generation.

In addition to this, the differential output for both I and Q is fed into different types of transmission lines. While the output of the TIA amplifying the signal of the I-Mixer is fed into two single-ended shielded transmission lines seen in the top right corner in the micrograph (Fig. 3.13), the output of the Q-Mixer's TIA is connected to coupled lines. As described in Chapter 2, the propagation in differential lines and single-ended lines is fundamentally different.

While both may provide a characteristic differential impedance of 100 Ω, the propagation factor γ is different resulting in different insertion loss and phase velocity for the two lines as shown in Fig. 3.16. The insertion loss of the two outputs shows reduced bandwidth. In comparison to the implemented TIA bandwidth (Fig. 3.15), the baseband 3-dB bandwidth is reduced to 17 GHz for the I channel and 25 GHz for the Q channel respectively. Similarly, the phase behavior over frequency is not identical for the two outputs, while the I channel shows a linearly decreasing phase, the Q channel displays a curvature. Thereby, the implemented baseband routing in the receiver will not only limit the total bandwidth of the transmitter, it also introduces additional I/Q imbalance due to the amplitude and phase mismatch.

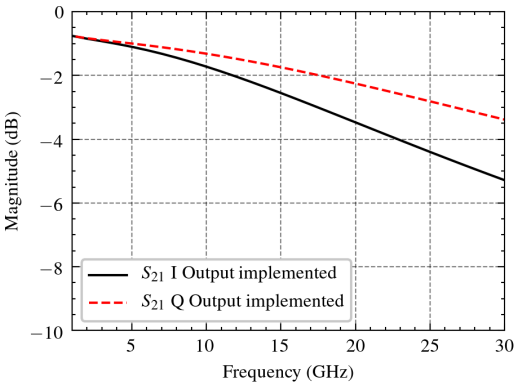

(a) Insertion loss of the implemented baseband routing.

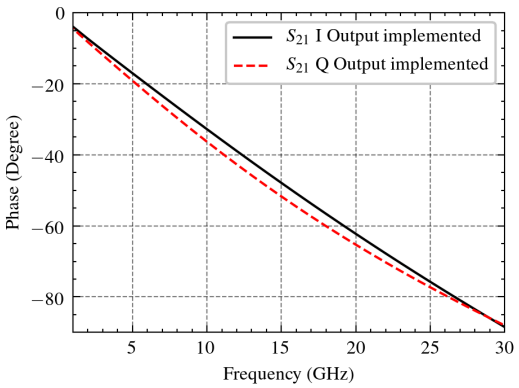

(b) Phase of the implemented baseband routing.

Figure 3.16: Insertion loss and phase of the implemented TIA output baseband routing. The implemented baseband routing at the individual outputs of the TIA show differences in the insertion loss (a) which increases with frequency. Similarly, the phase behavior (b) of both channel routings is not identical.

Given that these shortcomings in the baseband path of the receiver were found in the post-layout simulation after the tape-out, changes have not been implemented in fabricated hardware. In the following, solutions to the phase velocity problem and the power handling capabilities of the transimpedance amplifier are discussed.

For the different transmission line implementations in the I and Q path, the required routing below the ground plane to avoid interaction with the RF and LO routing creates transmission lines with a low characteristic impedance as the capacitance towards both the ground and substrate is very high. However, the signal routing below the groundplane cannot be completely avoided as the baseband signals need to be routed towards the pads without coupling into both the RF and LO path. For this, the groundplane was 'cheezed', i.e. the groundplane was partially removed along the signal routing as shown in Fig. 3.17. By this partial removement of the groundplane, the introduced line capacitance and losses were reduced. Eventually, both I and Q signals are connected to CoPlanar Waveguide (CPW) and then routed to the on-chip filter structures and signal pads.

Thereby, the insertion loss of the two outputs can be made equal as shown in Fig. 3.18. Additionally, the implemented transmission lines do not limit the bandwidth of the implemented TIA as the fast roll-off is not visible in this routing variant. As both outputs now use shielded single-ended transmission lines, the phase velocity of both outputs is identical. This is directly visible in the optimzed phase.

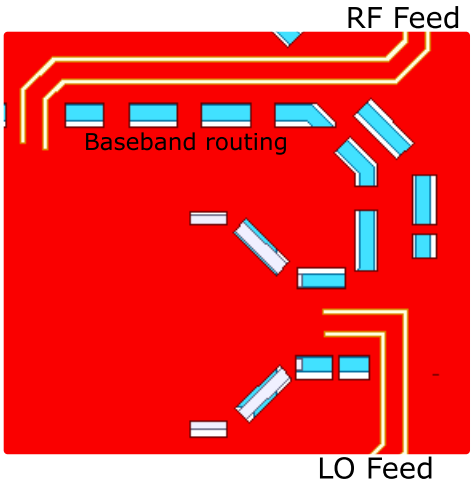

Figure 3.17: HFSS view of the cheezed groundplane above the baseband routing. The LO and RF feed are added for orientation. The holes in the groundplane are $\leq$ 10 µm long to avoid coupling between the baseband and the high-frequency routing.

The impact of this optimization becomes more visible when the phase difference between the two outputs is calculated and the two variants (implemented & optimized) are compared (Fig. 3.19). The linearly increasing phase difference in the optimized routing can be compensated using modern signal equalization in the baseband demodulation as it is directly related to the group delay and the physical length of the used transmission lines.

For bandwidth extension at higher LO power levels, the TIA was redesigned. The improved power handling is achieved by increased sizing of the transistors in the shared current path. Therefore, the transistors are able to handle higher input currents without breaking the feedback loop. As stated in [62], the total bandwidth is dependended on the desired gain and the gain of the feedback loop. During the layout, the spacial constraints given to the initally implemented TIA were kept. Again, the groundplane creates additional capacitance along each used metal strip. Thereby, the used resistors in the TIA have to be changed in comparison to the ideal schematic simulation to maintain the desired bandwidth.

In the receiver measurements (Chapter 5), the total noise of the implemented receiver was measured. In the measurement, the common mode noise floor - visible when only one single-ended output is connected to the spectrum analyzer- was about 20 dB higher than the measured differential noise. This noise is possibly related to the physical distance of the bypass capacitors to the critical nodes in the implemented receiver. For this, additional bypass capacitors in close vicinity to the critical nodes, namely the bases of the current mirros were placed. This resulted in reduced flicker noise at higher frequencies in the simulations. The resulting simulated CG of the improved

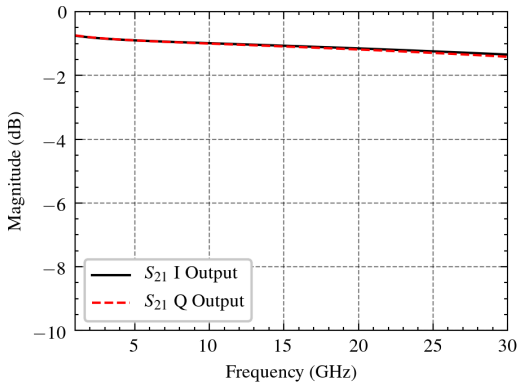

(a) Insertion loss of the optimized baseband routing.

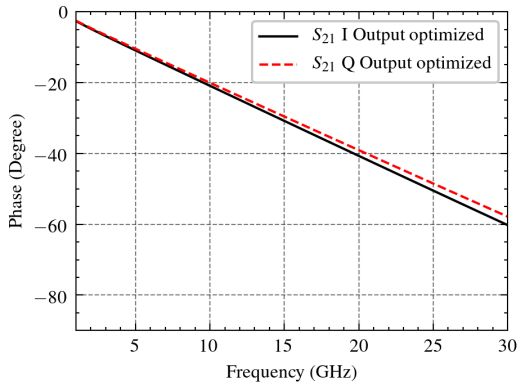

(b) Phase of the optimized baseband routing.

Figure 3.18: Insertion loss and phase of the optimized TIA output baseband routing. The optimized baseband routing at the individual outputs of the TIA show identical insertion loss (a). Similarly, the phase (b) of both channel routings decreases with frequency for both channels with similar rate.

TIA can be seen in Fig. 3.20. The sharp gain roll-off seen in the original TIA (Fig. 3.15) for high LO power levels is removed, by introducing another peak at 18 GHz, the overall bandwidth was extended with a total baseband 3-dB bandwidth of 36 GHz.

Overall, it can be seen that the design of the baseband amplifier in the receiver is crucial to its bandwidth. In contrast to transimpedance design for photo-detectors, the design process must include the mixer and LO excitation for correct load and current modeling for the baseband amplifier. While the shortcomings of the implemented design were found after its implementation during the characterization process of the receiver, a pathway and layout implementation for improved baseband bandwidth and I/Q imbalance is shown.

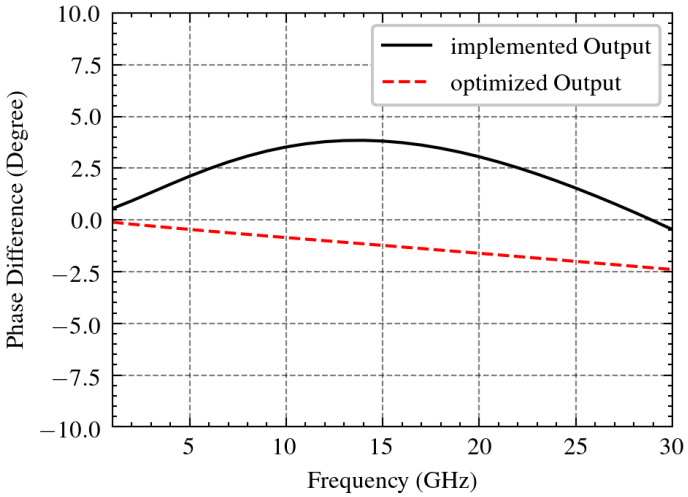

Figure 3.19: Phase difference between the outputs for the implemented and optimized baseband routing. Here, it can be seen that the phase difference slightly increases with increasing frequency for the optimized layout, while the implemented layout sees its phase difference maximum at 15 GHz.

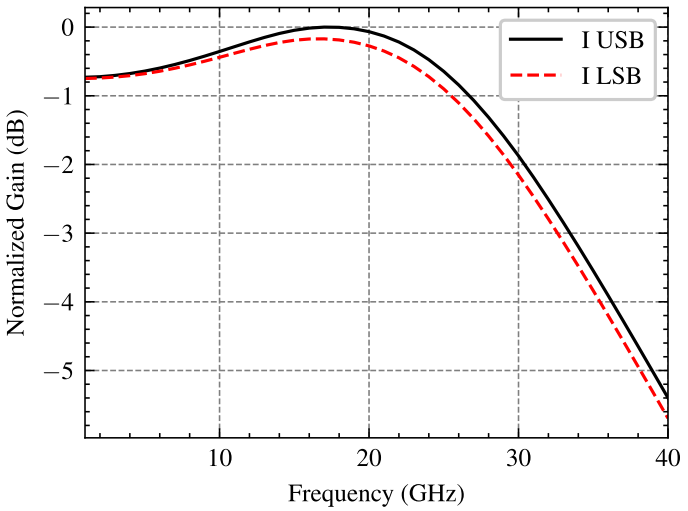

Figure 3.20: Simulation results of the improved TIA including a full EM-simulated layout for high LO power handling. The bandwidth can be improved for both sidebands above 33 GHz, equal to a total RF bandwidth of 66 GHz.

3.4 RF Power Amplifiers

One of the key building blocks in communication systems is the power amplifier, that is typically situated as the last element in a transmitter. In both the receiver and transmitter, a power amplifier is used in the LO generation as well to provide the necessary LO power for mixer operation. With increasing frequency, the design of such power amplifiers becomes more and more challenging, as the possibly generated power in the device technologies decreases with frequency (Johnson Limit) [63].

To find the optimum load conditions for power amplifiers, different approaches to determine the optimum load impedance for the used transistors are used. The load line approach is a graphical representation of the optimum voltage and current relation to maximize both voltage and current at the output of the amplifier based on the DC response (IV curves) of the transistor. As the name implies, the load line is purely resistive and does not take reactive components into account. For this, the commonly load-pull simulation/measurement [64] offers an extended approach which is ultimately independent of the design frequency.

Additionally, loadline theory for power matching is not valid anymore when approaching the $f_{max}/2$ limit [65]. Therefore, the transformer design must be improved to achieve the desired bandwidth and output power at 300 GHz. The here presented power amplifier has been published in [own3], [own1] and therefore will not be discussed in detail. Instead, in this part design considerations missing from the previous publications as well as a brief summary of its performance will be given. Thereby, the following transmitter and receiver RF characterization in Chapter 5 can be connected to the individual building block performance presented in this Chapter.

As shown in Fig. 3.21, the implemented 300 GHz power amplifier is based on a 3-stage cascode. In Chapter 2, it was shown that the used transistor technology (IHP SG13G3) provides sufficient available gain up to 300 GHz for amplifier implementations, when a cascode topology is used. Due to the high available gain, it was decided that the layout implementation for the core transistor as shown in Fig. 3.22 should ideally be as invisible as possible. I.E. the added input and output vias and transmission lines as well as the common-emitter to common-base interconnect should not change the input and output impedances of the cascode, or at least variations of these impedances should be minimized as shown in Fig. 3.23.

This design decision is in contrast to high frequency designs found in other technologies [own4], [66], [67]–[69]. Both Cross-coupling amplifier and G_{max}-Core amplifier topologies are used in technologies with low available gain at the design frequency.

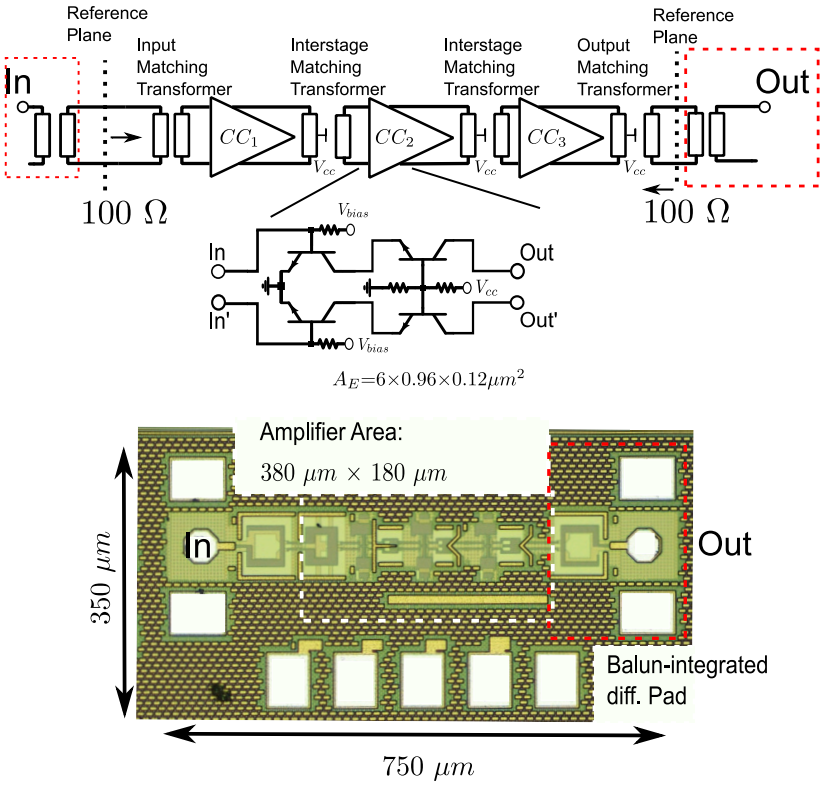

Figure 3.21: Block diagram and chip micrograph of the 3-stage PA. On-Chip Baluns are used at the input and output for probing. The biasing of the used cascode cells (CC) is shown for one cell. The base of the common-base stage is biased through a resistive voltage divider connected to the supply voltage (Vcc) which is fed through a center tap in the interstage and output transformers. The base of the common-emitter stages is biased separately through with 1 kΩ resistors connected to the base. ©IEEE [own1]

Both approaches allow to boost the available gain in a limited frequency range, either by adding additional capacitors to reduce the feedback or embedding the transistors in a - ideally - lossless matching network. These changes do not only cause peaks in the G_{max} curve, they also change the input and output impedances of the transistors. Especially, in G_{max}-Cores the optimization is accompanied by an accelerated gain roll-off which again makes broadband amplifier design increasingly challenging. In addition, the feasibility of G_{max}-Core amplifiers for broadband power amplifiers has not yet been shown.

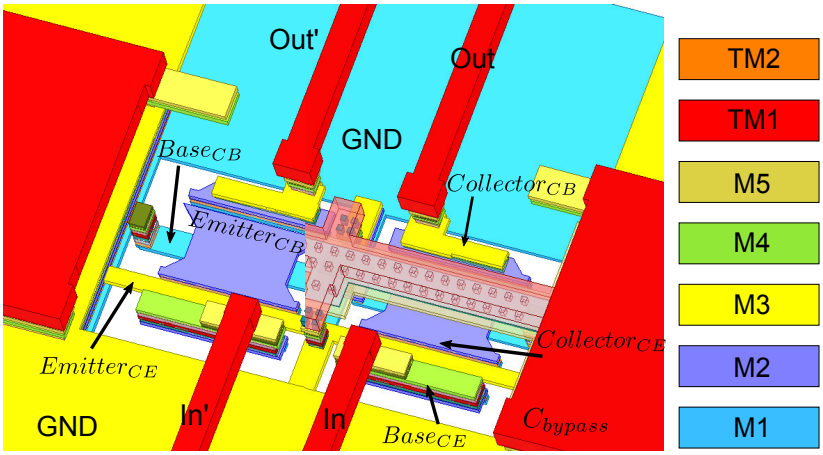

Figure 3.22: Full cascode layout. Each cascode pair represents a unit cell of the 3-stage amplifier excluding the impedance matching networks. Ground planes are positioned on all sides of each device, with additional bypass capacitors on the sides and the top of the base of the common-base transistors. The bypass capacitor is removed on the left side of the layout for visibility. ©IEEE [own1]

The ideal cascode including transistors with an emitter area of $6\times 0.96\times 0.12\,\mu m^2$ has an input impedance of 17.6 Ω-11.5j Ω and output impedance of 12 Ω-78j Ω at 270 GHz (see Fig. 3.23). The broadband impedance matching of the output node is particularly challenging due to the high impedance transformation required in the presence of the cascode output node's high Q-factor. Therefore, the implementation of the layout should aim to minimize the introduced parasitics. This will increase the challenge, but it will also allow access to matching networks implemented on higher metal layers, leading to minimized changes in S_{11} and S_{22} (Fig. 3.23). The equivalent output resistance and capacitance of the cascode is modeled as parallel R and C is 500 Ω/7.35 fF. Therefore, the interconnects between devices are optimized for minimum input and output impedance modification, both vertically and horizontally.

In [own1], the input, output, and interconnect modeling is described in detail which allowed to minimize the impact of the layout realization. It should be noted, that the inductor at the base of the CB transistor is sometimes used for additional gain boosting [9], [70]. In the presented power amplifier, this gain boosting was not actively used, however as seen from the resulting G_{max} curves in [own1], this cannot be avoided entirely.

Furthermore, interstage matching in between the CE and CB stage e.g. in the form of inductors is not feasible. As shown in [own1], the implemented transmission line between the two stages has a low characteristic impedance due to its width required to avoid electromigration, while a shift to higher metal layers would require additional vias which's losses negate the possible improvements of a series inductor. Therefore,

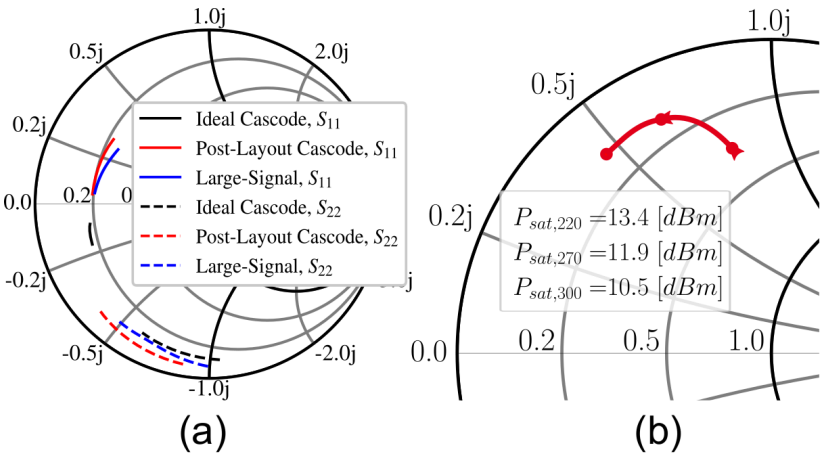

Figure 3.23: (a) The resulting input S_{11} and output S_{22} of the cascode for an ideal cascode, implemented optimized layout and under large-signal excitation between 200 and 350 GHz. The respective termination impedances for the matching networks can be derived from the provided smith chart projection. A reference resistance of 100 Ohms is used. (b) The optimal load impedances for achieving maximum output power of a single cascode including the layout in a range of 220 to 300 GHz. ©IEEE [own1]

this connection was kept on a low metal layer and its distance was minimized to thereby minimize the added capacitive loading of this node.

The resulting input and output impedance of the cascode including the layout can be derived from the S-Parameters shown in Fig. 3.23. The ideal output impedance of 12 Ω-70 jΩ at 270 GHz is decreased by the layout parasitics to 6.5 Ω-58 jΩ, which again increases for large-signal operation to 9.5 Ω-58 jΩ. For matching purposes, the transistor output capacitance is sometimes tuned out by parallel transmission lines/inductors. Thereby, a purely resistive output impedance can be generated. However, with the design frequencies approaching 300 GHz, the required length of such a compensating transmission line drops below 20 µm.Furthermore, the compensation is usually narrowband, which poses an additional challenge for matching interstage and output impedances in broadband applications.

For high-frequency circuits, transformers are often used for impedance matching. Especially for differential circuits, they enable common mode rejection and improved group delay flatness to impedance matching based on transmission line stubs. For narrowband matching and balun design, such baluns are often modeled using transmission lines [71], [72]. In the presented power amplifier, impedance matching transformers are used to provide a broadband match and allow for high output power generation.

Asymmetric broadside coupled-line transformers offer a solution for broadband impedance matching with high impedance transformation ratios, particularly for the final transformation to the external 100 Ω load. In the following, these asymmetric broadside-coupled line sections are introduced and presented in detail to generate broadband impedance matching networks at the input, output, and between each of the three stages.

3.4.1 Transformer-based Matching Networks

Coupled transmission lines can effectively transform the impedance between two network nodes when classical transformers operating below their self-resonance frequency (SRF) are inaccessible at around 300 GHz. For purely real termination/source impedances, the required line sections are typically around a quarter-wavelength. The operation bandwidth of such a transforming section can be further traded against the tolerable in-band mismatch and group delay distortion. In the simplest case, symmetric line arrangements can be exploited with regular even/odd mode analysis as introduced in Chapter 2. For the presented power amplifier, the required impedance transformation ratios are given by the input and output impedance of the layouted cascode. In case of the input matching, the impedance transformation ratio is 5:1 which in a conventional quarter-wavelength transformer would require a characteristic impedance of about 44 Ω which is equal to wide transmission lines.

In a 7-layer BEOL stack, broadside coupling between lines can be used to overcome the limitations of symmetric lines. This provides additional design flexibility due to the variable vertical line spacing (see Fig. 3.22). In this case, a simple even/odd symmetry plane referring to a global ground (see Chapter 2) cannot be applied. For this, A valid general modal analysis for an asymmetric couple-line system in inhomogeneous media should be used [37], [73], [74]. The mathematical formulation of such generalized asymmetric coupled-line transformer can be found in [own1].

All coupled-line distributed transformers implemented in this work utilize the 7-layer back-end-of-line (BEOL) stack to achieve a wide range of impedance transformation ratios. The transformers mainly utilize the 4-layer buried stack that is enclosed between TM1 and M3.. Thereby an improved matching between phase velocities of the $'c'$ and $'\pi'$ modes is achieved. Wherever possible, the bottom strip is chosen to be wider than TM1 due to its lower thickness, in order to achieve the required characteristic impedances. To improve line coupling, the bottom ground is removed, and the line sections refer only to the side ground, which is located in close proximity to make the layout compact. The presence of the side ground is fully included in the modal analysis of the coupled-line sections. Imperfect isolation of the coupled strips from the

surrounding global ground is commonly considered a performance degradation factor and is therefore often omitted in the design process. The ground plane adjacent to the transformer layout usually extends across the entire TM2–M1 metal stack to protect it from nearby components.

All buried coupled-line sections are operated near the critical point [74] where the capacitively and inductively defined line coupling factors, $'k_c'$ and $'k_l'$, are nearly equal, resulting in in-phase voltage ratios, R_c and R_π. According to $Z_{c,t}/Z_{c,b}{=}Z_{\pi,t}/Z_{\pi,b}{=}{-}R_cR_\pi$, it implies that some modal impedances may become negative. This statement is not a contradiction, but it contrasts with the more common even/odd analysis, where the voltage ratios are in-phase (see Chapter 2). The negative $-R_cR_\pi$ product indicates that the normal modes cannot be excited separately by any combination of voltage sources and terminating impedances, thus creating a co-existance of both modes effectively in the coupled-line section [75].

As described in [own1], the transformers can be divided into three subcategories given their placement inside the circuit (input, interstage and output). The input transformer is used to transform the differential 100 Ω impedance equal to the system impedance to the input impedance of the first cascode stage. As shown in Figure 3.23, the input impedance of the cascode is mostly resistive, therefore the capacitance is ignored in the transformer design process.

The corresponding 3-D simulation model of the optimized transformer layout is presented in Fig. 3.24 displaying all major dimensional parameters. The complete layout is subdivided into three line subsections, named from $'1'$ to $'3'$. Each subsection implementation applies a slightly different transformation ratio to optimize operation bandwidth in the presence of multiple reactive discontinuities resulting from the entire wiring system. Figure 3.25 shows a simplified equivalent circuit model that corresponds to half of the layout.

The simulated S-Parameters of the input transformer is shown in Fig. 3.26. For the other transformers, the analysis and simulation results of the individual transformers was already presented in [own1].

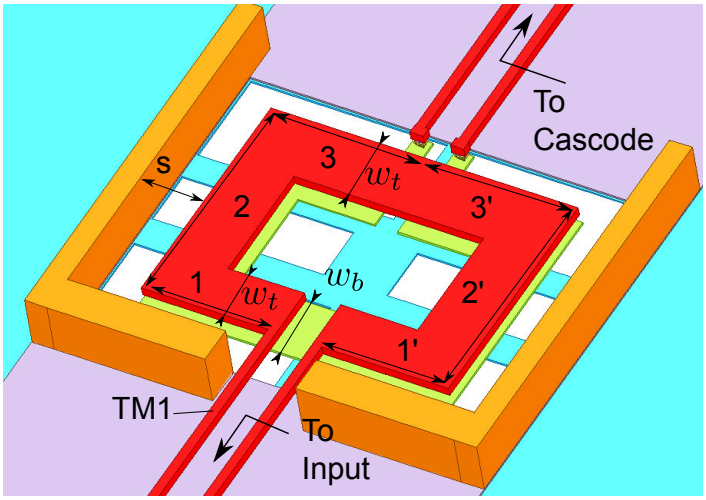

Figure 3.24: Full 3-D simulation model of the PA input transformer. Three main coupled-line sections, numbered from ′1′ to ′3′, with the corresponding widths for the top (w_t) and bottom (w_b) strips, as well as the spacing, s, to the side ground plane are indicated. The transformer covers a size of $80{\times}100\,\mu m^2$. ©IEEE [own1]

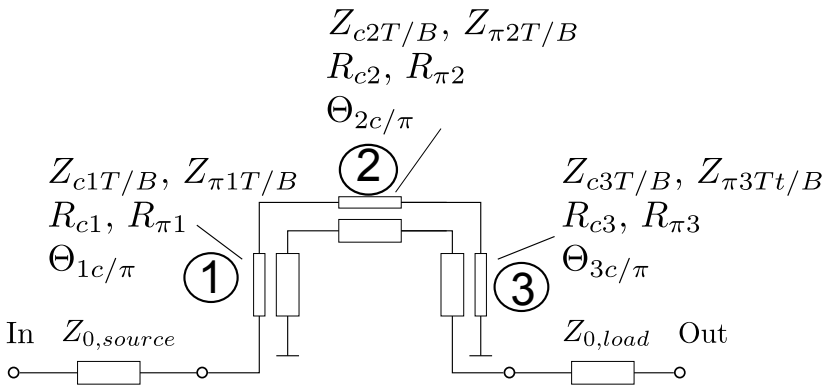

Figure 3.25: A simplified coupled-line model of the transformer is used to describe the PA input port, assuming an odd symmetry for the differential excitation scheme ©IEEE [own1]

The presented input transfomer displays a broadband input match from 230 to 325 GHz. Again, it should be noted that the input transformer transformers a real 100 Ω impedance to the real input resistance of the cascode base. The influence of the base-emitter capacitance can be ignored for this matching as the Q-Factor of the input is very low.

In the following, the measured results of the power amplifier are briefly discussed to later on compare the amplifier's performance with the measured performance of the frequency multiplication breakout and later on the full RF characterization of the TX and RX.

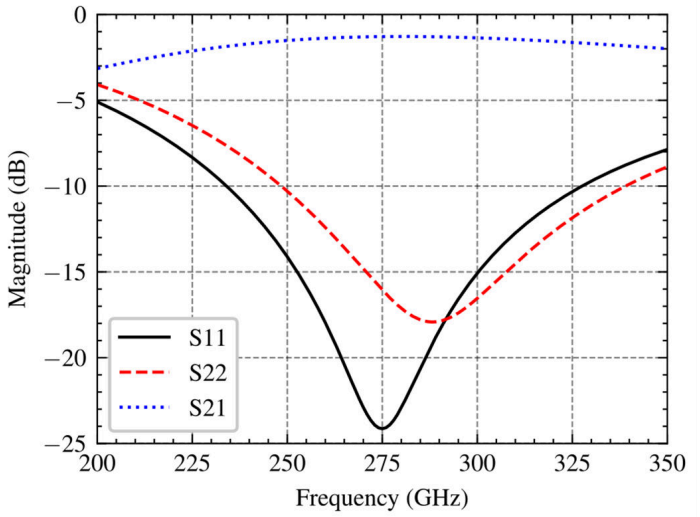

Figure 3.26: Simulated S-Parameters of the input transformer. Input match of the amplifier is hidden by the input match of the broadband balun in the following measurement.

3.4.2 Power Amplifier Measurement

The amplifier underwent characterization for both small-signal and large-signal operation. Frequency extenders were used in combination with a VNA for S-Parameter measurements (Fig. 3.27) and high power sources and a PM4 Power meter for large-signal measurements.

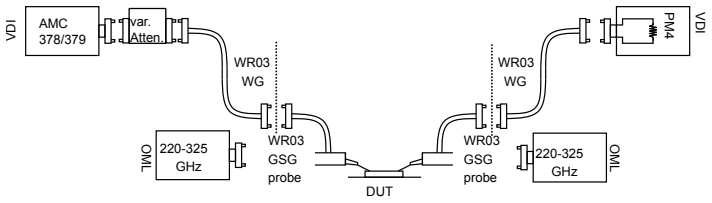

Figure 3.27: Measurement setup for both small-signal and large-signal measurements. The small-signal calibration was done using TRL standards. The small-signal calibration was performed using TRL standards, while for large-signal measurements, a two-tier calibration was conducted, which included the subtraction of the waveguide losses. ©IEEE [own1]

The presented amplifier exhibts a a maximum S_{21} of 20.1 dB at 254 GHz with a 3-dB bandwidth of 63 GHz, spanning from 239 GHz to 302 GHz for a supply voltage of 3 V (Fig. 3.28).

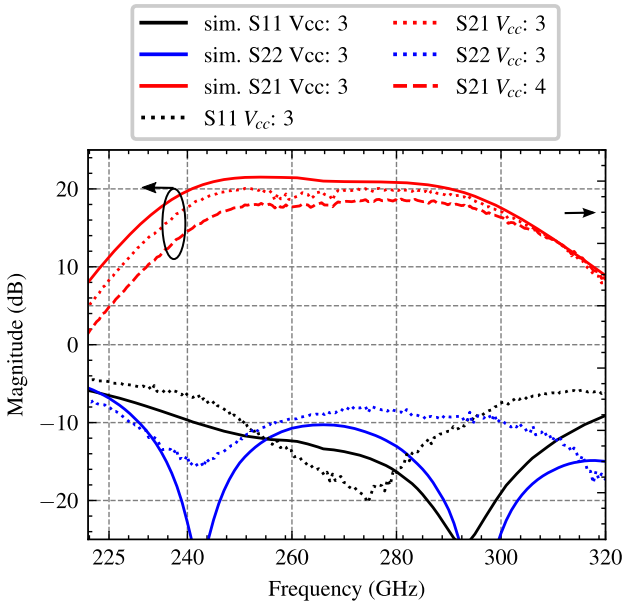

Figure 3.28: Measured and simulated small-signal S-parameters of the presented PA including the balun and pad. The resulting S_{21} for different supply voltages is shown as well. For 3 V supply voltage, the amplifier shows the highest gain and bandwidth. The measured k-factor is omitted from this plot.

Changing the supply voltages in either direction reduces the small-signal gain because the cascode biasing depends on the supply voltages (see Fig. 3.21) and thus changes the voltage headroom of the CE transistors. This effect is later on used to determine the input power levels at the power amplifier in the full system. In full compression, the reduced gain should not be visible as the output power should also be compressed.

As the amplifier is also used in the RF path of the transmitter, its effect on the group delay in modulated signals needs to be measured to derive potential inter-symbol interference limitations As shown in Fig. 3.29, the measured group delay stays within ± 4 ps in the entire frequency band, which is equal to ± 10% of the symbol duration time in a 100 GB/s 16-QAM modulation data stream. This measurement furthermore shows a very high correlation to the simulation.

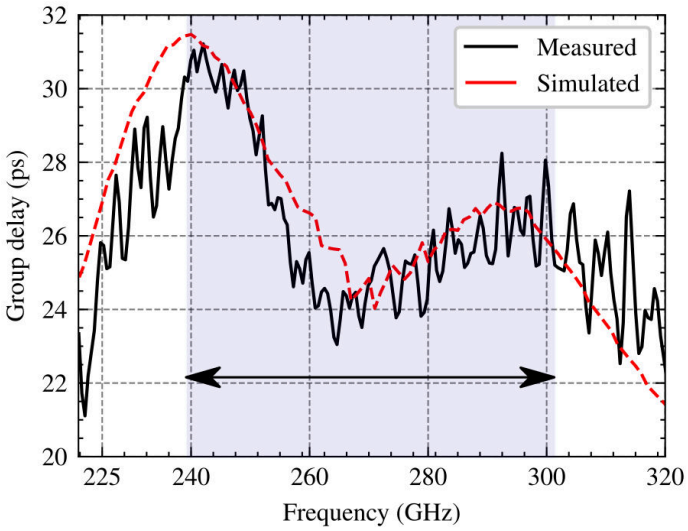

Figure 3.29: Measured group delay of the amplifier. Over the small-signal bandwidth (239-302 GHz), the group delay stays within ± 4 ps. Similar values were measured for varying supply voltages. ©IEEE [own1]

For large-signal measurements, the input power was adjusted with a pre-calibrated mechanical attenuator (see Fig. 3.27). The measurement was adjusted to account for the loss of the probes and additional s-bend waveguides.

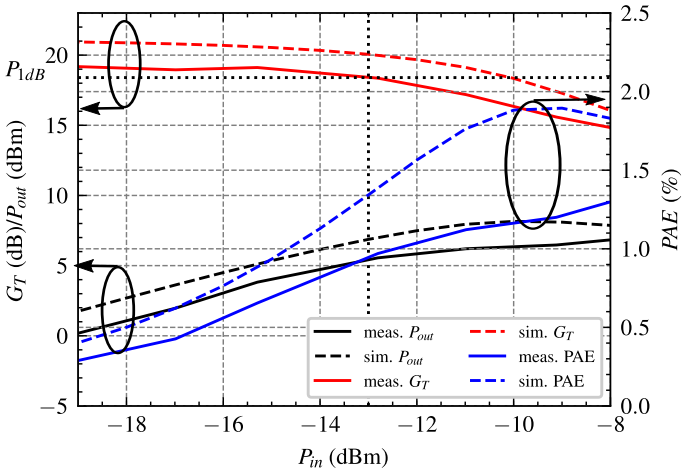

Figure 3.30: P_{out} vs. P_{in}, large-signal gain and power added efficiency(PAE) for a supply voltage of 3 V at 270 GHz. Both the output referred compression point and PAE remain almost constant for varying frequency. The losses of the balun and pad have not been de-embedded in this figure. ©IEEE [own1]

The measured output power (P_{out}), large-signal transducer gain (G_T), and power added efficiency (PAE) at 270 GHz is shown in Fig. 3.30. G_T aligns with the measured small-signal gain (Fig. 3.28), while an output referred P_{1dB} compression point of 5 dBm and a maximum saturated output power of 7 dBm at 270 GHz with a PAE of 1.3% was measured. Over frequency, these performance metrics are also shown in

Fig. 3.31 with a maximum OP_{1dB} of 5.2 dBm and maximum PAE of 1.38% at 260 GHz.

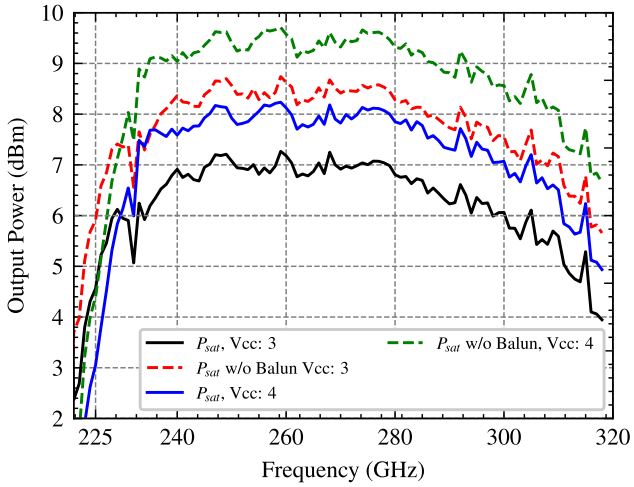

Figure 3.31: Saturated output power of the amplifier in the entire frequency band with and without balun losses. At 259 GHz, a peak P_{sat} of 7.3 dBm with a saturated output power 3-dB bandwidth 94 GHz (223 GHz–317 GHz) for a supply voltage of 3 V is measured. By increasing the supply voltage to 4 V, this output power was increased to 8.2 dBm. With Pad and Balun losses de-embedded, a peak output power of 9.7 dBm is obtained.

For saturated output power, the bandwidth is extended from 63 GHz to 94 GHz (223-317 GHz). The amplifier's maximum output power of 7.3 dBm is reached at 259 GHz. The amplifier consumes about 360 mW for a supply voltage of 3 V and a current density of 27.49 µA/mm^2 close to the f_t/f_{max} current density (26 µA/mm^2). By de-embedding the losses of the broadband balun, the power delivered to an external 100 Ω load is estimated as shown in Fig. 3.31, the de-embedded small-signal S_{21} is 23 dB at its peak. A maximum de-embedded output power of 8.7 dBm/9.7 dBm for 3 V and 4 V supply voltage, respectively, is achieved at 259 GHz.

The here presented power amplifier allows do cover most of the frequency band planned for the IEEE 802.15.3d-2017 standard [4]. In the presented transmitter and receiver, the power amplifier is used in the LO generation path. In the transmitter, the power amplifier is further used for amplification of the upconverted double sideband signal. For the LO generation, the amplifier linearity is not of interest, therefore the large-signal bandwidth extension could be used for carrier frequency allocation between 223 and 317 GHz provided that the LO frequency generation stages generate enough input power for the power amplifier. The shown linearity and group delay are of interest for the RF path where modulated signals will be applied to the input of the amplifier. It should also be noted that the amplifier is optimized for broadband power generation, while the gain-bandwidth could further be improved as shown in [32].

3.5 Frequency Generation

As previously described, both transmitter and receiver use identical circuits for LO generation. For LO generation, two different approaches can be found; Either based on integrated oscillators or externally provided LO reference signals. While the integration of oscillators on the same chip allows for an additional degree of indepenc, integrated oscillators have a reduced tuning range in comparison to externally provided reference signals.

However, at the same time the required LO frequency can often not be generated externally and then brought into the chip as a LO signal at around 300 GHz would require extremly complex packaging which is deemed impossible at this point in time. Therefore, the externally provided LO reference signal is typically fed into frequency multiplication stages to derive an LO frequency at a multiple of the reference signal. Through this approach, a high tuning range that is ultimately limited by the input and output matching of the frequency multiplication stages is achieved.

For broadband communication systems, it was shown that the multiplication factor and with it the initial LO reference frequency can become a limiting factor when the LO reference frequency falls into the used modulated bandwidth [60]. In addition, frequency multiplication does not only produce the desired output frequency but also additional unwanted harmonics which will also interact with up- and downconversion mixers and create modulated images at multiples of the LO reference frequency. Therefore, ideally the initial LO reference frequency should be as high as possible - with respect to packaging capabilites and the frequency multiplication factor should be kept as low as possible.

The typical generated multiplication factors are 2 and 3 and combinations of these. Frequency multiplication can be achieved either by mixer-based upconversion stages [76]–[78] or inherent device non-linearity[79]–[82]. For the latter, depending on the multiplication factor, a suitable combination of the transistor current conduction angle and its compression characteristics is commonly applied to optimize the harmonic of interest. For the former, the probably most representative example is an active Gilbert-cell which forms a doubler circuit while driving both inputs with the same frequency tone, ideally in quadrature[own5]. Its popularity at lower frequencies comes from the achievable conversion gain and inherent differential operation both at the input and output ports [61], [83]. However, its advantages disappear towards 300 GHz output frequencies for silicon technologies due to device frequency limitations and layout complexity. In particular, difficulties in controlling the appropriate phase relations between the relevant nodes may lead to a more complex output frequency spectrum and frequency/amplitude-dependent DC offsets.

Opposed to that, the use of an appropriately biased differential amplification stage (e.g. differential pair) with a combined or differential output can be equivalently applied for extraction of the higher-order even- or odd-mode harmonics with an additional advantage of the lower DC power consumption and layout simplicity. However, the major disadvantages become: 1) the leakage of a fundamental tone for odd-harmonic generators and 2) the missing balanced output for even-harmonic generators.

Independent from the topology of choice, the high-frequency device limitations with the related maximum device size lead to a very fast performance deterioration of multiplication stages while approaching the device cut-off frequencies. In particular, for low device biasing points typically required for harmonic current generation [80], they suffer from the missing current density for the rated device f_t/f_{max} density and from the low effective large-signal power gain. It eventually results in limited voltage/current swings, poor conversion efficiency, and considerably higher sensitivity to the input drive power level in comparison to the low-frequency implementations. On top of that, the termination impedances maximizing the harmonic power levels become predominantly reactive with impractically low real parts. All of this constrains the achievable operating bandwidth even though a multiplication factor predicts N-times increase of the input frequency bandwidth. Another set of challenges related to a wide frequency range of operation needs to cope with the spectral purity due to the potential frequency overlap among harmonics and the layout modeling complexity due to its frequency-increasing electrical size in terms of wavelength.

To address the carrier frequencies of the IEEE standard [4], the ideal multiplication factor when driven from an external signal generator should be equal or greater than 9. A multiplication factor of 10 would rely on the 5th harmonic generated by a device, which already shows decreased transconductance in comparison to the fundamental and third harmonic (compare Taylor-Expansion).

To generate a multiplication factor of 9, two frequency triplers are cascaded as shown in Fig. 3.32. As described above, odd harmonic-generators' disadvantage is their LO leakage. For this, bandpass filters are placed at the output of each tripler [84]. At the same time, the differential topology of the harmonic generator naturally suppresses even-harmonics as they only propagate in the common-mode given an ideal differential excitation. This undesired common-mode harmonics are further attenuated by the bandpass filters which include common-mode bandstop structures [84].

The triplers use cascodes for their increased voltage swing and isolation while the third harmonic is generated by the compression of the cascode. This operation mode is termed overdrive as the third harmonic is generated by the 'clipping' of the output voltage swing. Therefore, it can also be derived that this operation mode relies on

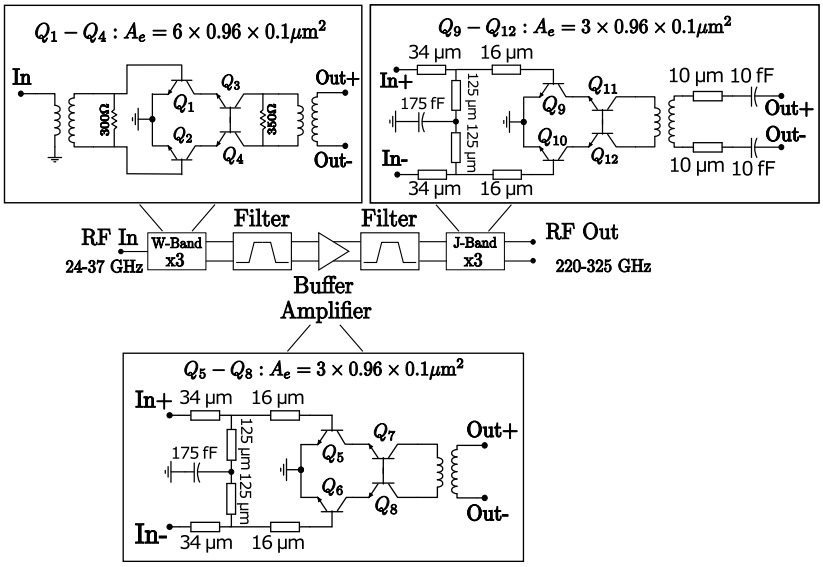

Figure 3.32: Block diagram of the implemented x9 frequency multiplier including the two filters used for harmonic suppression as well as the buffer amplifier at the intermediate frequency.

high input power levels. To achieve this for the second tripler with its input frequenc centered around 100 GHz, an additional buffer amplifier is positioned before the final tripler.

The x9 frequency multiplication stages were measured in a separate breakout including the power amplifier [own1] for increased output power. The measurement and simulation results can be seen in Fig. 3.33. From the results, the 3-dB bandwidth of the implemented frequency multiplication stages can be seen spanning from 239 GHz to 304.2 GHz, which is almost identical to the 3-dB bandwidth of the used power amplifier (comp. Fig. 3.28) At the same time, the effect of the implemented bandpass filters can be seen resulting in a harmonic suppresion of the undesired harmonics at the center of the band. Given the high total bandwidth of both the frequency multiplication stages and the following power amplifier, the undesired harmonics are amplified by the power amplifier at the edges of the observed frequency band where they fall into the amplification bandwidth. Here, the frequency multiplier stages achieve a harmonic suppression >30 dB from 243 GHz to 300 GHz.

Overall, it can be seen that ×9 frequency multiplication is feasible and - in combination with the power amplifier - generates output powers >0 dBm, sufficient to drive the up- and downconversion mixers in the implemented transmitter and receiver.

For communication, the phase noise of the LO frequency is of high importance as it creates an additional source for EVM detoriation (Chapter 2). The relatively low frequency multiplication factor has the advantage of decreased added phase noise.

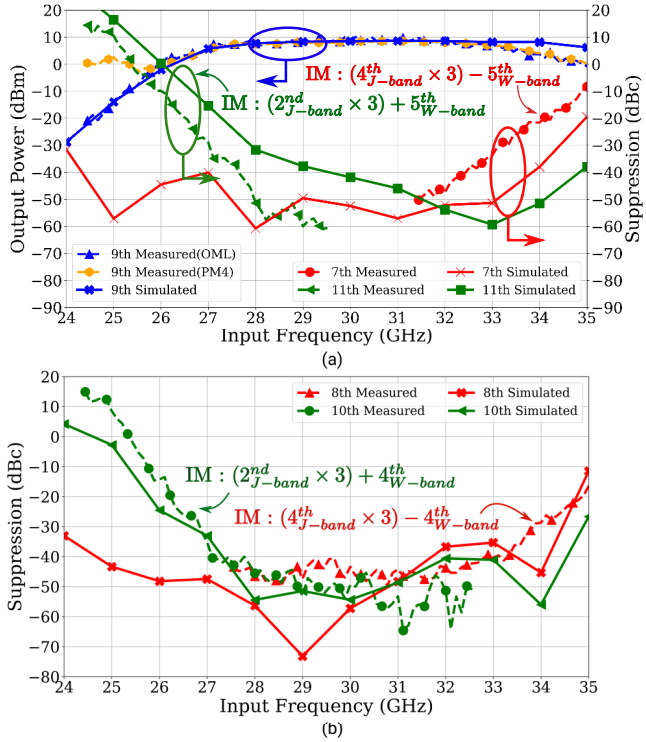

Figure 3.33: Measurement and simulation results of the frequency multiplier including the power amplifier. In the implemented communication transmitter and receiver, the output power of the frequency multiplier is divided by a Gysel-Power divider before further amplification with the respective power amplifiers. Thereby, the resulting output power is not identical to the LO drive power in the systems.©IEEE [own6]

In general, the added phase noise by frequency multiplication can be calculated by:

$$20 * log_{10}(N) \tag{3.1}$$

with N being the frequency multiplication factor. The here used x9 frequency multiplication stages add 19.1 dB to the generator's initial phase noise, which is 5 dB less than a x16 frequency multiplication stage [56].

In communication systems, the LO of the transmitter and receiver are ideally locked to each other to ensure optimum communication conditions and reduced phase noise.[85]. While inside a lab, the LO, the transmitter and receiver can be referenced to the same signal generator, this operation is not truly wireless. In communication systems including on-chip oscillators, frequency and phase locking between transmitter and receiver is typically achieved using phase locked loops (PLLs). At carrier frequencies around 300 GHz, implementations of such PLLs are rare [86] and show a limited locking range [87]. Other approaches such as costas loops for carrier recovery [88] are limited by the

usable modulation schemes and have so far only been shown for BPSK and QPSK at comparable operating frequencies.

To achieve LO phase alignment in the measurements shown in Chapter 6, signal generators with internal phase shifters are used with the transmitter and receiver driven from two individual outputs of this signal generator. The used phase shifter in combination with the LO frequency multiplication causes a limited phase resolution as the frequency multiplication factor is also applied to the phase.

Another potential approach for phase alignment is the implementation of integrated phase shifters in the LO generation path. Here, a phas eshifter implementation at the LO frequency would ensure the highest possible phase resolution. In the following, an integrated phase shifter operating up to 270 GHz is discussed, highlighting the potential for future phase locking.

3.5.1 Phase shifter

Phase shifting can be achieved by various methods such as delay line switching, reflection type, and vector magnitude addition. With increasing operating frequency, delay line switching becomes less and less attractive due to the increased losses and limited phase resolution. Contrary to this, active vector magnitude addition offers an alternative with decreased insertion loss due to the intrinsic device gain and full 360° phase resolution.

One popular implementation of such a vector magnitude addition based phase shifter is based on Gilbert cells as shown in Fig. 3.34. First, the 90° hybrid creates two orthogonal paths, which are then fed into a switching quad. By adjusting the base-emitter voltage of the individual transistors in the switching quad, the gain or in this case the vector magnitude is adjusted. The switching quad output is then first current-combined into a differential output which is then fed into a balun for differential to single-ended combination. One major disadvantage of this topology is the lack of a purely differential output. The non-ideal vector addition as shown in [89], leads to a mixed signal excitation i.e. both differential and common-mode signals are generated. However, for phase shifting only the differential sum of the applied vectors is of interest. For this, the balun should have high common-mode rejection to reject the unwanted signal propagation.

The implemented phase shifter can be seen in Fig. 3.35. Instead of the previously used SG13G3, the phase shifter uses a comparable experimental 90 nm SiGe BiC-

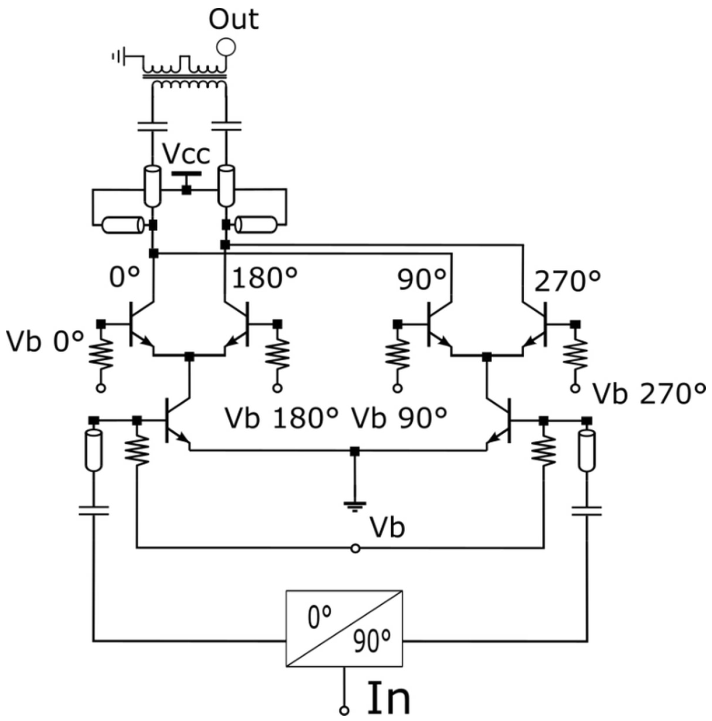

Figure 3.34: Schematic of the phase shifter. The general design is derived from a Gilbert Cell where the biasing of the switching quad is adjusted to change the gain and thereby the weighting of each path.

MOS technology (B12HFC) by Infineon with a f_t/f_{max} of 300/540 GHz respectively. The implemented phase shifter requires single-ended I and Q signals, for this a single-ended miniaturized 90° branchline hybrid was designed [90]. It uses the BEOL as the minituarization is achieved by additional MIM capacitors. The single-ended I and Q signals are then fed into the transconductance stage. The individual base biasing of the switching quad is achieved using 4k Ω resistors with additional DC bypass capacitors. For output matching, series transmission lines in combination with MIM capacitors are used while the collector biasing is provided by shunt transmission lines creating a common-mode node.

In normal operation, only two transistors of the switching quad conduct simultaneously, so the output impedance of the switching quad is assumed to be constant in the matching design process. Unlike regular Gilbert cells, the vector magnitude addition operation is not based on switching, but on the combination of the conducting transistors in the switching quad.

In the presented phase shifter, the phase shift is generated by the addition of individually weighted vectors. The weighting of these vectors depends on the biasing adjustment of the transistor in the respective vector's path. To achieve perfect phase coverage, the total sum of the vectors should remain constant, indicating constant amplitude.

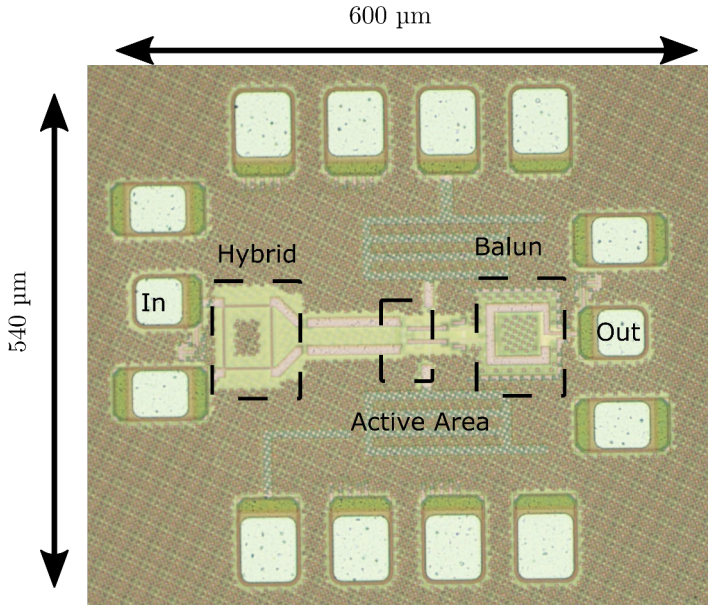

Figure 3.35: Chip micrograph of the phase shifter. The total size is 0.32 mm^2, the size is set by the required pads and their pitch of 100 μm.

The output matching of the phase shifter was performed assuming that only 50% of the switching quad transistors are turned on at any given time. The use of a single Gilbert-cell approach reduces the output current combining ratio. However, increasing the transistor size results in a high quality factor that limits the bandwidth. To achieve the final signal combining, a broadband coupled-line based balun with additional common-mode suppression is used. This is necessary for this application as the vector sum generation creates both a differential and common signal.

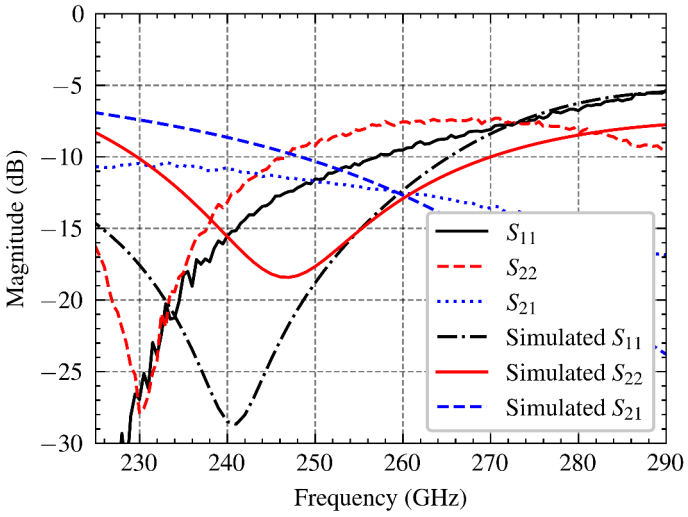

Figure 3.36: S-parameter measurement results of the phase shifter. Both input and output display a broadband match.

As shown in Fig. 3.36, both the input 90° Hybrid and the output balun achieve a broadband match with a return loss (S_{11} & S_{22}) below 10 dB spanning up to 255 and 245 GHz respectively. The insertion loss exhibits a 3 dB-Bandwidth spanning from 225 GHz to 270 GHz. Here, the lower end cannot be measured as it is outside the observable frequency range.

For the phase shifting operation, the constellation diagram (Fig. 3.37) shows that over the entire range different phase angles can be adressed. In the measurement, the biasing was varied with constant voltage steps of 10 mV. As the gain is not a linear function of the base-emitter voltage, the change in phase is not linear. By referring to the base current, the gain variations are in a linear relation due to the variation of g_m, thereby a equally spaced phase change can be achieved with respect to the base current. The phase shifter consumes 24 mW from a supply voltage of 2.6V with a total size of 0.32 mm², which is set by the required signal and biasing pads as shown in Fig. 3.35.

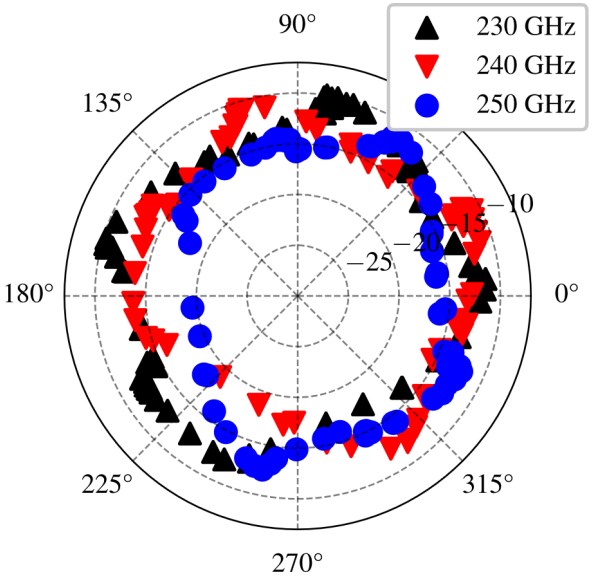

Figure 3.37: Phase shifter constellation measurement results at 230, 240 and 250 GHz. For different frequencies, the initial offset in phase is visible.

For LO phase alignment, the group delay variations caused by the phase shifter are not of interest. However, the phase shifter can also be used for beam steering when used in a transmit/receive array. Again, here for LO phase shifting, the group delay variations can be neglected, while the gain variations are removed by e.g. a limiting amplifier.

However, if the phase shifter is used in the RF path, the group delay should be constant as shown in Fig. 3.38. Therefore, the implemented phase shifter can be used for both LO and RF phase shifting. The implementation does not cover the entire

bandwidth of the previously shown frequency multiplication stages. The matching is centered around a lower frequency and would have to be increased. Based on the measurement results, a design at higher frequencies is feasible as it potentially has lower losses than [89] and can be combined with a high gain amplifier similar to [32].

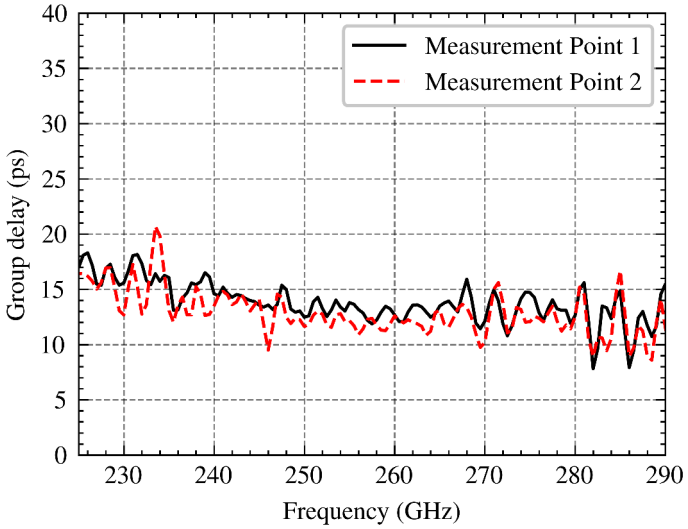

Figure 3.38: Phase shifter group delay measurement results. For different output phases, the group delay variation remains below 20 ps.

3.6 Summary and Conclusion

In this Chapter, the individual building blocks for the Dual Polarized 300 GHz Transmitter and Receiver were introduced. Moving along the block diagram (Fig. 3.3 & 3.1), first the antenna is presented before the individual up- and downconversion mixers are shown. The 300 GHz power amplifier and the frequency multiplication stage are used in both transmitter and receiver.

While the upconversion path shows no intrinsic bandwidth limitation, the baseband routing of the downconversion stage limits the total receiver bandwidth to 17 GHz which is half the required bandwidth for the largest channel in the IEEE standard[91]. Furthermore, the differing baseband routing for the I and Q mixers intrinsically creates an I/Q imbalance in both amplitude and phase, which cannot be equalized in the demodulator. In addition, it was shown that the implemented TIA is sensitive to the applied LO power at the downconversion mixer. Since the LO power cannot be linearily controlled as it is generated by the later described frequency multiplier stages, this limited power handling can lead to a further reduction of the usable bandwidth.

This bandwidth limitation was found after the integration into the receiver. In this Chapter, an improved transconductance amplifier is shown which covers the required bandwidth, offers LO power handling and improves the I and Q amplitude and phase imbalance. Due to the high turnaround time for tapeouts in the used experimental technology, no improved receiver was implemented.

In both the transmitter and receiver, a 300 GHz power amplifier is used to first provide the necessary LO power for upconversion and downconversion. For the transmitter, the same power amplifier is used to further amplify the upconverted DSB signal before it is transmitted through the antenna.
Compared to previous communication standards, the maximum RF bandwidth of 69 GHz defined in [4] creates a challenge for power amplifier design at this frequencies. The state-of-the-art showed that silicon-based power amplifiers did not exist in this frequency range which was clearly limited by the available silicon technologies. By using a advanced 0.13 µm SiGe BiCMOS technology, the operating frequency of the amplifier was increased. Similarly, the used technology exhibts large gain margin, therefore no additional - bandwidth limiting - gain boosting was applied in the amplifier design. To achieve broadband matching at the different stages of the power amplifier, the power amplifier uses novel asymmetric coupled-line transformers that allowed to achieve the required impedance ratios while maintaining a high bandwidth, low gain ripples and low group delay variations.
The bandwidth improvement is partially attributed to the multi-section design of the transformers which in comparison to the more common frequency-staggering does not lead to discontinuities in the phase behavior of the amplifier.

The presented amplifier has a 3-dB bandwidth spanning from 239 GHz to 302 GHz (63 GHz) with a peak gain of 23 dB, which is again lower than the desired bandwidth. Similarly, it was visible that the gain decreases faster above 280 GHz which is contributed to the transistor modeling in the early state of the technology development. The measured and simulated results show a high correlation at the lower end of the frequency range hinting for succesful device and passive modeling.

The amplifier reaches a maximum output power of 9.7 dBm which is close to the projected maximum output power of silicon technologies in this frequency range [5]. Ideally, the shown bandwidth and output power is available for the TX and RX, which is characterized in Chapter 5.

This dissertation presents a ×9 frequency multiplier chain based on two differential cascode triplers. The multiplication factor was chosen to not only increase the spacing between the generated harmonics, but also to minimize the contributions of

the frequency multiplication on the total LO phase noise. The cascode triplers were used to ensure that only odd harmonics will propagate along the differential routing, while the even harmonics are ideally confined in the common mode. In addition to this, novel bandpass filters were used at the output of the two triplers respectively to further suppress the generated undesired harmonics of the frequency multiplication.

The filters allowed to suppress the neighbouring undesired harmonics by 40 dB starting from 243 up to 305 GHz. This bandwidth overlaps with the bandwidth of the power amplifier that was used in the on-wafer measurement, therefore it can not excluded that the power amplifier limits the total bandwidth of the frequency multiplier stages.

In the implemented transmitter and receiver, the generated LO signal is split using a Gysel power combiner (Fig. 3.10) at the output of the last tripler. In this chapter, it was shown that the Gysel power amplifier adds additional loss which is ideally recovered by the following individual power amplifiers in each polarization. With further splitting for I and Q generation using the differential coupled-line 90° Hybrid (Fig. 3.6), the following RF characterization of the TX and RX will show if the LO power at the up- and downconversion mixer is sufficiently high for mixing in the desired frequency band.

Based on the individual performance of the broadband building blocks presented in this Chapter, it is expected that both TX and RX can be succesfully implemented. As shown by the bandwidth of the frequency multiplier stages and power amplifier, the LO frequency allocation will be limited to frequencies up to 305 GHz. Furthermore, DSB transmission at this 300 GHz is expected to be unsuccessful, as the used power amplifier will only amplify one sideband creating artifical RF filtering and thereby SSB generation.

To characterize the TX and RX chipset, in the following Chapter 4, the design of the broadband, high-frequency PCB is discussed to allow interfacing of the integrated chips with test equipment. There, it will also be shown whether the bandwidth achieved by the integrated circuits can be maintained by the packaging.

Chapter 4

Packaging

This chapter describes packaging for communications systems with bandwidths exceeding 10 GHz. In contrast to narrowband communications systems or terahertz imaging systems such as [92], [93], broadband communications systems need a respective broadband packaging especially for the baseband channels.

The final 300 GHz communications system contains four fully differential baseband channels that must be connected to a PCB to provide access to external instrumentation such as e.g. spectrum analyzers, arbitrary wave generators, or oscilloscopes for baseband processing. At the same time, the systems require a large number of DC supply voltages that also must be provided from the outside. As described in Chapter 3, a lens-integrated antenna is used. For this, the entire TX and RX chip have to be placed at the center of the used silicon lens. The designed PCB include a recess at the center of the PCB to accomodate the entire chip. During the packaging process, the PCB is then glued to the silicon lens to ensure mechanical stability and to provide a path for thermal dissipation. A depiction of the final lens assembly can be seen in Fig. 4.1.

The baseband channels incorporate on-chip filter structures in form of a mimcap and inductor that is visible in the micrograph. Thereby, the baseband inputs are visibly distinguishable from the remaining DC supply input pads. In addition, the LO pad structure at the bottom in form of ground-signal-ground pads can be identified where the externally supplied LO signal is fed into the input balun of the frequency multiplier.

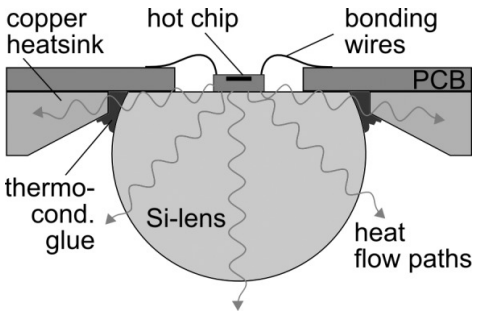

Figure 4.1: Depiction of the lens assembly. The chip is glued to the flat surface of the silicon lens which is then glued to the PCB. The chip is placed in a recess of the PCB and then wire bonded to the PCB traces.

As the individual I/Q mixers have a differential input, the differential signal must be provided accordingly to ensure signal purity. In contrast, the LO is single-ended and therefore does not require phase compensation to its reference, as described in Chapter 2.

4.1 PCB Design

Since external test equipment typically requires a 50Ω match, both the on-chip ports and the PCB interconnects must be matched accordingly for high bandwidth, low reflection, and signal purity. The pads shown in the micrograph of both TX and RX in Chapter 3 have a pitch of 100 µm. For geometric matching, the PCB transmission lines should have a width of 50 µm and a characteristic impedance of 50 Ω. The bond wire required to connect the PCB with the chip introduces an inductance of a few hundred pH depending on its length, this inductance should ideally be compensated by both on-chip filters and reactive components on the PCB to reduce its influence on the bandwidth.

The characteristic impedance of a microstrip is given as $\sqrt{\frac{L'}{C'}}$ in the ideal case of a lossless transmission line, with L' being the inductance per unit length and C' the capacitance per unit length. At the same time, the characteristic impedance of an actual microstrip implemented on any substrate can be calculated by the Hammerstad Equation [94]:

$$Z_{0,\text{microstrip}} = \frac{Z_0}{2\pi\sqrt{\varepsilon_{eff}}} \ln\left(8\frac{h}{w} + \frac{w}{4h}\right) \tag{4.1}$$

For a Rogers RO4350b substrate ($\varepsilon_r = 3.49$) and a thickness of 250 µm that is readily available for high-frequency applications, the necessary width for a Z_0 of 50 Ω is 700 µm. To reduce the line width, substrates with a higher ε_r can be used. FR-4 with a slightly higher ε_r cannot be used due to increased losses at higher frequencies

(dispersion) and the inaccuracy of its permittivity varying between 3.8 and 4.5. As an alternative Rogers RO3006 is selected with an ε_r of 6.15 and a loss tangent of 0.002 at 10 GHz, allowing to reduce the microstrip width down to 400 µm.

The Rogers RO 3006 laminate is a ceramic-filled PTFE in contrast to the more common RO 4350B which is a hydrocarbon ceramic laminates. While the simulations showed promising results, the first PCB prototypes proved to be too brittle and broke under minimal pressure during the assembly process. Therefore, the laminate needs to be combined with an additional FR-4 core for mechanical stability, making it a multilayer PCB.

In combination with the ground connections on the PCB, the minimum structure size is still too large as ideally still a microstrip width of 50 µm is required for geometric matching. For the single-ended LO input, the geometric feature size can be reduced by replacing the microstrip transmission line with a CPW. Thereby, the signal trace width can be reduced to 100 µm with a narrow gap of additional 100 µm and the ground traces of the CPW on its sides. The CPW also allows inclusion of stepped-impedance sections into the LO feed to compensate the signal bondwire and match to the input balun of the frequency multiplier. Furthermore, the added ground shielding along the sides of the signal path allows for additional isolation of the high-powered LO signal ($P_{LO} > 5\ dBm$) from the low-powered baseband signals.

While in a transmitter, the baseband and LO power levels are comparatively close to each other, in a receiver the downconverted baseband signal power is 20 dB lower than the LO and therefore can be masked by the LO signal propagating through the PCB. Especially, for broadband baseband channels this can become problematic if the LO frequency is inside the occupied baseband bandwidth. This effect creates an additional requirement for the development of RF frontends with sufficiently high LO frequencies.

For the differential I and Q baseband signals, coupled lines in a CPW configuration are used to minimize the width of each baseband channel. Coupled line sections were introduced in Chapter 2; due to its symmetrical topology, the characteristic impedance of the coupled line can be described through even/odd mode analysis, where the differential characteristic impedance ideally is 100 Ω.

The PCB design can be separated into 3 components:

- Bonding Area
- Coupled Line Decoupling
- Connector

These components will be discussed in the following.

4.1.1 Bonding Area

For both the LO input and the baseband input and output, the bonding area is crucial because the bond wire inductance must be compensated for the desired frequency response. As shown in Fig. 4.2, the baseband signal pads are directly bonded to coupled signal traces. Each signal trace has a width of 100 µm, which is the minimal width for regular PCB manufacturing processes. The ground walls on the side have a width of 400 µm, which is the minimum via diameter. In the implemented board, the ground walls are generated by evenly spaced vias along the ground traces. It should be noted, that the PCB manufacturing process does not allow for traces to be closer than 200 µm to the edges.

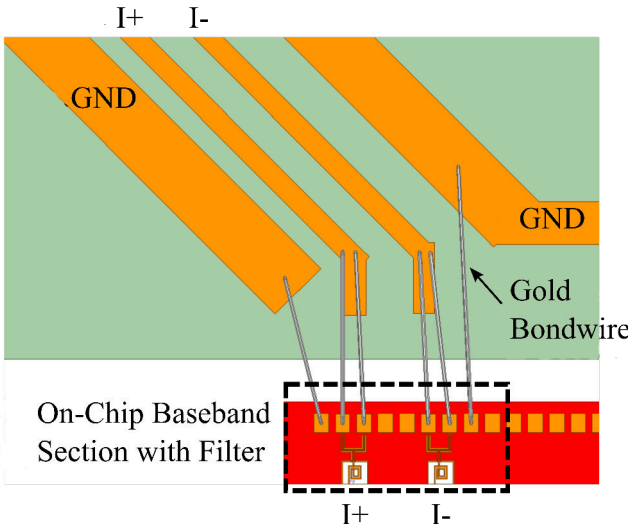

Figure 4.2: HFSS model of the differential baseband section. Each output has two identical signal pads which are bonded to the same trace. The ground pads are bonded as well. The center ground pads placed between the positive and negative signal pads are left unbonded as no center ground can be established.

The resulting return loss and insertion loss can be seen in Fig. 4.3 with the respective PCB Port placed along the coupled line on the PCB. The simulated S-Parameters show a broadband lowpass behavior with a return loss of at least -10 dB up to 33 GHz.

Similarly, the insertion loss shows a roll-off starting at 33 GHz. This low-pass behavior is mostly dominated by the on-chip implemented low-pass filter sections consisting of a small shunt capacitor implemented as a mimcap, the series inductor visible in Fig. 4.2, the pad capacitance and wirebond inductance. The use of two wirebonds per trace reduces the wirebond inductance. However, it is not possible to extend the lowpass behavior to higher frequencies.

In previous publications [6], [95], the wirebond compensation was done solely on chip resulting in a bandwidth of 14 GHz. By utilizing on-chip filter sections, the total bandwidth can be improved as shown in [96] while potentially reducing the filter order.

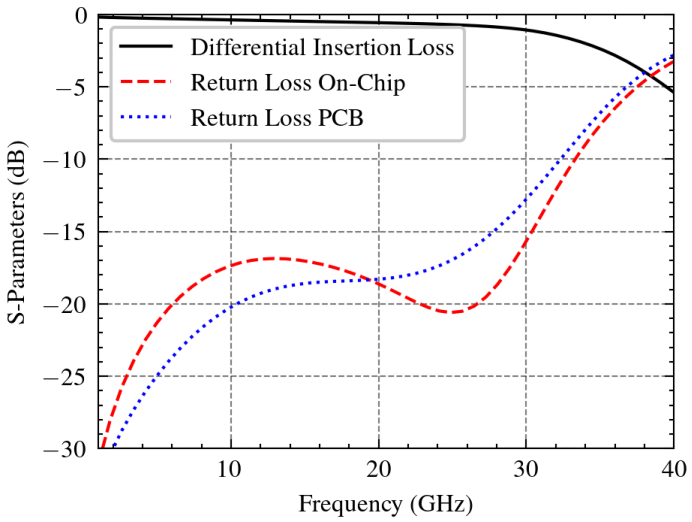

Figure 4.3: Insertion and return loss of the differential baseband bonding area shown in Fig. 4.2. The S-Parameters show a low-pass behavior up to 30 GHz.

In the implemented PCB, the diagonal traces are about 21 mm long to create the necessary fan-out for the connectors. The length of the line is the biggest contributor to the insertion loss, but it cannot be shortened, resulting in an unavoidable lossy section. The diagonal coupled line traces are then fed into the decoupling section.

4.1.2 Coupled Line Decoupling

As previously mentioned, the differential baseband signal pads are bonded to shielded coupled lines with a characteristic differential impedance of 100 Ω. However, a differential coupled coaxial connector is not available. Therefore, the coupled differential signal must be decoupled and slowly brought into reference to the global ground resulting in two single-ended traces that can then be fed into the final connector.

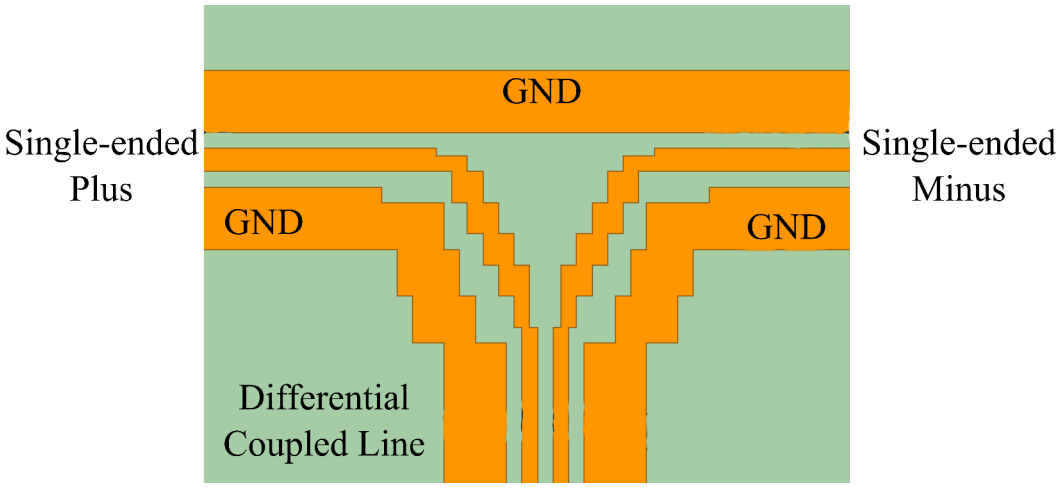

Figure 4.4: HFSS model of the differential baseband section. The minimum trace width of 100 μm is maintained. In the center, a discrete tapering can be seen with the distance between the traces slowly increasing.

To accomplish this, the signal traces are decoupled by gradually increasing the distance between the two traces as shown in Fig. 4.4. By this, the coupling coefficient is slowly decreased.

The resulting S-Parameters from the simulation can be seen in Fig. 4.5a. Here, both the differential return loss S_{11} as well as the return loss of the individual single-ended lines are below -10 dB over the entire frequency range, showing an excellent match to the system impedance of 50 Ohms.

The insertion loss is evenly split between the two traces, as the section in terms of insertion loss acts as a power splitter. At the same time, the phase relation between the two single-ended traces should be 180°. Since this is a passive structure, it can be used reciprocally as a baseband for both transmitters and receivers.

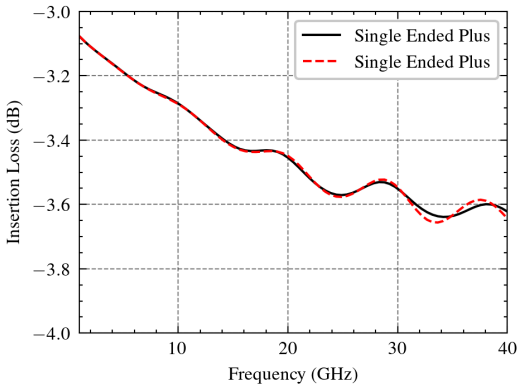

(a) Simulated insertion loss of the decoupling section. The losses are mostly due to the Ohmic and coupling losses of the copper traces.

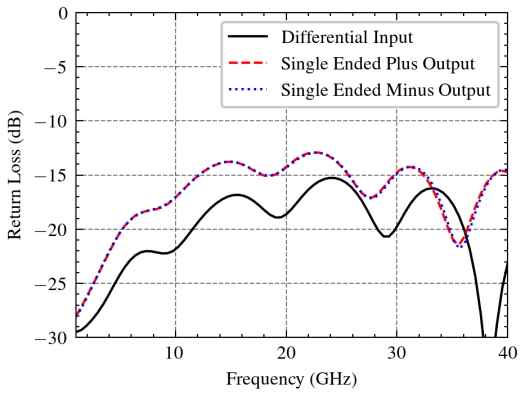

(b) Simulated return loss of the decoupling section

Figure 4.5: Simulation results of the mode decoupling section shown in Fig. 4.4.

4.1.3 Connector

In broadband/high frequency applications, the cable connector can become the bottleneck. Given the desired frequencies for the LO and baseband connections, 2.9 mm connectors are chosen (see Fig. 4.6) which are certified up to 40 GHz, exceeding the limitations of the conventional 3.5 mm connector with its cut-off frequency at 26 GHz. In order to ensure high repeatability, solderless and screwable connectors are used instead of soldering with a soldering iron. It is important that the connector-to-PCB connection is identical for each signal, as the communication system has 8 broadband inputs/outputs. This will help to avoid any unexpected behavior.

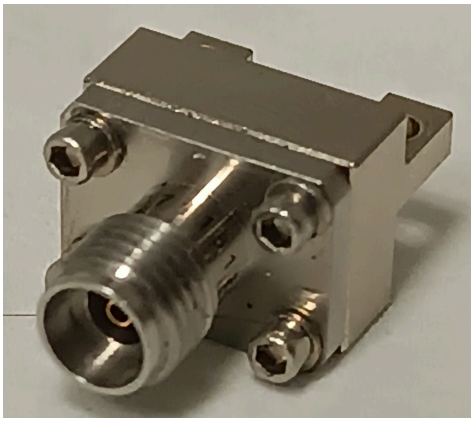

Figure 4.6: Image of the solderless 2.92 mm connector. The connector is to be screwed on the PCB with a support metal plate on the bottom side of the PCB.

At first, the connector 3D model was unavailable. As a result, the connector section was implemented as 50 Ohms lines with ground pads on the sides. Additionally, the ground pads have numerous vias to ensure a solid ground reference. However, the manufacturing company was not able to implement the desired multilayer PCB, leaving the two substrates electrically isolated from each other. Thereby, the ground

reference is only connected to the top-side of the connector, while the bottom-side is left floating. In addition to the trace recess at the PCB edges, the disconnected substrates can create resonant cavities and will affect the connector match and thus signal purity .These PCBs were used in the following chapters for the characterization of the individual transmitter and receiver and the back-to-back measurement as well.

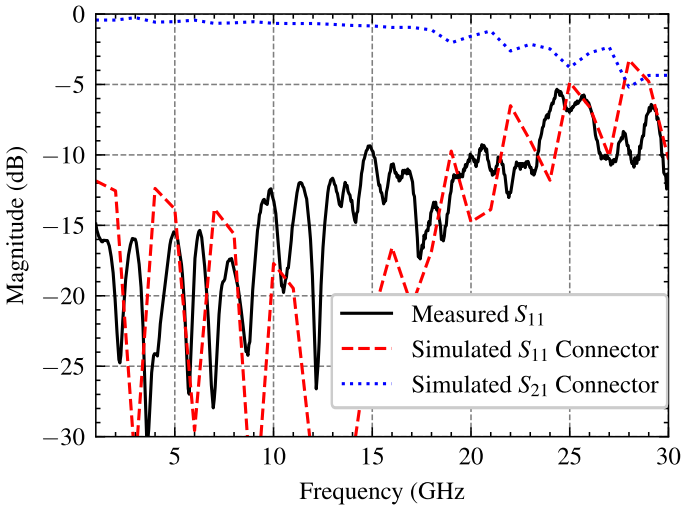

Figure 4.7: Measured return loss of the single-ended baseband and simulated connector response for the implemented PCB. The low-pass behavior is maintained until 20 GHz.

As the chips are bonded to the PCB, the insertion loss of the PCB cannot be extracted, the measured return loss is shown in Fig. 4.7. The return loss cannot be measured differentially due to the missing measurement equipment. Additionally, measurements using a broadband balun would only show the return loss of the balun which cannot be deembedded. The measured return loss shows that the full-sized PCB creates standing waves which are not visible in the simulation for the individual smaller sections. While the return loss remains below -10 dB in the shown frequency range, the expected smooth low pass behavior as seen in the bond area (Fig. 4.3) is not visible. In comparison to the simulated S-Parameter response of the implemented connector section, it is visible that the return loss increases similarly for both measurement and simulation. In the simulation however a strong resonance between 10 and 15 GHz is visible which cannot be reproduced in the measurements.

Similarly, for the LO port only the return loss can be measured as shown in Fig 4.8. While the narrow match at 26-30 GHz may correspond to the match of the LO chain and Pad, it cannot be estimated how much of the return loss is contributed by the match and how much is contributed by the losses in the PCB trace.

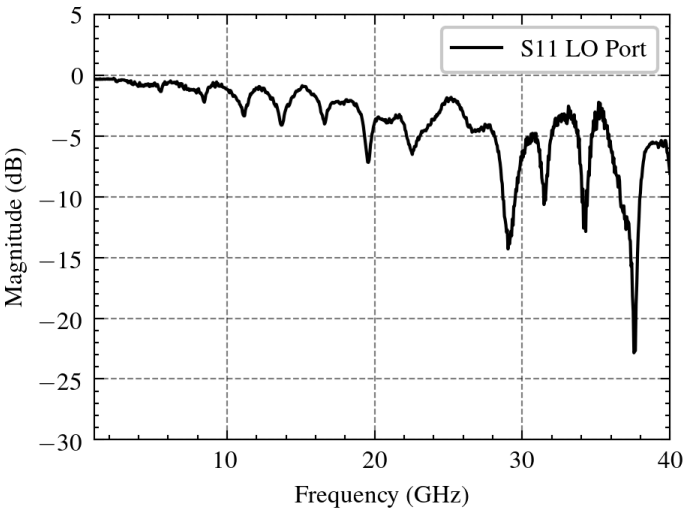

Figure 4.8: Return loss of the LO feed. At the input frequencies of the frequency multiplier the connector appears to be matched.

While the LO power could be applied to the frequency multiplier chain as shown in the next chapters, both transmitter and receiver showed a sharp frequency roll-off for varying IF frequencies (compare Chapter 5). This sharp roll-off is caused by two impairments which will be discussed below.

4.2 Impairements

4.2.1 Surface Roughness

The non-ideal surface roughness of copper can cause unwanted insertion loss, which cannot be avoided. Although various types of copper foils are available in PCB technology, not every foil is compatible with every substrates. For high-frequency substrates, a copper foil with low surface roughness such as rolled copper would be advantageous. However, only electrodeposited (ED) copper is available for the commonly used substrates. For the following analysis, the surface roughness along regular CPWs is modelled using the Huray surface roughness model in the available fullwave EM solver. In this modeling approach, the surface roughness is modelled by 'cannonballs' with defined radii that disturb the ideal surface on a metal. This surface roughness model is applied to the different surfaces of the metal traces.

The resulting insertion loss for coupled lines as used in the PCB with and without surface roughness can be seen in Fig. 4.9. The surface roughness causes a general increase in insertion loss which further acclerates for increasing frequencies.

The use of surface roughness along regular copper does not result in a sharper roll-off in frequency. Instead, this is caused by the surface finish, which will be discussed in the following section. It is important to note that surface roughness cannot be completely eliminated, and even the smoothest copper traces will have increased surface roughness

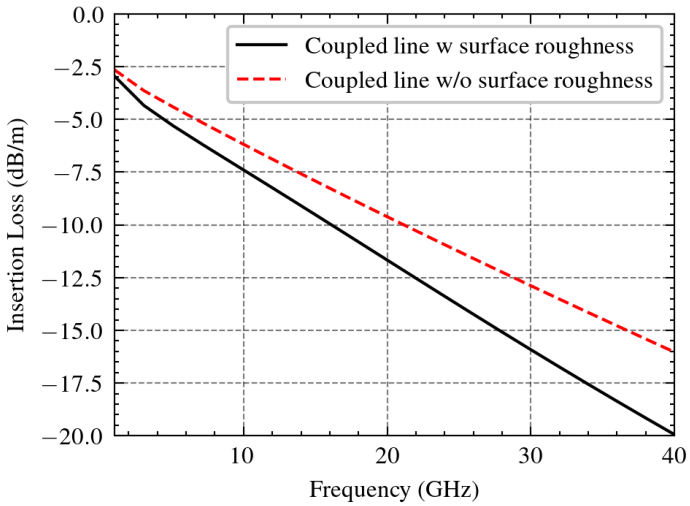

Figure 4.9: Insertion loss of coupled lines with and without surface roughness. The influence of the surface roughness increases with frequency.

after the surface finish is applied, as additional galvanic copper is added to the base copper traces.

4.2.2 Surface Finish

The PCBs are meant for interfacing the chip with external measurement instruments, the copper lines on the PCBs need to provide a surface that allows for gold wire bonding while also enabling soldering of connectors, bypass capacitors, etc. on the surface. The typical and most common surface finishes for this purpose are Electroless Nickel Immersion Gold (ENIG) and Electroless Nickel Electroless Palladium Immersion Gold (ENEPIG). Both of these surface finishes add different layers on top of the copper. The gold layer needed for interfacing with the gold bond has a thickness between 0.02 and 0.07 µm. The nickel layer in both cases has a thickness of 1 µm to 5 µm. For ENEPIG, an additional layer of Palladium (PD) is added in between the nickel and gold layer for additional adhesion (see Fig. 4.10).

For the general sizing of the transmission lines, the surface finish can be neglected as it barely changes the crosssection, with the copper thickness being at least 17 µm. It should be noted that in the application of the surface finish another layer of galvanic copper (up to 25 µm) is added to the initial copper traces, leading to a final copper thickness of 42 µm.

For regular microstrips, the surface finish has no influence because the majority of the E-field is confined to the substrate, and the current paths run along the bottom side of the copper trace and the top side of the ground plane. These surfaces are not exposed to air as they face the substrate and are left untreated in the surface finish

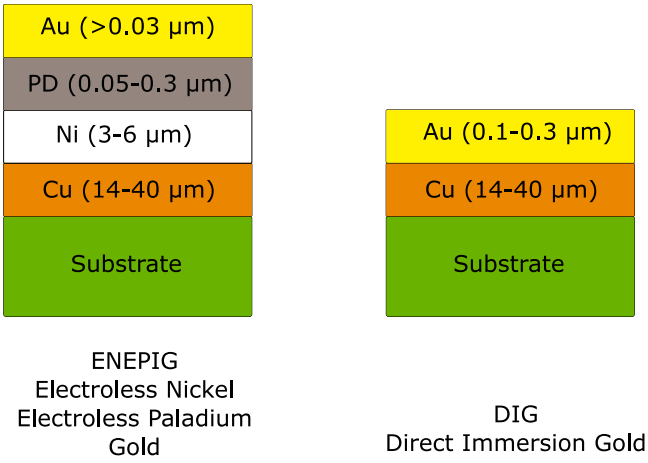

Figure 4.10: Cross section of ENEPIG and DIG surface finish.

process. For CPW, the E-field is confined in the 'plane' for strongly coupled signal and ground paths. As coupling decreases, a greater proportion of the E-field travels through the substrate. This phenomenon is significant because the surfaces along the horizontal plane undergo surface finishing, resulting in an uneven material stack along the sidewalls of the traces. In addition to the skin effect, which causes the current to occupy less surface area as frequency increases, most of the current is limited to the inner edges of the signal traces. To calculate the effective skin depth in the trace over frequency, the following formula is used:

$$\delta = \sqrt{\frac{\rho}{\pi f \mu_0 \mu_r}} \sqrt{\sqrt{1 + (\rho 2\pi f \varepsilon)^2} + \rho 2\pi f \varepsilon}. \tag{4.2}$$

This can further be simplified to [36]:

$$\delta = \sqrt{\frac{2 \cdot \rho}{2\pi f \mu_0 \mu_r}} = \sqrt{\frac{1}{\sigma \pi f \mu_0 \mu_r}}. \tag{4.3}$$

A depiction of the skin effect can be seen in Fig. 4.11 with the majority of the current flowing at the edges of the PCB trace.

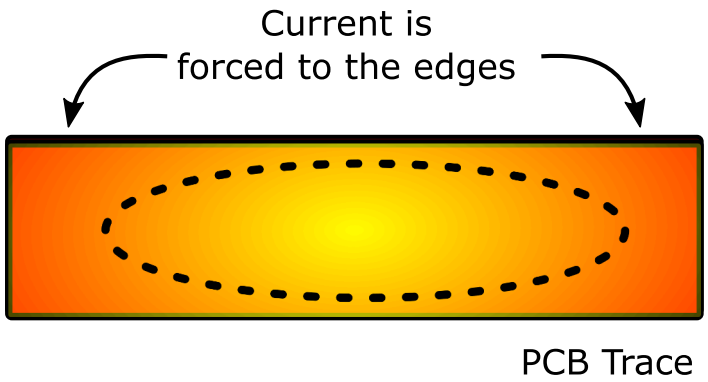

Figure 4.11: Skin effect in the PCB trace. With increasing frequency, the current does not fill the entire area but moves to the outer edges of the trace.

With the decreasing penetration depth δ, the impact of the nickel layer increases. Nickel has a conductivity (1.43×10^7 S/m) that is at least four times lower than the conductivity of Gold (4.10×10^7 S/m) and copper (5.96×10^7 S/m). The conductivity of electroless nickel is even worse by a factor of 10 in comparison to regular nickel. This alone causes higher attenuation of a coupled line in comparison to a microstrip, with the rate of attenuation increasing with frequency. Furthermore, nickel has ferromagnetic properties which directly affects the insertion loss as magnetic loss occurs as well. The magnetic permeability µ also changes the expected skin depth. However, it is difficult to determine the ferromagnetic effect of the nickel since the electroless nickel used is doped with phosphorus and its permeability is frequency-dependent. Therefore, this effect is not modeled, but it may cause differences between the simulation and measurement [97].

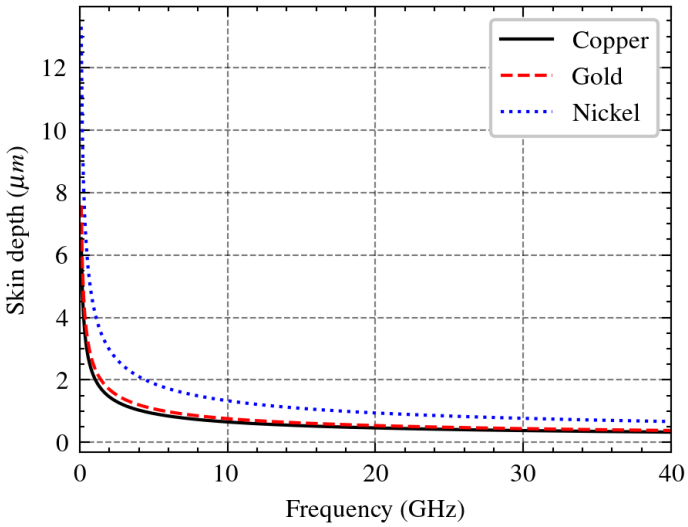

Figure 4.12: Skin depth over frequency for the different used materials in PCBs.

For further analysis, the ideal microstrip section as used in the surface roughness analysis is extended. Here, on each surface additional metal layers according to the ENEPIG stack (see Fig. 4.10) are added. The resulting insertion loss can be seen in Fig. 4.13. The added layers cause an increase in insertion loss at low frequencies while the difference to the ideal microstrip does not further increase for frequencies above 10 GHz.

By including the surface roughness in the model, the combined effect of both surface roughness and surface finish can be observed. The insertion loss at 1 GHz for low frequencies is comparable to that of the microstrip with only the surface finish. However, the difference increases significantly with frequency. Therefore, this microstrip model exhibits a sharp roll-off that ultimately restricts the bandwidth of low-pass filter sections for baseband matching, resulting in increased insertion loss along the LO

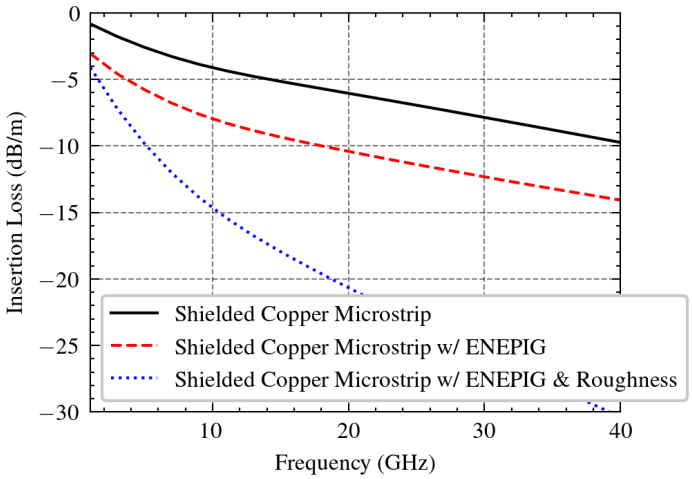

Figure 4.13: Insertion loss of shielded microstrip section with ideal, ENEPIG surface finish and ENEPIG with surface roughness. The combination of both effects show a strong deviation from the ideal microstrip.

feed transmission line. The inclusion of surface roughness in the surface finish model reveals that while neither effect significantly impacts losses in isolation, their combination results in a sharper roll-off.

Based on this findings, the use of ENEPIG can become a limiting factor for broadband packaging. As shown above the nickel layer has the lowest conductivity of the used metals. For high frequency applications, nickel-less surface finish is desired. At the same time, this surface finish should allow for gold bonding and soldering, which is not the case for e.g. hot air levelling (HAL). For these purposes, Immersion Silver and Immersion Gold (ISIG) and Direct Immersion Gold (DIG) surface finishes are typically used. ISIG is not commercially available, while DIG surface finish is only offered by a small number of PCB manufactures in Germany. In the DIG surface finishing process, the topmost copper atoms are replaced by gold atoms in contrast to the added layers in the previously described processes.

Using this surface finish in combination with the Rogers RO3006 substrate, an additional PCB was fabricated. The connector section was also remodeled using a full 3D model to improve the return loss and provide a broadband match to the microstrips and coupled lines used. The following sections discuss the simulation and measurement results.

4.3 Measurement

The fabricated PCB with the test structures including a regular CPW and coupled line can be seen in Fig 4.14. The picture shows the fully assembled PCB including the 2.92 mm connectors screwed to the PCB. The image displays coupled lines with mode decoupling at the top and a shielded microstrip at the bottom. Mode decoupling is necessary for structure characterization due to the prevalence of single-ended test equipment.

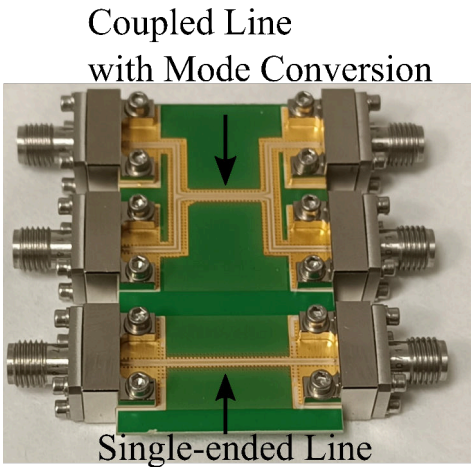

Figure 4.14: Photograph of the PCB with teststructures in full assembly with 6 connectors screwed to the PCB. At the top, a coupled line with a mode conversion section as presented in this Chapter is shown. At the bottom, a CPW as single-ended reference was placed.

The PCB was characterized using a VNA and signal power measurements. The expected simulation results are shown in Fig. 4.15. The simulations show a broadband match up to 40 GHz with a steady decrease in insertion loss as expected for regular transmission lines. The implemented microstrip shows a insertion loss of 1 dB at 20 GHz. The following plots show the input reflection for two different terminations (Short, Load) connected to the opposite side of the single-ended microstrip.

For further analysis of the manufacturing influence on the assembly, the PCB edges are grinded down using sand paper to achieve increasingly shorter distances between the board edge and signal pin. In the short terminated measurements a resonance appears at 28 GHz (Fig. 4.16). This resonance is removed by decreasing the distance of the pin to the edge of the PCB. Thereby, the resonance is moved above 30 GHz but cannot be completely removed. The return loss measurement of the load termination allows to analyze the broadband match when the microstrip and connector section is connected to the baseband section.

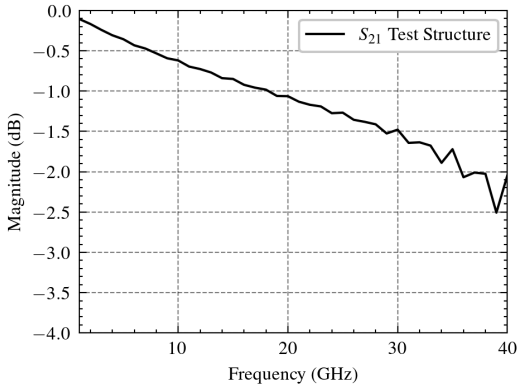

(a) Simulated insertion of the microstrip transmission line.

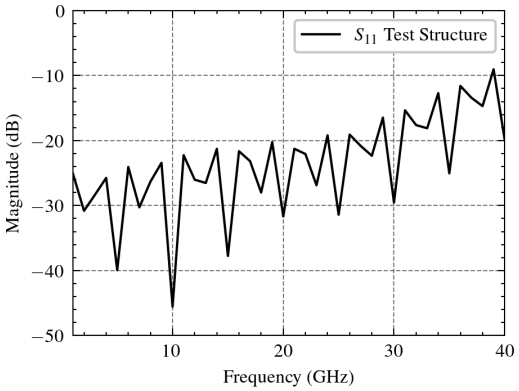

(b) Return loss of the microstrip transmission line

Figure 4.15: Simulated insertion and return loss of the microstrip transmission line on the fabricated PCB test structures. The insertion loss shows a linear roll-off until 35 GHz, while the return loss is below -10 dB up to 40 GHz.

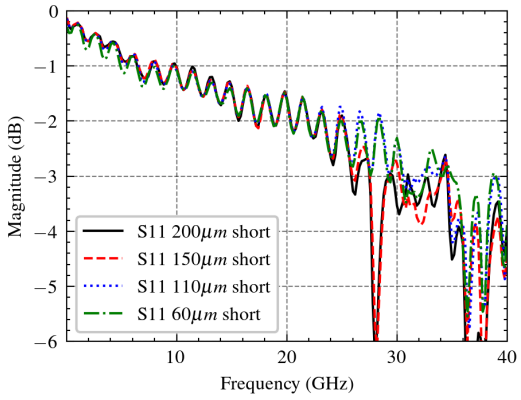

(a) Measured return loss of the single-ended microstrip using Short Termination

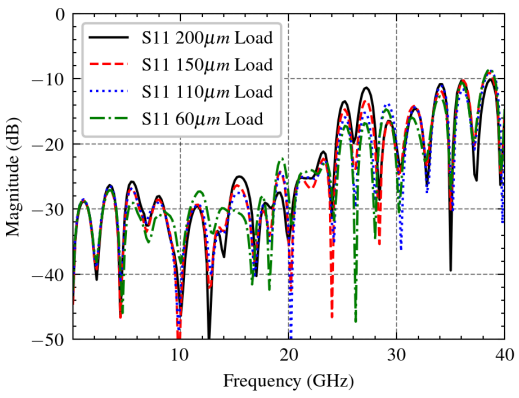

(b) Measured return loss of the single-ended microstrip using Load Termination

Figure 4.16: Measured return loss of the single-ended microstrip with short and load termination. The insertion loss displays a linear roll-off up to 30 GHz, while the measured return loss increases above 25 GHz.

The load terminated measurements show that the connectors are well matched to 50 Ω up to 25 GHz (Fig. 4.16). By further reducing the pin distance, the return loss is improved by 4 dB above 25 GHz.

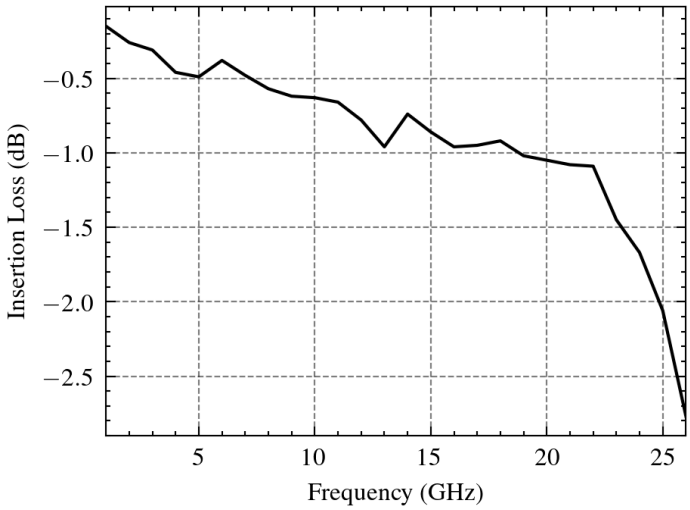

Figure 4.17: Measured insertion loss using signal generator and spectrum analyzer. The measured insertion loss aligns with the simulated insertion loss shown in Fig. 4.15.

The measured insertion loss shown in Fig. 4.17 displays the expected behavior as shown in the simulated results (Fig. 4.15). Through this measurement, it can be shown that the DIG surface finish in combination with the high-frequency substrate can be modeled well and therefore a succesful implementation of an improved communications PCB should be possible.

4.4 Summary and Conclusion

For broadband communications systems, the design of the integrated chip cannot be done without taking the packaging into consideration. The design of transmitters and receivers with multiple differential mixer outputs as well as their individual DC biasing creates a large number of signal pads that need to be bonded to PCBs. This challenge will further increase for massive MIMO systems where the amount of broadband baseband inputs/outputs will scale with the number of channels. Therefore, the design of packaging for 'simple' communications systems will continue to move towards high density packaging.

The high package density in combination with the high required bandwidth requires added complexity in the PCB design. As shown in this chapter, a regular 50Ω microstrip line on PCB has a width equal to almost half of the entire transmitter die width. The limited space for the fan-out was met with high frequency substrates as well as coupled lines for the baseband interconnects. Thereby, the baseband and LO interconnects could be designed under the constraints of limited design area. In addition, this still left enough space for the DC biasing of the TX and RX.

The presented shielded coupled lines allow interfacing to differential IQ mixers with minimal width. In addition, a mode decoupling structure was developed to decouple the differentially coupled-lines and make them accessible for single-ended connectors. However, the coupled line, in combination with the necessary surface finish for gold bonding, results in unexpected insertion loss. Additionally, the PCB to connector interface was initially not properly manufactured. In the implemented communication PCBs, the multilayer PCB has two substrates which are electrically isolated from each other due to the missing through-vias from the top to the bottom side of the PCB. Therefore, the ground reference of the connector is only connected to the topside ground of the PCB. As shown in this Chapter, the improper implementation of the connectors reduces their bandwidth to 15 GHz, while the added insertion loss of the used transmission lines further decreases the bandwidth of the baseband connections.

For the LO generation input, the measured S-Parameters showed a percepted match at the design frequency, however at the same time, the measurement displayed multiple resonances. In combination with the sharp cut-off of the connector matching, it remains unclear whether the LO generation can be excited. It is expected that both the connector as well as the incorrect matching of the LO creates reflections in the PCB which cannot be extracted in the measurement. Additional S-Parameter measurements between the baseband ports and the LO port showed no transmission between these ports.

It is expected that the improper PCB implementation in combination with the increased insertion loss leads to a reduced bandwidth when combined with the transmitter and receiver presented in the previous Chapter 3. While the problems regarding the surface finish and connector design were identified and solved for PCB test structures, these changes were not implemented in the measured TX and RX due to the advanced state of this dissertation. The problems shown in this Chapter were mostly identified in the characterization process of the fully packaged communications system.

In this chapter, the challenges for packaging of communication chipsets with a large number of inputs was shown. For future massive MIMO implementations, it is expected that these challenges remain and will become more severe and therefore also need to be met by sophisticated circuit design. In the following Chapter 5, the RF performance of the individual TX and RX will be presented including the PCB implementation imperfections presented in this Chapter.

Chapter 5

Dual-Polarization MIMO

The previous chapters introduced the design and performance of the individual building blocks was presented. According to the results in Chapter 3, the implemented circuits should enable communication at carrier frequencies around 300 GHz. To evaluate the performance of the implemented dual-polarized TX and RX, a broadband, high-frequency packaging was introduced in Chapter 4. This chapter evaluates the RF performance of the implemented and packaged TX and RX through individual characterization.

Based on the measurements presented in this chapter, it can be determined whether the integration of the building blocks into full systems was successful and communication can be achieved as will be later shown in Chapter 6. Similar to Chapter 3, first the antenna will be evaluated as it is identical for both TX and RX, before the individual RX and TX performance will be presented.

5.1 Antenna Measurement

Both the transmitter, as well as the receiver include dual-polarized antennas for polarization diversity based MIMO similar to [56] as described in Chapter 3. In contrast to linear polarized antennas, the characterization of the radiated power cannot be derived from a single measurement due to the unavailability of circular polarized test equipment.

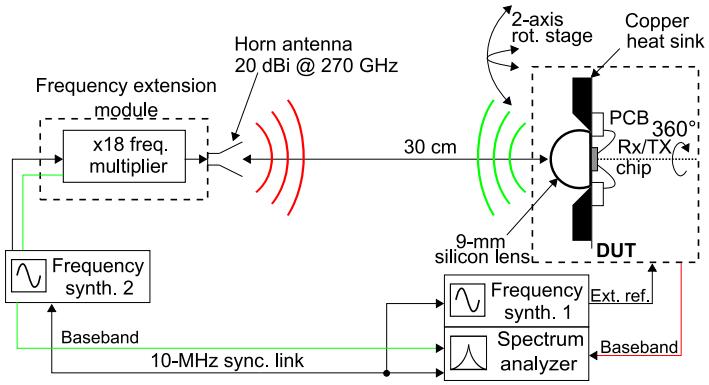

Figure 5.1: Measurement setup for the radiation pattern measurement of both TX and RX. For the TX (green) and RX (red) characterization, the OML VNA frequency extender is used as a receiver or transmitter, respectively.

As shown in Fig. 5.1, the antenna measurement is done using OML VNA frequency extenders in either receive or transmit mode depending on the measured circuit (TX or RX). The DUT is mounted on a electrically steerable stage allowing for rotation in the ϕ and Θ planes in a cylindral coordinate system. Thereby, the DUT can be tilted towards the respective angular position. A linear-polarized standard gain horn antenna is mounted on the waveguide port of the OML frequency extender. Due to the linear-polarized test antenna, only one projection of the emitted circular polarized wave can be received by the OML module (for TX transmission) as described in Chapter 2. To capture the entire radiation pattern of the lens-integrated antenna, the DUT must be measured at two different - orthogonal - positions. For this, the DUT can be turned along its poynting vector.

Thereby, the radiation along the major and minor axis of the circular polarized antenna can be measured. As an example, the normalized received radiation pattern for both projections of circular polarized antenna at 270 GHz is shown for one polarization of the transmitter (see Fig. 5.2a & Fig. 5.2b). While for one projection (Fig. 5.2a), the measured directivity is 23.4 dBi, the other projection (Fig. 5.2b) shows a higher directivity of 24.09 dBi.

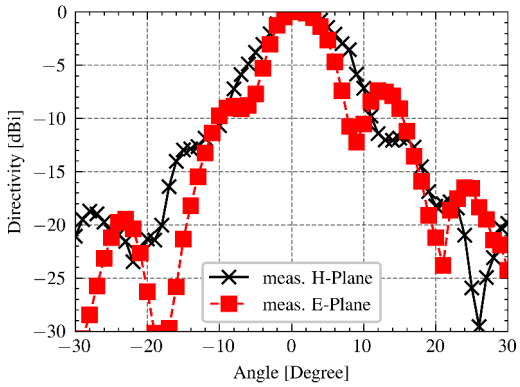

(a) Measured antenna radiation pattern for one projection at 270 GHz, resulting in a Directivity of 23.4 dBi. The radiation pattern shows irregular side lobes on both sides of the main lobe. Additionally, the width of the main lobe is not equal for both E- and H-Plane cuts.

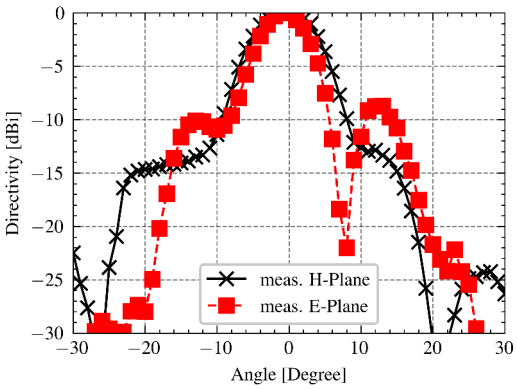

(b) Measured antenna radiation pattern for one projection at 270 GHz, resulting in a Directivity of 24.09 dBi. The E-Plane cut shows a clear zero between the main lobe and side lobe in one direction.

Figure 5.2: Measured antenna radiation pattern for both projections at 270 GHz.

In the presented radiation patterns, the width of the main lobe is different for both E- and H-Plane cuts. Similarly, the side lobe pattern is different not only for E- and H-Plane, but for each plane individually.

As previously explained, the total radiation pattern is the superposition of the two measured projections. The result of this superposition can be seen in Fig. 5.3a. Here, the width of the main lobe is identical for both cuts. In addition, the superposition of the measured radiation patterns creates the mean of the previously irregular side lobes. For the superposition of the two radiation patterns, a directivity of 23.94 dBi is calculated at 270 GHz. This measured directivity is later on used for the path loss deembedding in the measurements presented in this chapter.

The chosen representation only presents the radiation pattern along two orthogonal cuts, by projecting the measured radiation pattern on a 2D-Array, the gaussivity of the final beam is visualized as shown in Fig. 5.3b.

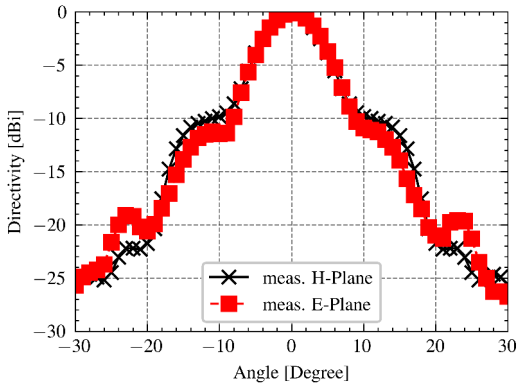

(a) Measured antenna radiation pattern for both projections at 270 GHz. The side lobes and main lobe are equalized through the superposition of the individual radiation patterns. A total directivity of 23.94 dBi is extracted.

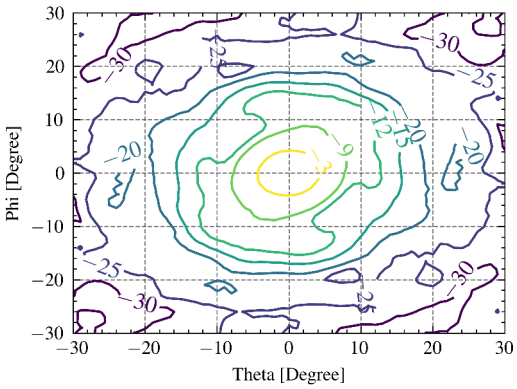

(b) Contour projection of the measured radiation pattern at 270 GHz. The contour projection extends the observed area from the two orthogonal cuts to a full 30x30 array.

Figure 5.3: Superposition of the measured antenna radiation pattern for both projections at 270 GHz. Displayed as E-/H-plane cuts and full 2D contour.

Both transmitter and receiver show similar directivity behavior over frequency for both polarizations respectively. As expected, the measured directivity increases with frequency due to the increasing lens aperture with respect to the wavelength. The resulting directivity over frequency is shown in Fig. 5.4.

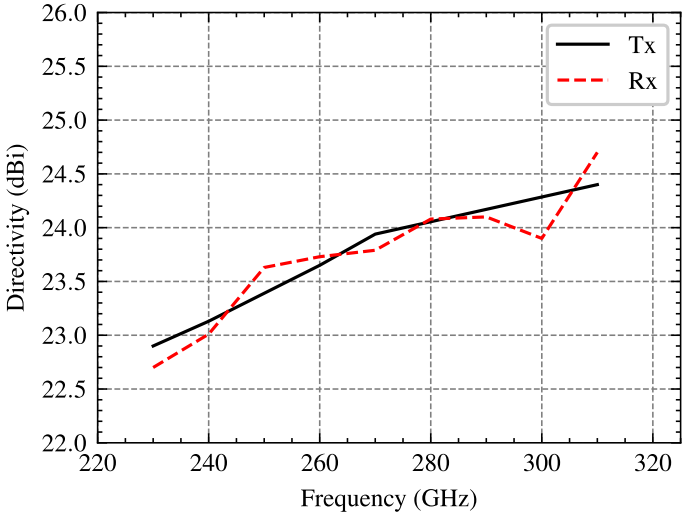

Figure 5.4: Antenna directivity for both TX and RX for different LO frequencies. The directivity stays between 22.7 and 24.5 dBi for both.

Due to the steady increase and similarity between transmitter and receiver and the respective polarizations, the radiation patterns for the different combinations as well as frequencies is not shown in this dissertation.

5.2 Receiver

In the following, the RF characterization of the implemented dual-polarized RX will be presented. The respective block diagram and chip micrograph can be found in Chapter 2 and will not be shown at this point.

In the receiver characterization, first the conversion gain of the RX will be characterized. Based on the measured conversion gain, the noise figure of the total receiver can be determined. The conversion gain characterization also allows us to measure the achieved RF bandwidth of the receiver and therefore identify whether the simulated bandwidth from the individual building blocks and packaging can be maintained.

5.2.1 Conversion Gain

5.2.1.1 RF/LO Bandwidth

As the receiver is first characterized without its counterpart, the CG is measured using test equipment. For this, the OML VNA extender used in the antenna characterization is used as a single-tone source. The output power of the OML VNA extender - which has been measured using a PM4 power meter - is used in combination with the known antenna gains on both the source and receiver side to estimate the received power of the RX. Thereby, the CG of the receiver is then given by the difference between the received power $P_{av,RX}$ and the power reading of the spectrum analyzer. This is first done for both I and Q mixer independently for varying LO frequencies with a constant IF frequency offset of 33 MHz with the results shown in Fig. 5.5.

The measured conversion gain here is shown for the desired fundamental operation of the mixer, as well as the sub-/ and superharmonic operation of the mixer using the different LO harmonics. Through this measurement, the RF/LO 3-dB bandwidth can be measured starting from 243 GHz to 305 GHz. This bandwidth is identical to the measured LO generator bandwidth as shown in Chapter 3. Thereby, it can be derived that the generated LO power is sufficiently high to achieve near constant conversion gain in the complete frequency range.

The shown downconverted mixing products of the undesired harmonics of the frequency multiplication stages is not directly proportional to the harmonic suppression shown in Chapter 3. The here shown sub-/superharmonic conversion gain is rather related to the mixer's nonlinear downconversion with the provided harmonic power. Nonetheless, the receiver shows a harmonic separation of >30 dB from 260 GHz to 305 GHz.

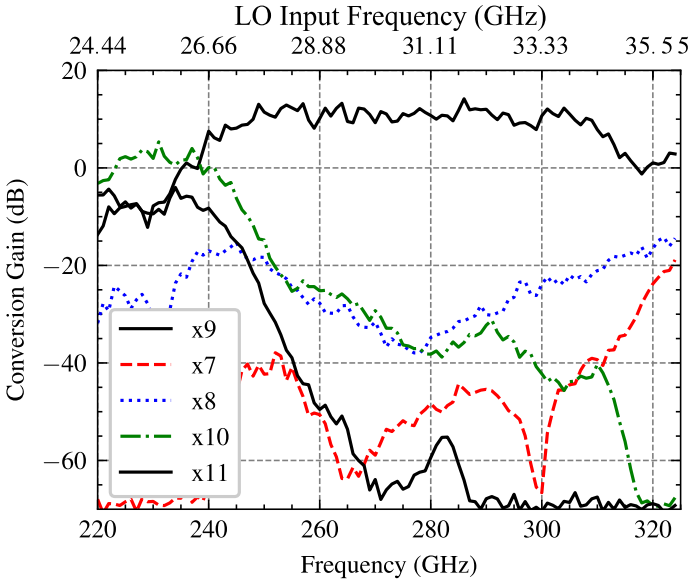

Figure 5.5: Harmonic mixing products of the RX for the different harmonics of the LO frequency generation. From 245 GHz up to 310 GHz, the conversion gain of the undesired harmonics is more than 30 dB below the desired harmonic mixing.

In the measurements, the different biasing points of the mixer, frequency multiplier stages and LO power amplifier were varied. For the shown RF/LO bandwidth, the changes in the suppression and conversion gain were neglectable and are therefore omitted from this dissertation. By varying the power amplifier bias, the gain can be slightly adjusted as shown in Chapter 3 and [own1]. As the conversion gain does not react to this gain variations, the mixer is not limited by the provided LO power.

5.2.1.2 RF/IF Bandwidth

As the transmitted power of the used OML module cannot be varied, the linearity of the RX cannot be characterized. The OML transmits power below -20 dBm which in combination with the path loss leads to low received power levels, therefore only the small-signal response of the receiver frontend can be measured. For communication receivers, the RF/IF bandwidth is of highest interest which was also shown in the description of the individual building blocks. For this, the LO frequency of the RX is kept constant while the RF frequency generated by the OML module is varied.

Thereby, the IF bandwidth for different LO frequencies is measured as shown in Fig. 5.6. Here, it becomes clear that the LO power is not sufficient for mixing at 240 GHz as shown in Fig. 5.5. This can also not be improved by adjusting the base-collector voltage or the multiplier chain. For the other LO frequencies, a peak CG of around

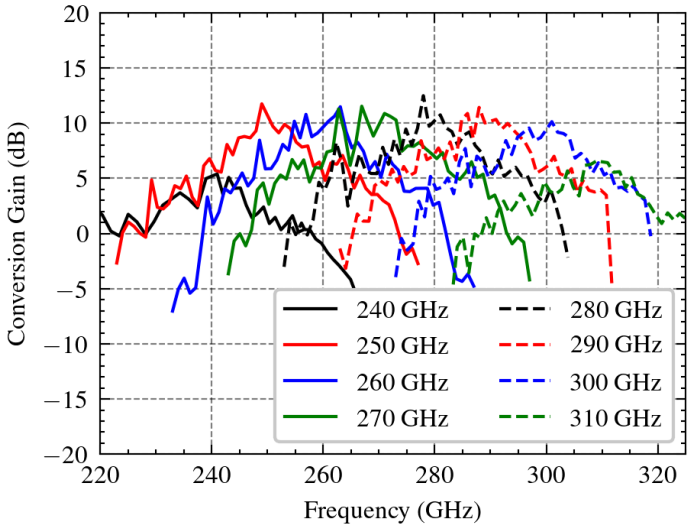

Figure 5.6: Conversion gain of the receiver for different LO frequencies in 10 GHz steps while the received signal is swept in 1 GHz steps. At the band edges (240 & 300 GHz), the LO power is insufficient for amplification, in the center of the band a maximum conversion gain of 10 dB for different LO frequencies is achieved.

10 dB can be seen. It should be noted that the measured conversion gain is for SSB downconversion, as only one RF tone can be generated at a time. The total 3-dB conversion gain bandwidth based on this measurement spans from 243 to 305 GHz similar to the previous measurement.

While the total receiver bandwidth can be read from this plot (Fig.5.6), the individual IF bandwidth cannot be easily extracted here. For this, the IF bandwidth for 250 GHz (Fig. 5.7a) and 260 GHz (Fig. 5.7b) can be observed. From this, the IF bandwidth can be read with an IF bandwidth of more than 9 GHz for the USB, while the LSB bandwidth is about 8 GHz. This is in contrast to the simulated bandwidth of the TIA in Chapter 3 and also lower than 17 GHz expected from the bandwidth limitation of the on-chip baseband routing. The difference of 10 GHz between the measured RX bandwidth is then caused by the combination of the lossy baseband packaging (Chapter 4) with the bandwidth-limited baseband output. As described in Chapter 4, the influence of the Nickel in the surface finish on the bandwidth could not be simulated, therefore it cannot be ruled out as the main contributor. For correct evaluation of the RF/IF bandwidth, the receiver needs to be measured again using optimized PCBs.

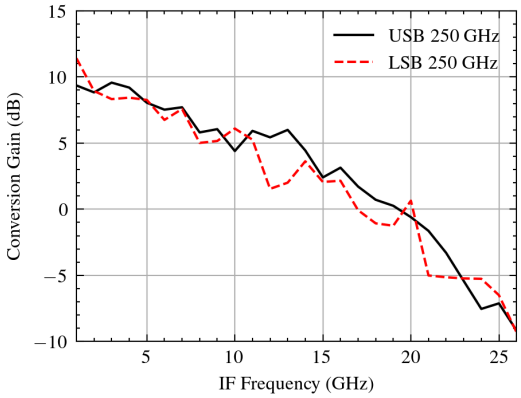

(a) Conversion gain of the receiver at a LO frequency of 250 GHz for both upper and lower sideband.

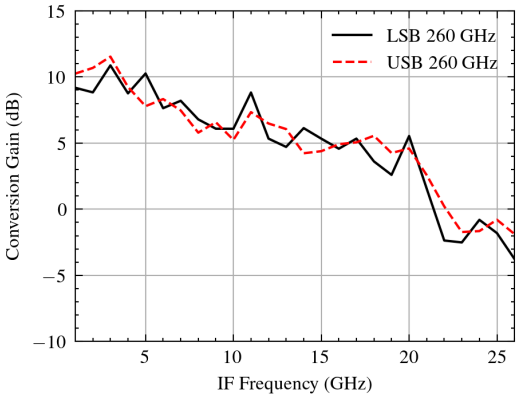

(b) Conversion gain of the receiver at a LO frequency of 260 GHz for both upper and lower sideband.

Figure 5.7: Conversion gain of the receiver at 250 and 260 GHz. For both LO frequencies, Upper Side Band (USB) and Lower Side Band (LSB) is shown. The conversion gain is almost identical for both sidebands, while the bandwidth slightly differs.

LO Freq. (GHz)	CG (dB)	LO Freq. (GHz)	CG (dB)
240	5	280	10
245	8.5	285	10
250	9.5	290	10
255	10	295	9
260	10	300	9
265	11	305	9
270	10	310	7
275	10		

Table 5.1: Conversion gain for different LO frequencies in the receiver. The conversion gain remains flat in the center of the band, while the outer edges exhibit lower conversion gain due to the decreased LO power.

For other LO frequencies which will not be shown here in detail, the 3-dB IF bandwidth is around 8 GHz. Here, it should be noted that this bandwidth only describes the frequency-amplitude behavior of the receiver+packaging while the phase cannot be observed. The respective conversion gain for different LO frequencies can be seen in Table 5.1. As mentioned earlier, the LO power is insufficient for mixing at 240 GHz, while for other LO frequencies, the conversion gain is maintained.

5.2.2 Noise Figure

Due to the lack of noise sources and standardized measurement equipment in the frequency range above 200 GHz, the noise figure of the receiver cannot be directly extracted and relies on de-embedding of the conversion gain of the receiver and additional measurement equipment. A simplified block diagram for the noise figure calculation is shown in Fig. 5.8

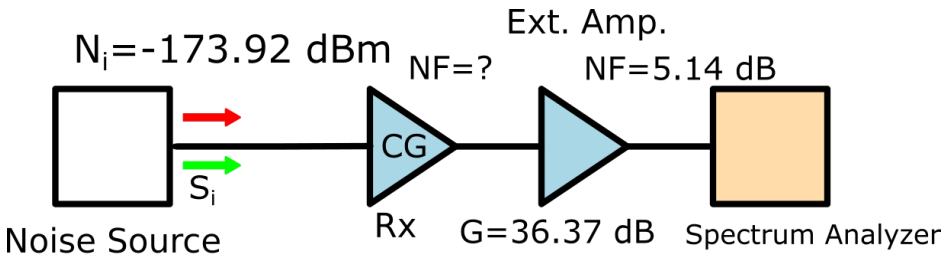

Figure 5.8: Block diagram showing the noise figure calculation of the receiver. The initial noise in the system is purely thermal. Based on the noise power reading on the spectrum analyzer, the different known terms - in this case the external amplifier's Gain (G) and Noise Figure (NF) and the CG of the Receiver can be de-embedded.

Firstly, we assume that the noise source is purely thermal. Therefore, the thermal noise floor is calculated as:

$$NoiseFloor_{dBm} = 10 * \log_{10}(kTB/1mW) \tag{5.1}$$

with k being the Boltzmann's constant, T the temperature in Kelvin - in our case around 294 Kelvin, and B is the bandwidth which is here set to 1 Hertz. Therefore, the $NoiseFloor_{dBm}$ is -173.92 dBm in our case. It should be noted that the noise marker in a spectrum analyzer also gives the noise power in relation to the 1 Hz Bandwidth, which facilitates the following calculation.

The noise was measured with the spectrum analyzer using a pre-amplifier from Mini-Circuits with a Gain of 36.37 dB and a NF of 5.14 dB at 50 MHz. At an LO frequency of 260 GHz, the noise marker value of -107 dBm was taken from the spectrum analyzer.

To now sucessfully estimate the noise figure from this measurement, the Gain and NF of the pre-amplifier as well as the CG of the Rx (10dB) and the losses of the balun have to be substracted from the noise power reading. The total difference of this value (-159.51 dBm) and the thermal noise floor then give the total noise figure of the Rx at this specific LO frequency and mixer biasing.

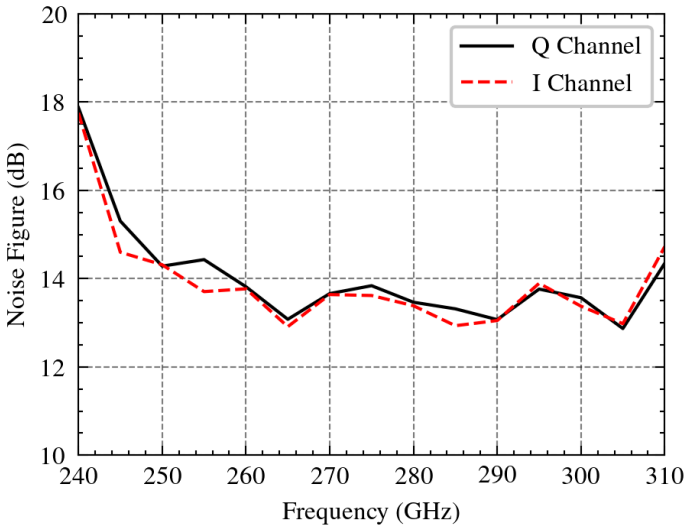

Figure 5.9: Single sideband noise figure of the receiver for different LO frequencies. Again, the conversion gain at the center of the frequency band leads to a low noise figure.

For the varying LO frequencies and the two different mixers, the single sideband noise figure can be calculated by using the CG as shown in Table 5.1. The resulting noise figure over frequency can be seen in Fig. 5.9. The measured noise figure is below 14 dB from 258 to 308 GHz for both I and Q mixer. The I mixer shows a slightly better noise figure which, however, is in the measurement tolerance of the noise figure de-embedding. At the band edges, the noise figure increases rapidly due to the decreased conversion gain of the receiver.

As the double sideband CG cannot be measured due to the lack of the respective source, the double sideband noise figure can only be calculated from the single sideband noise figure and is 3 dB lower.

In comparison to existing LNAs in this frequency range [32], the measured Noise Figure is slightly higher (about 2 dB at 250 GHz), however in the receiver the added losses of the antenna with its hybrid also contribute to a higher noise figure. Therefore, the receiver noise figure and LNA noise figure in identical technologies is assumed to be nearly identical. Based on this, an LNA first receiver will not have an SNR advantage compared to the implemented mixer first receiver.

Despite the increased operating frequency, the here presented noise figure is on the same level as for communications systems operating around 240 GHz [6] showing a succesful implementation of a broadband receiver design without major noise deterioration. The noise here is ultimately limited by the used transistor technology and mixer topology as full gilbert cell downconversion mixers in this frequency range present an increased noise figure generated by the transconductance pair [61].

5.2.3 IQ Imbalance of the Receiver

The IQ imbalance of the receiver can be extracted as well from the respective IF sweeps (Fig.5.7a). By substracting the received power values from each other, the IQ imbalance between the two mixers is calculated. The resuling I/Q imbalance can be seen in Fig. 5.10. The receiver shows an identical IQ imbalance for the majority of the LO frequencies, that is below 0.8 dB up to 9 GHz. For frequencies above 10 GHz, this I/Q imbalance rapidly detoriates and therefore is also not shown for IF frequencies above 12 GHz. As shown in Chapter 3, the implemented baseband routing of the respective I and Q baseband outputs indicate a high likelihood for an increased IQ imbalance which also expected to be IF frequency dependent. This effect cannot be circumvented without a redesign of the routing as proposed in Chapter 3.

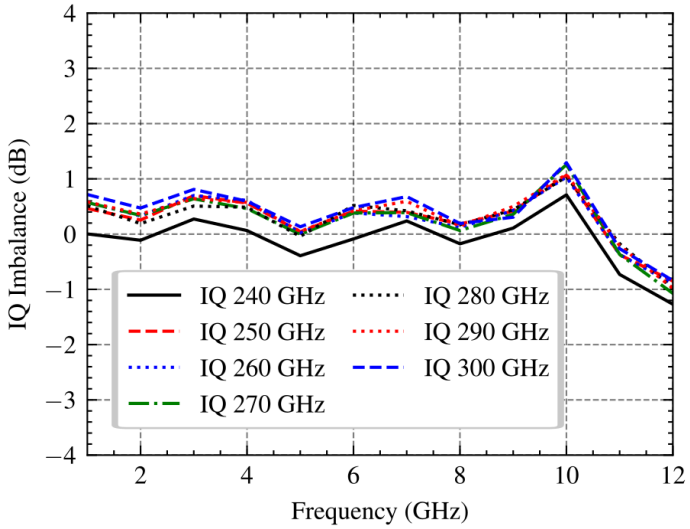

Figure 5.10: IF frequency dependent IQ imbalance of the receiver at different LO frequencies spanning from 240 GHz to 300GHz. The IQ imbalance remains below 1 dB for LO frequencies between 240 GHz and 310 GHz up to a IF frequency of 10 GHz.

The high insertion loss of the PCB in this case should not contribute to the IQ imbalance as both outputs are designed identically. However, as the influence of the surface finish on the coupling cannot be correctly estimated and the coupled lines are not matched well to the connector, additional I/Q crosstalk could be generated by the PCB. To isolate this, the fastest way is to redesign the PCB with the improved connectors and surface finish as proposed in Chapter 4.

The I/Q generation in the LO generation through the differential coupled line 90° Hybrid (Chapter 3) is independent to the used IF frequency and is best read from the RF/LO bandwidth measurements where a small IF frequency of 33 MHz is chosen. Due to the small IF frequency, it is expected that the routing and PCB induced IQ imbalance is constant. The respective 'static' IQ imbalance of the receiver for different LO frequencies is shown in Fig. 5.11. The IQ imbalance is below 0.3 dB over the entire usable frequency range, only at the upper frequency band edge it increases to 0.5 dB which is most likely related to decreasing phase and amplitude balance in the used hybrid.

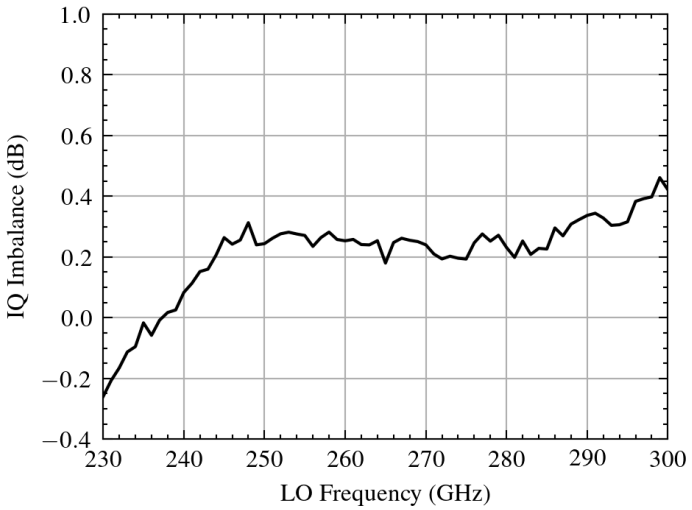

Figure 5.11: IQ imbalance of the receiver at different LO frequencies spanning from 240 GHz to 300GHz. It can be shown that the IQ imbalance is very low (below 0.4 db) for low IF frequencies of 33 MHz.

All in all, the measurements of the receiver show that downconversion of signals with carrier frequencies around 300 GHz is possible using the implemented circuits (Chapter 3) in the advanced 0.13 µm SiGe BiCMOS technology. However, the usable bandwidth of the receiver is reduced due to the design issues as indicated in Chapter 3 and the further decreased bandwidth of the used PCB.

Based on this, the Rx presents a potential bottleneck for broadband communication, which is contrary to the findings in [60] where the mixer-first receiver approach has a

higher bandwidth than the used amplifiers. While the RF/LO bandwidth shows a high bandwidth from 243 to 305 GHz, this bandwidth cannot be maintained in the RF/IF bandwidth measurement due to the increased insertion loss of the packaging. The measured noise figure is on-par with communications system implementations operating around 240 GHz showing that the technological improvements allow to maintain similar performance despite the increased operating frequency.

5.3 Transmitter

In the following, the RF characterization of the TX will be discussed. For transmitter characterization, the OML VNA frequency extender is used as a receiver. For this, the conversion gain of the used frequency extender is first measured using a back-to-back connection of two OML VNA frequency extenders with the output power of the transmitting OML module known through the previous output power measurement using the PM4 Power Meter. The conversion gain of the OML module is later on deembedded in combination with the path loss to achieve accurate reading of the transmitted output power of the TX. The power measurement setup and deembedding method is similar to the one used in [84], with the difference that the power measurement of the transmitter is performed in free space.

First, the transmitter's large signal behavior will be investigated similar to the input power sweeps shown for the power amplifier (Chapter 3) at different IF frequencies. The compression behavior is analyzed for both single mixer operation and simultaneous operation of both I and Q mixers. In addition, the IF frequency will be varied to extract the IF/RF bandwidth. Ultimately, the harmonic suppression of the transmitter will be measured where the LO/RF bandwidth is extracted as well.

5.3.1 Compression

As previously described, the compression of the transmitter using a single mixer is analyzed first. For this, a signal generator in combination with an external discrete balun is used to provide a differential IF signal at the baseband input of the mixer. For this compression, the mixing products generated by the baseband upconversion are measured as well. The relevant mixing products are the upconverted 2^{nd} and 3^{rd} harmonic which are spaced accordingly relative to the LO frequency.

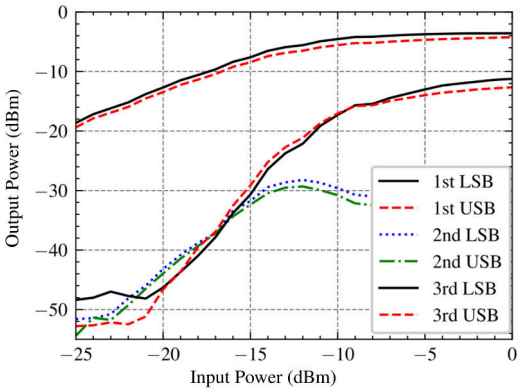

(a) Large signal measurement results of the transmitter at 255 GHz. At this frequency, both sidebands are almost equal. A high 2^{nd} order harmonic is visible.

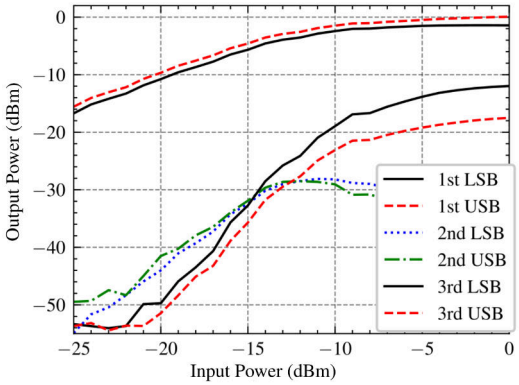

(b) Large signal measurement results of the transmitter at 260 GHz. At this frequency, both sidebands exhibit sideband asymmetry for a frequency difference of 6 GHz. A high 2^{nd} order harmonic is visible. The output power is increased by 2 dBm compared to 255 GHz.

Figure 5.12: Large signal measurement results of the transmitter for LO frequencies of 255 and 260 GHz. For both LO frequencies, the 2^{nd} order harmonic product is clearly visible. At 260 GHz, a sideband asymmetry is visible.

The resulting single mixer compression curve for the Q mixer at 255 GHz for an IF frequency of 3 GHz is shown in Fig. 5.12a. The respective 2^{nd} harmonic ($\pm$ 6 GHz) and 3^{rd} harmonic ($\pm$ 9 GHz) are displayed as well. The input power is limited by the minimum output power of the used signal generator. Furthermore, both LSB and USB curves are shown in this figure, displaying nearly identical behavior. The TX generates both LSB and USB simultaneously, therefore the total transmitted power of the TX based on this measurement is about -1 dBm.

At 260 GHz, a sideband asymmetry is already visible in combination with an increased saturated power level to 2.13 dBm. This increase in power is unexpected, furthermore the sideband asymmetry is already visible for low IF frequencies. For the RX measurement, it was visible that the PCB did not lead to sideband asymmetry but reduced the bandwidth, therefore it is also expected that this sideband asymmetry is not related to the PCB but to on-chip asymmetry and errors in the deembedding.

Nonetheless, the individual mixer compression curves at both LO frequencies showed that the 2^{nd} order harmonic is high. As this can directly affect the link quality, the origin of this second order harmonic will be discussed in the following.

5.3.1.1 Harmonic Distortion

In the mixing process of a double sideband upconversion mixer, the mixing products closest to the LO frequency are $f_{LO} \pm f_{IF}$, $f_{LO} \pm 2f_{IF}$ and $f_{LO} \pm 3f_{IF}$. For an ideal linear mixer only the desired $f_{LO} \pm f_{IF}$ should exist whereas the 2^{nd} and 3^{rd} order mixing products do not exist. For the implemented differential upconversion mixer (Chapter 3), only the 3^{rd} order mixing product should exist when the mixer compresses. This undesired 3^{rd} harmonic tone is proportional to the input signal power squared. The existence and suppression of the additional harmonics in the TX is also called harmonic distortion (HD)

In the ideal TX simulation at 260 GHz (Fig. 5.13), this 3^{rd} order mixing product exists, and similar to the measured large-signal compression (Fig. 5.12b), it is around 10 dB smaller then the desired mixing product's power at full compression. In contrast to the measurement, the 2^{nd} upconversion is nonexistent, with a harmonic suppression of this tone by nearly 50 dB. Therefore, it can be concluded that the observed behavior is unexpected for ideal differential baseband excitation of the transmitter.

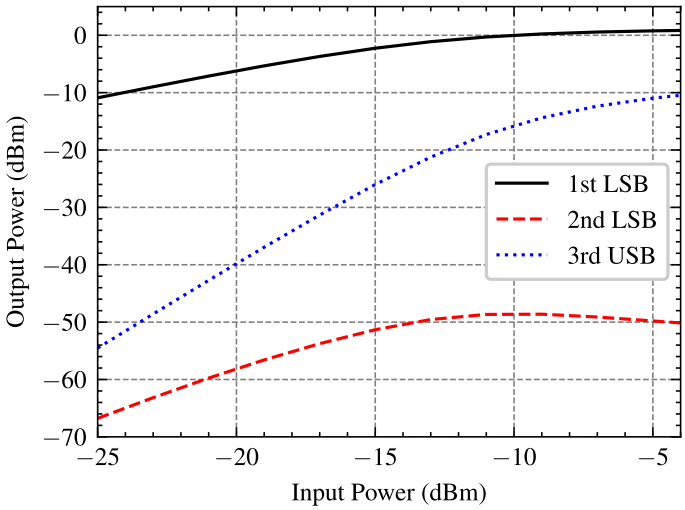

Figure 5.13: Simulated single mixer compression at 260 GHz with an IF frequency of 3 GHz. In the ideal case, the 3^{rd} order harmonic is well suppressed.

For ideal differential baseband excitation, the 2^{nd} order distortion should only be generated in the common mode of the upconversion mixer and directly be rejected by the output transformer of the mixer. Therefore, the measured 2^{nd} order mixing product appears to be differential. This however can only be the case for imperfect differential excitation.

In Fig. 5.14, the compression of an artifically mismatched upconversion mixer is shown. In simulation, this was achieved by varying the emitter degeneration of the

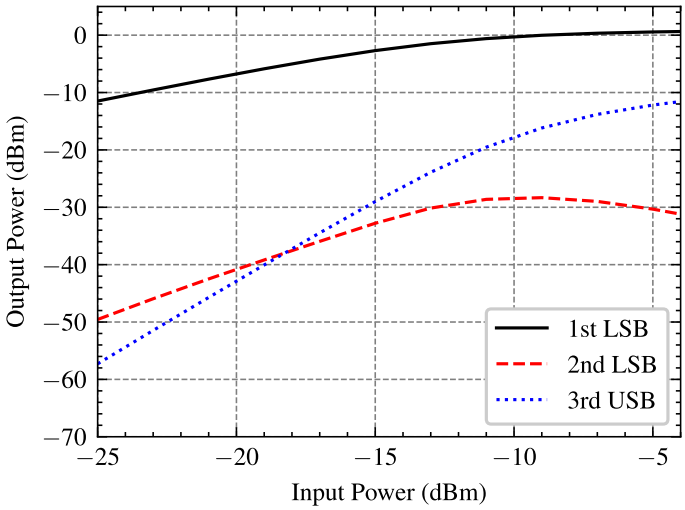

Figure 5.14: Simulated single mixer compression at 260 GHz with an IF frequency of 3 GHz with artificial mismatch. By introducing artifical mismatch the behavior of the measured compression can be achieved.

buffer amplifier which leads to different base-emitter voltages at the transconductance pair (compare upconversion mixer schematic in Chapter 3). As shown for this simulation, both odd mixing products remain untouched by the mismatch, however the 2^{nd} order harmonic is increased to similar levels as shown in the measurement (Fig. 5.12a).
The origin of this mismatch cannot be directly derived from the upconversion mixer layout or the PCB. While both the PCB and baseband routing on the TX will introduce common mode at the mixer's baseband input, additional process variations in the experimental technology cannot be excluded. In separate measurements which are not shown in this dissertation, the pull-up resistors of the input buffer of the TX were measured and showed a difference of 20 Ω depending on the position on the die.

For future upconversion mixer implementations, this effect should be minimized by reducing the possible influence of process variations. The measured second order harmonic distortion defined as

$$HD_2 = \frac{\text{Amplitude of second Harmonic}}{\text{Amplitude of Fundamental}} \tag{5.2}$$

The visible HD_2 will directly affect the communication link as its relationship to 2^{nd} order intermodulation is defined as:

$$IM_2 = 2HD_2. \tag{5.3}$$

It should be noted, that the presented measured large-signal compression for the single measurement is for optimized mixer biasing. It was found that the base-emitter voltage directly influences the observed HD_2. The presented compression measure-

ments are biased at the point where the achieved fundamental conversion gain is traded against decreased 2^{rd} order harmonic power.

As shown in the large-signal measurements of the single mixer in the TX (Fig. 5.12a & Fig. 5.12b), the output power generated by a single mixer is insufficient to compress the following power amplifier, as the measured power of the TX is lower than the saturated output power of the power amplifier in combination with the antenna-induced losses. The single sideband exciation of the TX here allows to operate both mixers simultaneously with their power ideally combining. This measurement will be explained in the following.

5.3.2 Single Sideband Measurement

Communication systems above 200 GHz generally operate in double sideband transmission. Double sideband transmission stems from the regular behavior of upconversion mixers operated with periodic signals (i.e. frequency translation). While double sideband transmission occupies larger bandwidths in the RF domain, the generation of single sideband signals in bandwidths in excess of tens of GHz becomes impossible as the required RF filters cannot be implemented on-chip.

For the total transmitted power, the entire transmitted power needs to be integrated over the observable bandwidth. When operating two mixers (I/Q) at the same time, three different scenarios can be created with allow for output power estimation.

- Both I and Q Mixer operate at different IF frequencies. Thereby, four fundamentally upconverted signals are generated. In addition, at least up to 8 further harmonic tones are generated (when only the first three harmonics of the baseband signal are considered). All these tones have to be integrated over the entire bandwidth.
- Both I and Q mixer operate at identical IF frequencies and the baseband signal is in-phase. This will generate two fundamentally upconverted signals. If the phase perfectly aligns, each tone will be 3dB higher than the tone generated by a single mixer. This difference will only be 3dB if the baseband is perfectly in-phase. For different phase relationships, the ratio will change between the USB and LSB.
- Both I and Q mixer operate at identical IF frequencies and the baseband signal is out-of-phase. Thereby, only either USB or LSB will be generated. And thus, the majority of the output power is in one tone only.

The last case simplifies the measurement of the maximum output power of a transmitter as only either the USB or LSB tone holds the majority of the output power.

This also allows for better comparison of the compression behavior of the transmitter with the power amplifier, as power amplifiers are typically only measured with a single tone applied.

The method described before for generating the single sideband signal is typically described as the phase-shift method or Hartley modulator. While this method can be used for low bandwidths or single tones, its application for broadband signals becomes nearly impossible as it requires broadband 90° generation while also compensating the additional group delay introduced by the individual components in the transmitter. Here, it should be noted that both I and Q Mixers are needed, whereas a communication system using a single mixer cannot generate a single sideband based on this approach. The other common method based on bandpass filtering needs to be implemented in the RF domain. Such bandpass filter requires a high stopband rejection and sharp passband edges. To achieve this behavior, a high filter order is needed which introduces additional losses in the transmission path which is not desired irrespective to the added implementation complexity. In general, this approach cannot be found in high-frequency communications systems.

For optical communications other methods for single sideband generation such as optical single sideband scheme (OSSB) or tandem single sideband (TSSB) exists, which cannot be replicated in communication using fully integrated circuits.

In the following, the math behind the phase-shift method will be briefly explained as it is needed to understand why and how measurement results can vary from ideal mathematical assumptions.

As the implemented transmitter has both I and Q Mixer, the phase-shift method can be applied. For the phase-shift method, we assume that the baseband signals I and Q are out-of-phase. Normally, the quadrature is solely generated by the LO. Thereby, the resulting upconverted signals for the I and Q channel respectively can be described as:

$$A_I \cos(\omega_m t) cos(\omega_c t) = \frac{1}{2}[\cos((\omega_c - \omega_m)t) + \cos((\omega_c + \omega_m)t)] \tag{5.4}$$

$$A_Q \sin(\omega_m t) sin(\omega_c t) = \frac{1}{2}[\cos((\omega_c - \omega_m)t) - \cos((\omega_c + \omega_m)t)]. \tag{5.5}$$

At the output of the upconversion mixers, the signals are combined using a differential Gysel power combiner. Therefore, the result of this combination can be expressed as :

$$LSBSignal: \frac{A_{I,LSB} + A_{Q,LSB}}{2} \cos((\omega_c - \omega_m)t) + \frac{A_{I,USB} - A_{Q,USB}}{2} \cos((\omega_c + \omega_m)t). \tag{5.6}$$

In this way, the LSB tone will be generated, while the USB tone is suppressed. Likewise, the LSB suppression and hence USB generation can be achieved by applying a negative 90 ° phase-shift to the baseband.

Under the ideal assumption, that both I and Q amplitudes as well as USB and LSB are symmetric, the resulting tone will have 6 dB more power in comparison to a tone generated by a single mixer.

In reality, this condition cannot be achieved. The IQ imbalance is mostly based on the IQ-generation and on-chip and was measured separately similar to the IQ imbalance measurement for the receiver. For this, one mixer was fed with a baseband signal while the other mixer is left in idle state. The difference in output power of each mixer then defines the IQ imbalance.

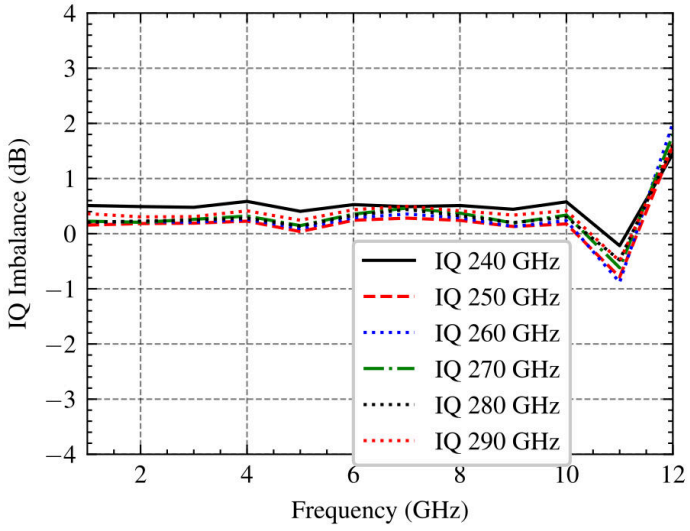

Figure 5.15: IQ imbalance of the TX for LO frequencies between 240 and 290 GHz in 10 GHz steps. For the TX, the IQ imbalance stays well below 1 dB for IF frequencies up to 10 GHz.

This IQ imbalance is around 0.4 dB for IF frequencies up to 10 GHz. Above 10 GHz, the influence of the packaging does not allow to maintain the IQ imbalance. The identical behavior of both TX's and RX's IQ imbalance above 10 GHz points to decreased isolation between the I and Q channel on the PCB. This decreased isolation however

cannot be directly attributed to a single component in the PCB, the first assumption is the connector match presented in Chapter 4 which showed that for frequencies >15 GHz reflections at the connector can be expected which may lead to incorrect IQ imbalance readings.

The influence of the sideband asymmetry on the single sideband generation can only be neglected for very low IF frequencies, where the termination of the mixer in both sidebands can be assumed identical. For higher IF frequencies in the GHz range, the asymmetry is generated by the mixer termination and gain variation of the following blocks over the observed frequency range. Based on this, the resulting CG derived from the single sideband measurement will differ from the ideal 6 dB while also having different behavior respective to the observed sideband.

The measured sideband asymmetry from the single mixer measurements for different IF frequencies at different LO frequencies is shown in Fig. 5.16. For an IF frequency of 1 GHz, this asymmetry is low up to 270 GHz, whereas the sideband asymmetry for the other IF frequencies is ± 2 dB for the different LO frequencies. While this is partially caused by the faulty de-embedding of the conversion gain of the OML module and the influence of the used broadband balun, a generally high sideband asymmetry is observed. Above 290 GHz this behavior is expected, as the power amplifier's bandwidth limit is reached with the gain decreasing rapidly. Thereby the LSB tones see a higher gain than the respective USB.

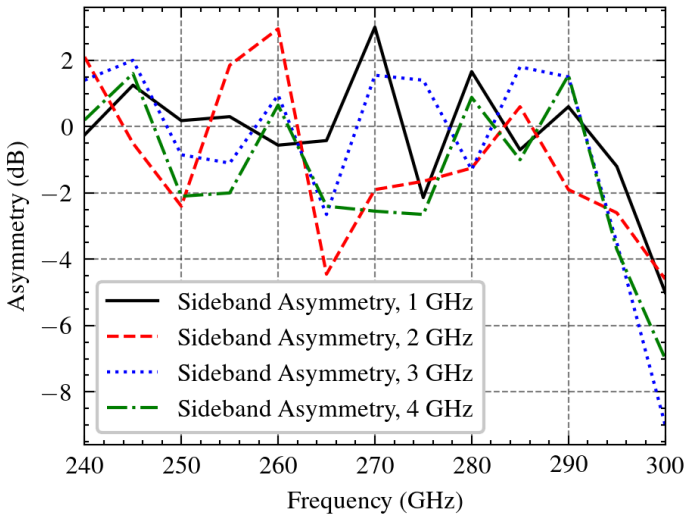

Figure 5.16: Sideband asymmetry derived from single mixer measurements with different IF frequencies. The different LO frequencies (see x-axis) show that the sideband asymmetry is chaotic and cannot be solely linked to the baseband routing which would predict identical sideband asymmetry for identical IF frequencies.

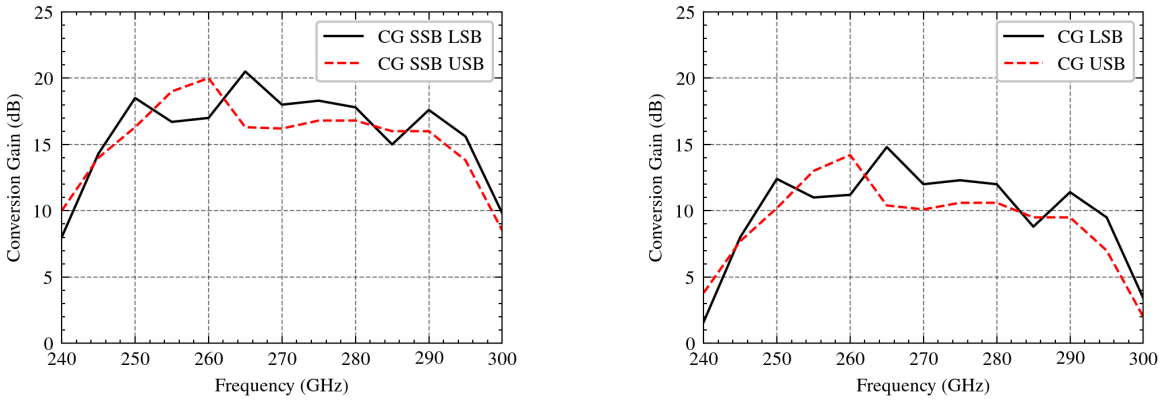

(a) SSB operation of the TX

(b) DSB operation of the TX

Figure 5.17: Conversion Gain with constant IF frequency of 2 GHz for DSB(single mixer) and SSB (both mixers + Hybrid) operation at different LO frequencies. The two operation modes show a difference of 6 dB as expected from the mathematical derivation.

This sideband asymmetry behavior (Fig. 5.16) is also visible when observing the conversion gain in the single sideband operation in both configurations. The sideband asymmetry creates a higher CG for the SSB USB at lower frequencies, while the SSB LSB shows an increased CG at higher frequencies as shown in Fig. 5.17a and 5.17b. The outlier at 285 GHz is also visible in the conversion gain of the SSB LSB measurement.

The measured conversion gain for both DSB and SSB operation show the expected difference of 6 dB due to the simultaneous operation of two mixers. In contrast to this, the saturated output power behavior is different for the two observed operation modes (Fig. 5.18b & 5.18a). The saturated output power is only increased by 4-5 dB between the single mixer and dual mixer operation, therefore it is assumed that the two mixers in combination with the power amplifier allow to slightly compress the power amplifier. This is mostly due to the soft compression behavior of a single mixer, as visible in the compression curves for single mixer measurement in comparison to the sharp compression displayed by the amplifier presented in Chapter 3. For the SSB measurement (Fig. 5.18a), the compression of the amplifier dominates while the mixers do not provide sufficient output power to reach full compression of the amplifier. This behavior is further confirmed as the total output power does not increase by 1 dB when supplying the amplifiers with a supply voltage of 4 V. Here, the impact of the decreased gain is more severe than the added voltage headroom.

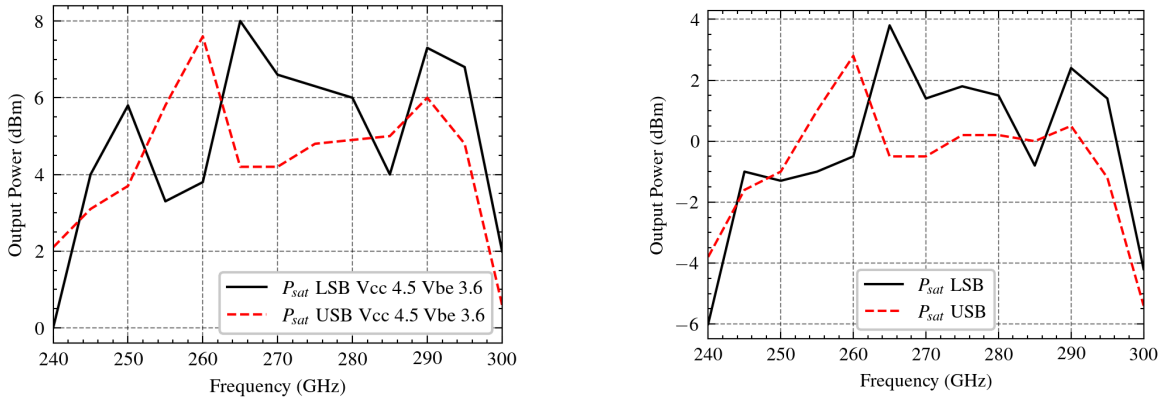

(a) SSB operation of the TX

(b) DSB operation of the TX

Figure 5.18: Saturated Output Power with constant IF frequency of 2 GHz for DSB(single mixer) and SSB (both mixers + Hybrid) operation at different LO frequencies.

For the overall performance of the transmitter, the total maximum output power as well as the resulting bandwidth is of highest interest. For this, the transmitter again was operated in SSB generation. Here, the phase shift was generated using an external broadband 90° Hybrid with a maximum bandwidth of 26.5 GHz. This frequency is also the upper limit of the used baluns for the differential baseband signal generation.

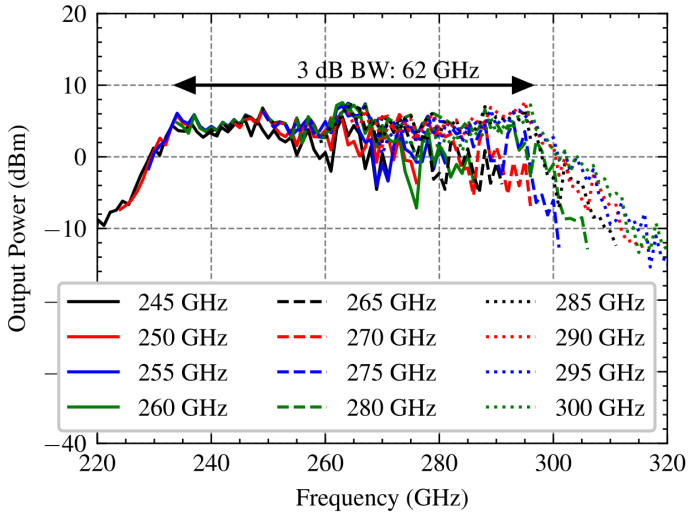

Figure 5.19: Saturated output power over frequency in SSB operation for different LO frequencies with increasing IF frequencies. Here, it can be seen that RF signals can be upconverted in a 3-dB bandwidth spanning from 234 GHz to 296 GHz.

Similar to the conversion gain over LO frequency for the RX (Fig. 5.6), the saturated output power for different LO frequencies is shown to derive the total potential RF bandwidth of the transmitter (Fig. 5.19). Here, a total saturated output power 3-dB bandwidth of 62 GHz can be observed spanning from 234 GHz to 296 GHz.

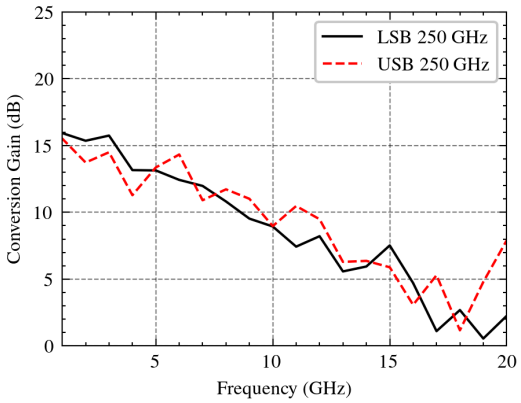

(a) Conversion gain of the TX for a LO frequency of 250 GHz.

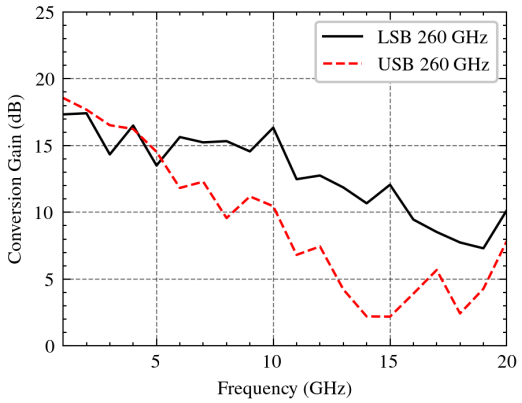

(b) Conversion gain of the TX for a LO frequency of 260 GHz.

Figure 5.20: Conversion gain of the TX at 250 and 260 GHz. For 250 GHz, the USB and LSB bandwidth is identical at aroud 8 GHz whereas the conversion gain at 260 GHz shows a high asymmetry with both USB abd LSB bandwidth reduced to 5 GHz respectively.

Compared to the measurement results of the used power amplifier, this shows a nearly identical bandwidth, with the frequency range lowered by 5 GHz.

Again, the actual IF/RF bandwidth cannot be read from this plot. For this, the Conversion Gain at 250 GHz and 260 GHz for varying IF frequency is shown (Fig. 5.20a and 5.20b).

As seen for a LO frequency of 250 GHz (Fig. 5.20a), the conversion gain of the transmitter has an equal bandwidth for both USB and LSB of about 8 GHz. However, for a LO frequency of 260 GHz (Fig. 5.20b), the sideband asymmetry is clearly visible and the IF bandwidth is reduced to 5 GHz for both sidebands. As this bandwidth reduction is dependent on the LO frequency, it is irrespective of the PCB induced bandwidth reduction which is in contrast to the bandwidth behavior of the RX.

As previously shown, the influence of the PCB can be compensated for the TX by applying high input power to the mixers, as the saturated output power is independent of the insertion loss in the baseband. This respective bandwidth can be seen in Fig. 5.21, where the total output power is shown for a LO frequency of 270 GHz both for the USB and LSB. Here, it can be seen that the bandwidth is extended, however, the total output power still flunctuates by 2 dB for the LSB over a frequency range of 20 GHz. In contrast to this, the USB shows a clear resonance at 15 GHz, which is related to the connector bandwidth on the PCB as shown in Chapter 4.

For the operation of the TX, the linear operation of the mixers is important. The input referred compression point shows the input power for which the conversion gain

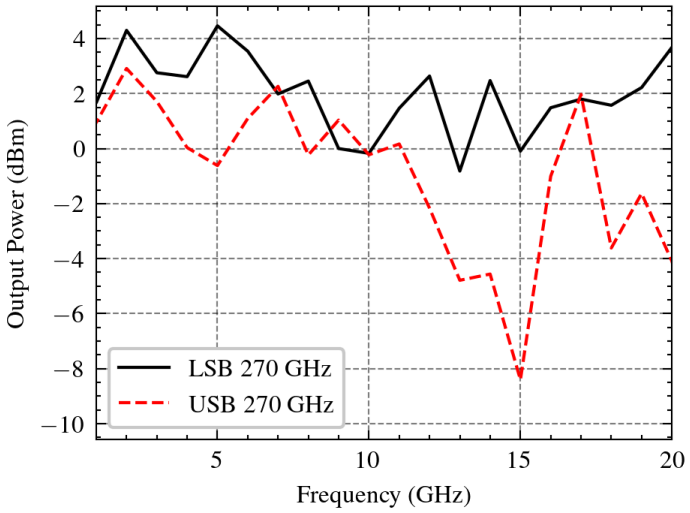

Figure 5.21: Saturated output power at 270 GHz for IF Sweeps in both directions. Again, it can be seen that the sideband asymmetry is visible for saturated output power.

will decrease by 1 dB, which is the typical metric for compression in linear circuits. This respective behavior for different LO frequencies is shown in Figure 5.22 for SSB operation of the mixer.

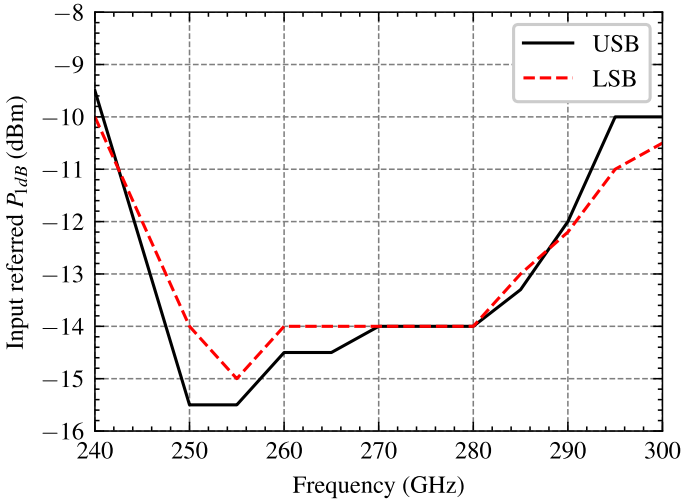

Figure 5.22: Input referred compression point of the transmitter for the different LO frequencies. In contrast to the output power, the input referred compression remains almost constant between 250 GHz and 280 GHz and does not strongly vary between the upper and lower sideband.

The input referred compression point is constant for LO frequencies ranging from 250 to 280 GHz. For increasing frequency, the mixers require additional input power to saturate which is due to the declining switching behavior of the upconversion mixer. This frequency behavior must be noted as it can directly influence the data rates for

LO frequencies above 290 GHz when the baseband power is insufficient to compress the mixers.

5.3.3 Harmonic Suppression

By using the single sideband operation, the harmonic suppression of the transmitter is measured for an IF frequency of 33 MHz. For this, not only the desired harmonic (×9) is observed but also the mixing products of the other undesired harmonics of the frequency multiplication stages namely 7^{th}, 8^{th}, 10^{th}, and 11^{th} harmonic. The resulting upconverted tones for constant IF and varying LO frequency can be seen in Fig. 5.23. The RF/LO 3-dB bandwidth spans from 243 to 296 GHz, which at the lower boundary clearly appears to be set by the LO generation, as the lower boundary is identical for TX, RX and the individual measurement, while the provided LO power is insufficient to drive the upconversion mixer above 295 GHz.

The suppression of the undesired upconverted SSB signals can be observed as well, this is related to the generated LO power of the different harmonics as shown in Chapter 3. In the transmitter a harmonic suppression to the neighbouring harmonics of at least 40 dB can be seen between 255 and 290 GHz. At the edges, the harmonic power increases rapidly as expected from the frequency multiplier stage measurement.

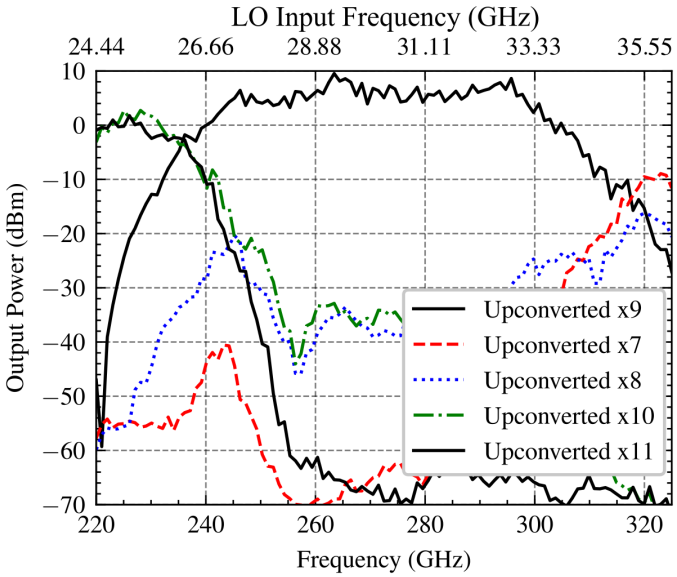

Figure 5.23: Upconverted SSB signals for an IF frequency of 33 MHz and varying LO frequency. Here, the 5 observed mixing products are shown. The RF/LO bandwidth is reduced starting from 243 to 296 GHz.

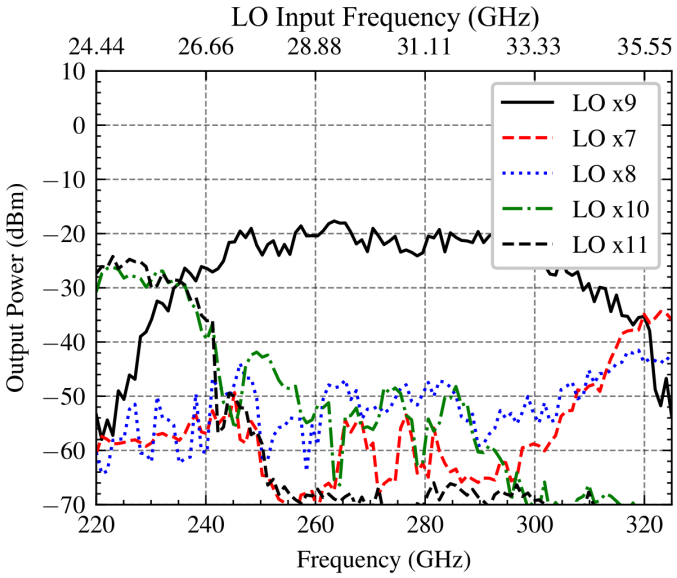

Figure 5.24: LO leakage of the different LO harmonics present in the TX. In comparison to the transmitted upconverted output power, it can be seen that the LO leakage is suppressed by about 25 dB with the other harmonics further suppressed.

In addition, the LO leakage of the different generated LO harmonics can also be measured as it is transmitted by the TX as well. It should be noted that these measurements are conducted for high IF power levels, which increases the LO suppression, thereby the fundamental LO is suppressed by 25 dB, while the other harmonics are further suppressed down to almost 50 dB from 240 to 310 GHz. The high conversion gain presented by the 10^{th}, and 11^{th} at the lower band edge is due to the amplification of these harmonics by the power amplifier, as the 10^{th}, and 11^{th} upconversion product is placed inside the amplifier's 3-dB bandwidth.

For single mixer operation, the LO leakage will always be much worse than the presented LO leakage (Fig. 5.23) as the unused mixer cannot be turned off and thus acts as a degenerated common-emitter amplifier for the applied LO signal. If one mixer is turned off i.e. the biasing is not provided both the differential coupled-line 90° Hybrid as well as the Gysel power combiner will not be terminated correctly and will face asymmetry. To avoid this, both upconversion mixers need to be biased at the same time independent of the operation.

5.3.4 Group Delay

The single sideband characterization of the transmitter can also be used to measure the group delay difference between the two channels. For this, the Tektronix DPO70000 oscilloscope is used to first align the differential I and Q baseband input signal at mul-

tiple frequencies (1, 5, 10, 15 GHz). Instead of using the broadband Balun to create two orthogonal differential inputs, the phase control of the Anapico signal generator is used. The two orthogonal I and Q signals are applied to the transmitter. While the initial phase setting creates a single sideband response, this response can further be improved by adjusting the phase difference between I and Q to achieve maximum sideband suppression.

In this measurement, the sideband suppression is the ideal indicator as a clear maximum can be found in comparison to the power in the desired sideband which will vary by fractions of a dB. The resulting phase difference between the maximum suppression and the initial state is then divided by the frequency, resulting in the measured group delay needed for sideband suppression. This group delay is frequency independent and by measuring it at multiple frequencies, it could be shown that the group delay difference varies between 5 and 5.33 ps. This group delay difference can later be used to precompensate the signal generators in the communication link measurements in Chapter 6.

5.4 Power Consumption

Given the identical LO signal generation in both the transmitter and receiver, the power consumption is nearly identical in this section. All power amplifiers in the LO generation are biased identically with a supply voltage of 3 V drawing 130 mA each, as shown in [own1]. The buffer amplifier and second tripler biasing points are identical in the transmitter and receiver, while the first tripler in the transmitter with a supply voltage of 3.5 V is biased higher than in the receiver (2.6 V). The transmitter profits from the increased supply in the first tripler as it slightly improves its output power and thus improves CG and harmonic rejection of the transmitter. In the receiver, this effect could not be reproduced as the conversion gain does not further increase with higher LO driving power, the downconversion of the other harmonics can also not be improved with higher supply voltages. Thereby, the receiver input tripler is biased lower for better efficiency.

As described in Chapter 3, the downconversion mixer and TIA in the receiver share the same DC supply of 4 V and draws around 18 mA when no LO power is applied. The power consumption of the individual parts cannot be isolated. The second stage of the TIA and its output buffer share the same supply voltage of 3 V while drawing 50 mA. Thereby, the total DC consumption of the receiver is 1.44 W with the LO generation consuming 1 W that is equal to 70 % of the total power consumption. In the transmitter, the upconversion mixers in each polarization consume 50 mW drawing from

a 4 V supply, whereas the baseband buffer consumes additional 9 mA with a supply voltage of 2.4 V. The transmitter further includes RF power amplifiers for each polarization. Therefore, the total power consumption of the transmitter is 1.977 W. The majority of the power consumption here is given by the additional RF power amplifiers.

5.5 Summary and Conclusion

In this chapter, the individual RF performance of both RX and TX was shown. For the antenna it was shown, that the difference between the RX and TX is minimal, which is expected as the difference in the measured directivity is only introduced by assembly inaccuracy and the used measurement method. Both RX and TX have a Directivity between 23 dBi and 24.5 dBi over the observed frequency band.
This measured directivity is needed to calculate the expected free-space-loss which is then de-embedded from the measurements of the RX and TX.

For the RX, a total RF/LO bandwidth spanning from 243 to 305 GHz was measured, which corresponds to the measured 3-dB bandwidth of the frequency multiplication stages presented in Chapter 3. The IF bandwidth is symmetric for both USB and LSB with 8 GHz for the majority of the observed LO frequencies. This bandwidth is lower than the simulated bandwidth both for the on-chip structures as well as the coupled lines on the PCB. It is expected that the connector in combination with the surface finish on the used PCB contributes to this additional bandwidth reduction.

The RX presents a single sideband conversion gain of 10 dB for LO frequencies from 250 to 305 GHz as shown in Table 5.1. With its noise figure below 14 dB between 260 and 310 GHz, the implemented RX presents a succesful implementation of a broadband receiver capable of operating at LO frequencies up to 305 GHz with its bandwidth currently limited by the PCB implementation.

The TX has a total RF/LO bandwidth of 53 GHz (243 GHz to 296 GHz), which is identical to the total bandwidth of the amplifier but tuned to slightly lower frequencies. Thereby, also the respective bandwidths of RX and TX overlap from 243 to 296 GHz, equal to a total bandwidth of 53 GHz for the link based on the RF performance. The transmitter has an input referred compression point of -14 dBm at 250 GHz, which increases to -10.5 dBm with increasing frequency due to the decreased switching performance of the upconversion mixer. When both mixers are run concurrently and generate a single sideband, a maximum output power of 8 dBm is reached around 262 GHz.

Table 5.2: Receiver operating above 200 GHz in Silicon.

Ref	Technology	Frequency (GHz)	CG (dB)	IF BW (GHz)	SSB NF (dB)	P_{DC} (W)	Chipsize (mm^2)
[98]	65nm CMOS	240	25	16	15	0.26	2
[99]	55nm SiGe	240	23	54	24.5	0.86	1.84
[15]	40nm CMOS	290	-19.5	27	26.5	0.65	3.15
[16]	40nm CMOS	265.58	-	20	22.9	0.88	10.93
[22] [1]	130nm SiGe	280	25	40	18.2	0.38	1.12
[95]	130nm SiGe	240	21	9	9.5	1	1.522
[23]	130nm SiGe	275	21.4	30	22.3	0.44	1.418
		275	27.5	30	20.1	0.49	2.03
This Work	130nm SiGe	243-305	10	8	≤ 14	1.44	5.12

[1] Not direct-conversion

It was shown that the output power of the two mixers is insufficent to fully compress the power amplifier as the output power remained constant for varying collector voltages of the power amplifier. Thereby, the power combining using the Gysel power combiner (Chapter 3) introduces too much loss for full saturation.

The IF bandwidth of the TX is limited to 8 GHz at 250 GHz which is similar to the RX measurements. Again, due to this similarity the PCB introduced insertion loss appears to limit the bandwidth. For other LO frequencies, a sideband asymmetry was visible which stems from an RF asymmetry as the upconversion mixer seems to be tuned to lower frequencies.

For lower frequencies around 240 GHz, it is clear that the generated LO power is insufficient in the receiver to provide enough conversion gain in the mixer. In the transmitter, the combination of both I and Q mixer, as shown in the SSB measurement, is not able to saturate the RF amplifier. In the amplifier measurements as presented in Chapter 3, the RF amplifier is able to generate up to 9 dBm, this power level cannot be reached even when taking the antenna losses into account.

Table 5.3: Transmitter operating above 200 GHz in Silicon.

Ref	Technology	Frequency (GHz)	P_{out} (dBm)	IF BW (GHz)	P_{DC} (W)	Chipsize (mm^2)
[100][1]	130nm SiGe	220	8.5	-	0.64	-
[20]	130nm SiGe	240	-0.8	17	0.38	4.3
[101]	130nm SiGe	220	4.8	-	0.9	2.8
[102]	40nm CMOS	300	-5.5	-	1.4	5.188
[103]	65nm CMOS	240	0	-	0.22	2
[95]	130nm SiGe	240	8.5	10	0.96	1.614
[104]	130nm SiGe	290	-4.1	15	0.3	–
This Work	130nm SiGe	243-296	8	8	1.98	5.53

[1] Sliding IF

In Table 5.2, the state-of-the-art of receivers operating above 200 GHz in silicon is given. The here presented receiver reaches the highest LO frequency for silicon-integrated receivers. In addition, its single sideband noise figure is better than the state-of-the-art by a wide margin when taking the operating frequency into account. As shown in this chapter, the IF bandwidth of the receiver is low due to the baseband routing both on-chip and on the PCB. In addition, due to implementation of a dual-polarization receiver, it takes up a large area and consumes the highest DC power due to the doubled amount of power amplifiers in the LO generation path.

The state-of-the-art for silicon-based transmitters operating above 200 GHz is shown in Table 5.3. In general, it can be seen, that transmitter implementations are far less reported which again is due to the low output power. This is also reflected by the low carrier frequencies in the Table. For the relevant frequency range above 250 GHz, the presented transmitter has the highest output power. As expected, the IF bandwidth is low in comparison to other publications, which is due to the PCB. Both power consumption and area are high since both polarizations need to be biased at the same time.

Chapter 6

Back-to-Back Communication

The Back-to-Back Measurements of the 300 GHz transmitter and receiver are discussed in this chapter. To achieve this, both the transmitter and receiver are mounted along a rail in a line-of-sight configuration at a distance of 60 cm, as shown in Figure 6.1.

The receiver is mounted on an electrically adjustable cylindrical positioner, which has also been used in the antenna directivity measurements. The transmitter is mounted on a movable x-y-z stage with an additional gyrometer for minor adjustments in ϕ and Θ. The two modules are aligned by finding the maximum transmitted power. Additionally, the receiver is turned along its propagation axis to ensure alignment in both ϕ and Θ.

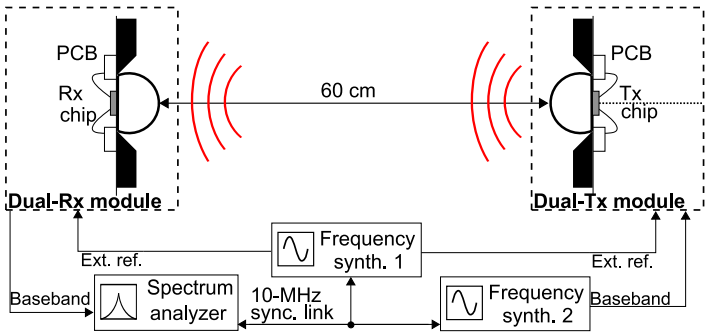

Figure 6.1: Setup of the communication setup in a distance of 60 cm. The RX and TX are first aligned in close distance to each other before moving them to the measurement distance.

In this setup, first the link RF characterization is done to determine the 6-dB bandwidth of the link, before modulated data is sent through the link.

During the characterization process of the transmitter, the I mixer in one polarization broke in an unexpected ESD event which eventually stopped drawing current. Due to the completed full RF characterization of the transmitter, the communication measurements were concluded with the characterized transmitter. Therefore, the following measurements in this chapter only reflect the performance of a single polarization and thus describe the inherent potential of the designed building blocks (Chapter 3) for future communication, but do not completely reflect the total link performance of the designed TX and RX chipsets.

It should be noted that the used transistor technology is still in a development stage, with the transistors not only presenting performance variations but also a lower yield in comparison to e.g. IHP SG13G2. An exchange of the transmitters would have required an additional full RF characterization which was deemed too lengthy at this point of the dissertation.

6.1 RF Characterization

For the initial RF characterization of the link, unmodulated sine waves are fed into one of the I/Q mixers of the transmitter and then read out at the IF output of either I or Q at the receiver. As both input and output are differential external baluns are used to generate the differential input signal for the transmitter and to combine the differential output of the receiver.

The resulting normalized gain can be seen in Fig. 6.2. In contrast to the individual transmitter and receiver measurement, the 6-dB bandwidth is of interest, as it is the combination of the individual 3-dB bandwidths. The back-to-back measurement shows a minimum 6-dB bandwidth of 6 GHz for an LO frequency of 240 GHz.

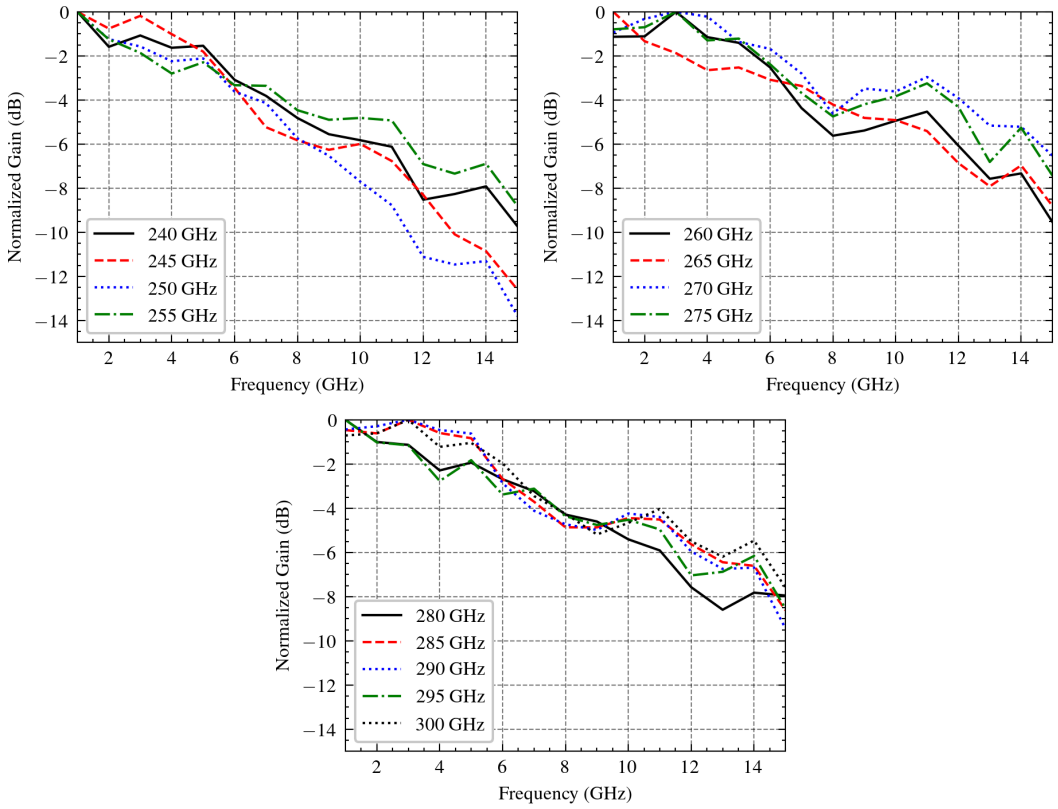

Figure 6.2: Normalized gain for different LO frequencies. As gain is measured in a back-to-back configuration, the 6-dB bandwidth is evaluated, this bandwidth is between 11 and 13 GHz for most LO frequencies.

For LO frequencies above 250 GHz, the measured baseband 6-dB bandwidth of the link ranges from 11 to 13 GHz.

In comparison to the individual RF measurements in Chapter 5, this bandwidth is 3 GHz higher than the expected 8 GHz that was shown for both RX and TX. In the link RF measurement, the individual bandwidth of the LSB and USB is not measured, as the TX transmits a double sideband signal, which is then downconverted by the RX. The measured raw power in the measurement aligns with the full link budget of the presented link (Fig. 6.1).

6.2 Link Measurements

The setup used for measuring data rates is shown in Fig. 6.3. For the generation of the modulated broadband baseband signals, a pair of Tektronix AWG7000B arbitrary wave generators (AWG) with a sampling rate of 50 GS/s are used. Here, pseudo-random bit sequences of order 7 with a stream length of $2^9 - 1$ were generated for the different used modulation schemes. Furthermore, a root raised-cosine filter with an

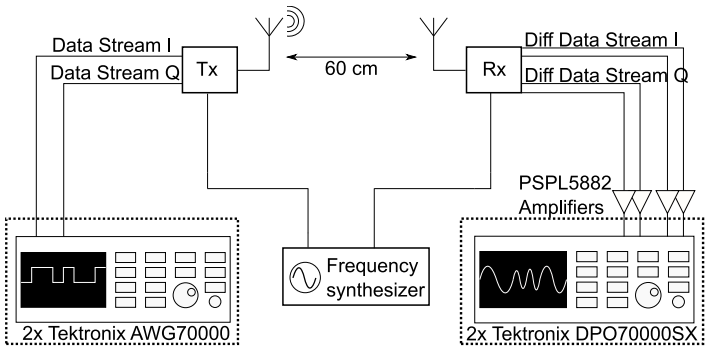

Figure 6.3: Setup of the communication measurement in a distance of 60 cm. Arbitrary Wave Generators are used for baseband generation, Demodulation is done by the oscilloscopes connected to the receiver baseband outputs.

α of 0.5 to 0.7 was applied for the chosen modulation schemes to further reduce the effective bandwidth of the baseband signal.

On the RX side, the downconverted signal is demodulated by two Tektronix DPO77002SX high-speed oscilloscopes with a sampling rate of 100 GS/s. The oscilloscopes include software for demodulation of the captured timestreams which allows to analyze EVM, constellation, and eye diagram in real-time and also handles the clock recovery. For quadrature modulation schemes, it also gives feedback on the gain and phase imbalance which is then adjusted on the transmit side by changing the internal delay and amplitude difference between the two AWGs.

For broadband communication, the measurement setup also requires multiple pairs of phase-matched cables to ensure that at least the differential signals can maintain their differential operation up until the inputs/outputs of the PCB. On the TX side, the losses of the cables and used DC blocks are compensated by internal pre-calibration of the signal generation path.

The communication system is measured first using phase-shift keying modulation. For this measurement, the ADC of the oscilloscopes should ideally be saturated. Thereby potential amplitude errors can be eliminated. In a phase-shift keying communications system, this can be achieved by limiting amplifiers in the RF path and baseband path. In the presented communications system, additional external broadband amplifiers are connected at the output of the RX as shown in Fig. 6.3.

On the TX side, it has to be noted that the power spectral density of the generated signal will remain constant for all symbol rates, which means that the power will be spread over the entire spectrum. Thereby, with increasing symbol rate less and less power is concentrated in the low-frequency part of the spectrum (below 5 GHz). It is expected that the influence of the PCB will become more severe with increasing bandwidth, which will result in additional data rate limitations.

The arbitrary wave generators have a maximum differential peak-to-peak voltage of 500 mV which will be applied to the differential 100 Ω provided by the mixer inputs. This is equal to a maximum rms power of 0.97 dBm, which - for a single tone -is sufficient to compress the mixer input as shown in Chapter 5.

For BPSK which makes use of only one mixer in the transmitter and receiver respectively, a maximum data rate of 30 Gbit/s can be achieved for LO frequencies between 260 GHz and 280 GHz as shown in Fig. 6.4. Given the title of the dissertation, it can be seen that data rates up to 20 Gbit/s are possible for a LO frequency of 300 GHz. For higher data rates, this immediately suffers from the reduced bandwidth and SNR at this LO frequency.

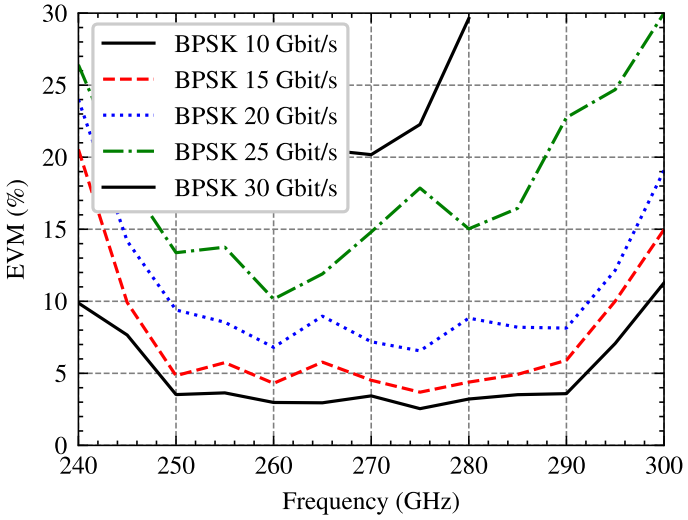

Figure 6.4: EVM for BPSK modulation at different LO frequencies and data rates. While 25 Gbit/s can be achieved for every LO frequency, the maximum BPSK data rate of 30 Gbit/s is only available for LO frequencies between 255 GHz and 280 GHz.

For data rates up to 20 Gbit/s, it can be seen that the EVM only increases by 2-3% for every additional 5 Gbit/s. However, starting with 25 Gbit/s, the EVM rapidly increases. Here, it appears that the required bandwidth cannot be achieved. Therefore, 30 Gbit/s is also only possible in the center of the band, where the RF power amplifier allows for full amplification of the generated double sideband signal.

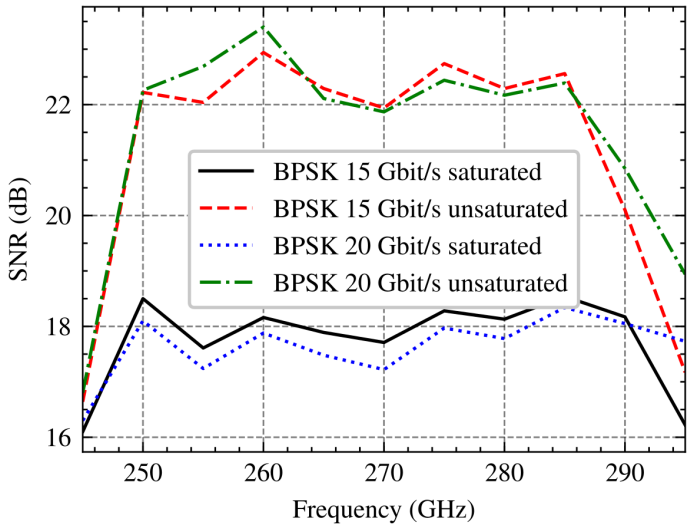

Figure 6.5: SNR for BPSK modulation at different LO frequencies and data rates (15 Gbit/s and 20 Gbit/s). It is visible that the SNR limits the transmission at the band edges, while the center of the band shows good alignment between saturation and unsaturated transmission.

As previously described, the voltage range at the oscilloscopes' inputs is adjusted to saturate the ADCs in the oscilloscopes. However, by increasing the voltage range, the actual SNR of the link can be calculated as shown in Fig. 6.5. This is here shown for 15 Gbit/s and 20 Gbit/s in the BPSK transmission. It can be seen that the input compression of the oscilloscopes limits the perceived link SNR by up to 3 dB at 260 GHz. However, even with compressed input the SNR is above 17 dB from 250 to 290 GHz. At the edges of the band, the available link SNR decreases rapidly, which is directly linked to the increased EVM for these LO frequencies (Fig. 6.4), thereby it can be assumed that the transmission at the band edges is SNR limited and can thereby not be majorly improved.

In the eye diagram, phase distortion is visible at every observed data rate. the eye shape is not ideal. For the desired states, the amplitude is set by the saturation of the ADC. However, in the transition region between these states, multiple lines are visible (Fig. 6.6). This behavior is caused by frequency jitter as explained in Chapter 2. Similarly, the Demodulator in the oscilloscopes constantly calculates the frequency offset that is at least 100 kHz in the measurement and increases up to 1 MHz for the maximum data rate.

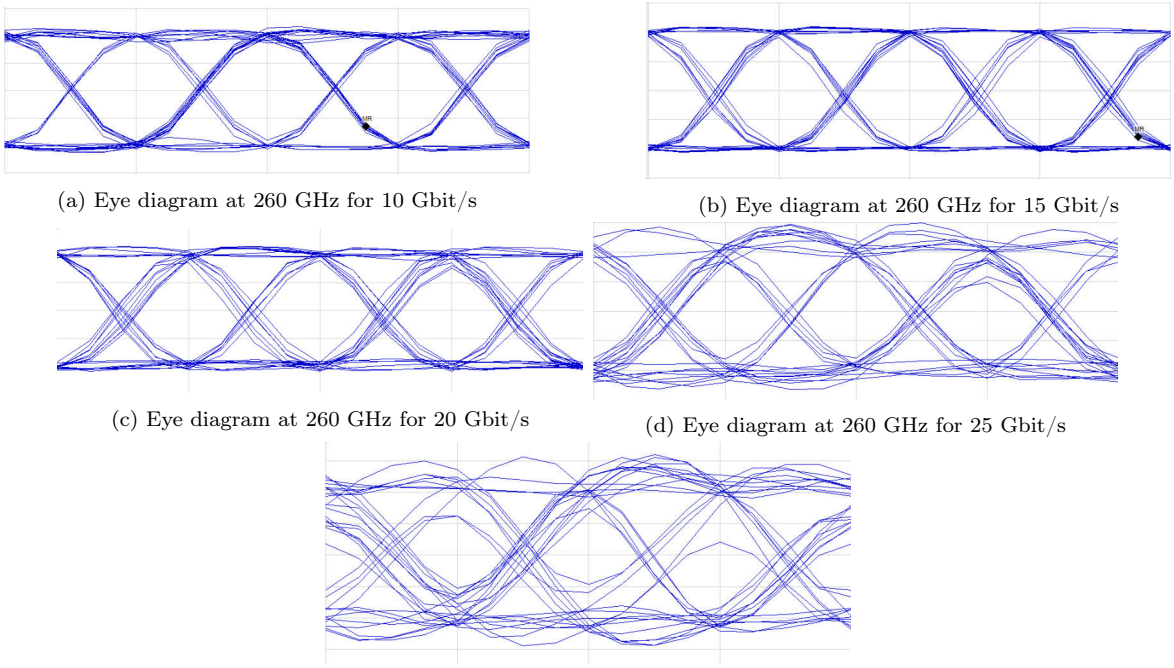

(a) Eye diagram at 260 GHz for 10 Gbit/s

(b) Eye diagram at 260 GHz for 15 Gbit/s

(c) Eye diagram at 260 GHz for 20 Gbit/s

(d) Eye diagram at 260 GHz for 25 Gbit/s

(e) Eye diagram at 260 GHz for 30 Gbit/s

Figure 6.6: Measured eye diagram for a LO frequency of 260 GHz at different data rates. Even for low data rates, a phase jitter is visible which further increases with data rate. Starting from 25 Gbit/s, additional amplitude distortion is visible in the overshoot. For 30 Gbit/s, the eye opening is barely visible and affected by the noise in the link.

By applying QPSK modulated signals to the transmitter, both I and Q mixers on the transmit and receive side are used simultaneously. This leads to an increased data rate for identical symbol rates. Ideally the EVM for QPSK modulation should be identical to BPSK modulation with the same symbol rate, as the two data streams (I and Q) should transmit independently and not interfer with each other.

This is the case for symbol rates of 10 and 15 Gbaud/s, as shown in Fig. 6.7a and 6.7b. For LO frequencies up to 270 GHz, the relationship between BPSK and QPSK is maintained. For the QPSK with a data rate of 30 Gbit/s, the EVM increases above 270 GHz. This is possibly related to the IQ imbalance in the RX which was shown to increase with LO frequency. For a symbol rate of 20 Gbaud/s, which corresponds to a data rate of 40 GHz in QPSK (Fig. 6.7c), the EVM for QPSK is much higher for QPSK in comparison to the respective BPSK modulation. This data rate also presents the upper limit of the data rate that can be demodulated for the presented communication link.

The EVM deterioration here is caused by two effects. For a symbol rate of 20 Gbaud/s, the corresponding baseband bandwidth is 20 GHz (considering no pulse shaping). As shown in Fig. 6.2, this exceeds the measured 6-dB bandwidth of the link (max. 13 GHz). While this bandwidth limitation is not too severe for the BPSK modulation, for the recombination of two independent I/Q streams, this presents a hard boundary.

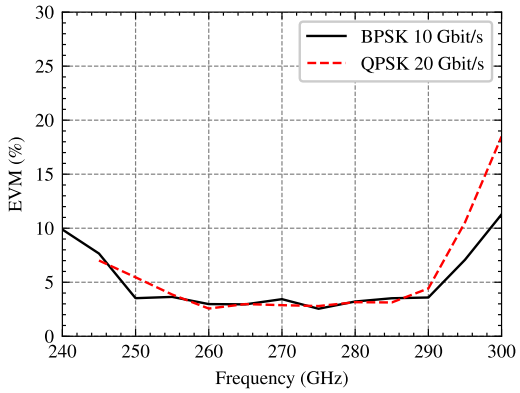

(a) EVM over LO frequency for a symbol rate of 10 Gbaud/s

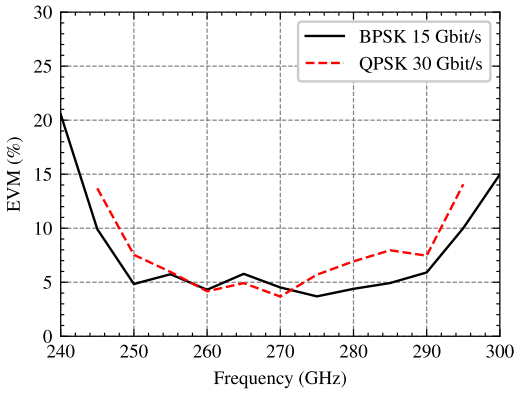

(b) EVM over LO frequency for a symbol rate of 15 Gbaud/s

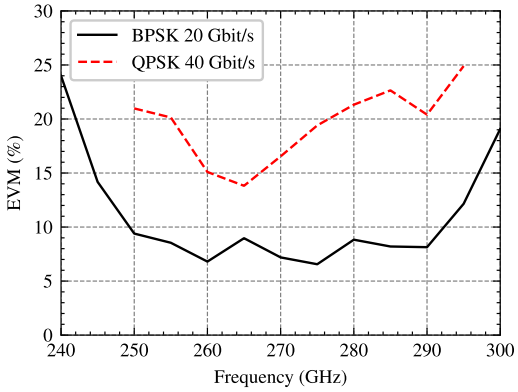

(c) EVM over LO frequency for a symbol rate of 20 Gbaud/s

Figure 6.7: EVM over LO frequency for different symbol rates in QPSK and BPSK. For a symbol rate of 10 Gbaud/s, the EVM is identical for both QPSK and BPSK. For higher symbol rates, these increasingly differ.

Similarly, the IQ imbalance of TX and RX in the individual measurement (Chapter 5) was shown to rapidly increase for IF frequencies above 10 GHz.

Thereby, a isolation between the two orthogonal baseband signals cannot be maintained, leading to an additional contribution to the total EVM in the QPSK modulation.

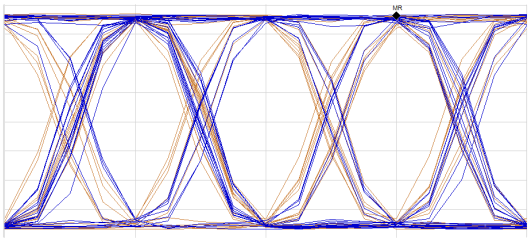

(a) Eye Diagram at 260 GHz for 20 Gbit/s

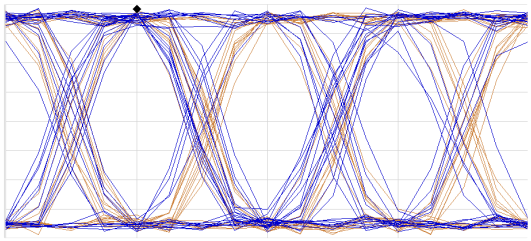

(b) Eye diagram at 260 GHz for 30 Gbit/s

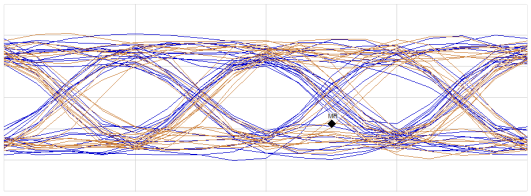

(c) Eye diagram at 260 GHz for 40 Gbit/s

Figure 6.8: Measured eye diagram for a LO frequency of 260 GHz at different data rates in QPSK modulation. Even for low data rates, a phase jitter is visible which further increases with data rate.

The respective eye diagrams for the QPSK modulation at 260 GHz is shown in Fig. 6.8. For all data rates, a clear eye opening is visible, while the jitter shown for BPSK Modulation (Fig. 6.8) is here present for both data streams and therefore, is increased for the total demodulation.

As previously described, the receiver output is amplified with additional external amplifiers to increase the received power at the oscilloscope's input. For data rates of 20 Gbit/s and 30 Gbit/s, this operation resulted in the shown eye diagrams (Fig. 6.8a and 6.8b). However, when further increasing the data rate to 40 Gbit/s, this was not possible using the external amplifiers. For this data rate, the frequency jitter was highly increased prohibiting the frequency locking of the two channels.

This effect was also visible in the constellation diagram as the four expected constellation diagrams continously splitted from each other, leading to perceived 8 possible bit combinations. As this effect is only visible for a short period of time and occurs randomly in the transmission, this effect is not visualized in this dissertation.

In this configuration, the oscilloscopes apparently receives multiple concurrent down-converted data streams that can be modulated. Due to the coexistence of multiple data streams, the demodulator is not able to discriminate between the desired and undesired data stream.

By removing the external amplifiers at the scope's input, the data rate could be increased to 40 Gbit/s. Due to the absence of the amplifiers however, the input of the input ADC in the oscilloscopes cannot be saturated. This leads to an unavoidable amplitude jitter as shown in Fig. 6.8c. For further increasing data rates, the eye

opening closes completely and no locking can be achieved.

The here described additional undesired constellation limits the presented communication link to phase-shift keying modulation. Due to the noise for the individual constellation points, 8PSK was not achievable in the measurement. Similarly, the phase jitter and additional constellation increases the total size of the constellation points, which prohibits the discrimination of the single points in 16-QAM modulation.

In the following, possible causes for this undesired second concurrent data stream are discussed.

6.3 Undesired Mixing

As previously described, the oscilloscopes receive multiple valid data streams from the RX where only one valid data stream is expected. This concurrent reception of multiple data streams leads to challenges for the carrier recovery in the demodulator of the oscilloscopes. While up- and downconversion of the data stream with different harmonics is possible, the presence of a second baseband signal generated by undesired harmonics is expected to be lower powered than the desired harmonic due to the high harmonic suppression as shown in Chapter 5.

The presence of such undesired additional basebands due to harmonic mixing would rather lead to an additional EVM deterioration as it represents additional correlated noise. As the demodulator at high data rates tries to lock to different data streams, the data streams propagating in the receiver appear to be on similar power levels.

Therefore, it is expected that this second baseband is generated by the same LO frequency with an additional delay in comparison to the desired LO signal of the receiver. Such a second, delayed LO signal can have multiple origins.

As shown in Chapter 4, the used connector sections in the implemented PCB have a limited bandwidth based on the measured return loss. While the LO feed return loss presented an apparent match at the design frequency, it cannot be excluded that the perceived match is caused by the high insertion loss or potential resonances in the PCB. Considering a non-ideal matching between the external LO signal generator and the interconnect between the PCB and the input frequency multiplier stage (Chapter 3), reflections and thereby standing waves will occur on the PCB LO feed structure.

This reflection could create a delayed, high powered second LO tone which is fed into the RX as well. As the frequency of the second tone is identical but shifted in phase, it can propagate through the entire RX similar to the desired LO signal and create an additional - delayed - version of the downconverted signal. Thereby, a second valid baseband signal is provided to the input of the oscilloscopes.

This effect could not be verified in the measurements, as it would require an ideal PCB implementation to negate this potential cause. Alternatively, a isolator could be used before at the RX LO feed to reduce the standing waves on the PCB. At the time of the measurement, no isolator/circulator was available in the laboratory at this frequency range. The here proposed cause is based on the signal propagation between 25 and 33 GHz. However, the additional undesired LO could also be generated in the RF domain between 240 and 300 GHz.

A RF generated second LO can have two origins. As the RX constantly receives two circular polarized waves, it cannot be excluded that a second undesired LO signal is coupled through the other unused polarization. This alone can have two origins. As described in Chapter 2, the two polarizations in an integrated chip will have a limited isolation due to fabrication and assembly inaccuracies, this limited isolation creates a cross-talk between the two polarizations which allows for the presence of a second delayed LO signal at the mixers. In addition, the second received LO leakage is not bound by propagation along the transmission lines in the RX but can potentially also propagate through the substrate and ground planes given insufficient DC decoupling.

Due to the system architecture, the two polarizations cannot be used independently as the second polarization must be at least biased to present to present the correct terminations for the passive structures in the antenna and LO generation path. During the measurement, multiple combinations were tested, where the individual amplifiers in both TX and RX were turned off to potentially block signals. This did not influence the previously described frequency locking problematic.

In contrast to previous MIMO implementations [56], the two polarizations in both the RX and TX share the same LO generation path. It cannot be excluded that the implemented splitting and isolation is sufficient to avoid the propagation of another delayed replica of the LO signal. This however cannot be fixed in the current design. For this, a single polarization RX/TX would be necessary.

6.4 Summary and Conclusion

As shown in this chapter, the presented TX and RX are able to achieve communication at LO frequencies up to 300 GHz. The presented link bandwidth shows an extended 6-dB IF bandwidth of up to 13 GHz for different LO frequencies in contrast to the expected 8 GHz derived from the individual TX and RX measurements in Chapter 5.

In the data rate measurements, it was shown that maximum data rates of 30 Gbit/s for BPSK and 40 Gbit/s for QPSK can be reached in the center of the frequency band (260-280 GHz for BPSK and 250-295 GHz for QPSK). The communication link is limited to phase-shift keying modulation schemes as the link exhibits high frequency jitter and thereby challenges to the carrier frequency recovery in the demodulator. This frequency jitter causes a high spread of the individual points in the constellation diagram and thereby does not allow concurrent amplitude and phase modulation in form of 16QAM.

In the measurements, the frequency locking was limited due to the presence of an additional valid data stream at the input of the oscilloscopes. This undesired data stream could not be eliminated. Multiple causes for this undesired operation are named in this chapter with potential solutions.

Overall, this communication link presents the first fundamentally operated communication link operating at LO frequencies up to 300 GHz in silicon, as shown in the state-of-the-art table (Tab. 6.1) for communication systems. In comparison to previous implementations in SiGe, the increased operating frequency is visible, which is only matched by CMOS communication links operating at a distance of ≤ 3 cm. As discussed in this chapter, the modulation scheme and total bandwidth is limited for the presented TX and RX. This leads to the reduced achieved data rates compared to [17], [21].

Table 6.1: Wireless links above 200 GHz in silicon technology

Ref	Technology	Frequency (GHz)	Modulation	Data-rate (Gbps)	P_{DC} (W)	Distance (cm)
[17]	130nm SiGe	190	BPSK	50	0.154	0.6
[18]	40nm CMOS	300	16-QAM	32	2.05	1
[19]	130nm SiGe	220-260	32-QAM	90	1.96/0.98	100
[20]	130nm SiGe	240	BPSK	25	0.95	15
[6]	130nm SiGe	220-255	16-QAM	100	1.41/0.55	100
[15]	40nm CMOS	290	16-QAM	32	0.65	1
[16]	40nm CMOS	265.58	16-QAM	80	0.89/0.88	3
[21]	130nm SiGe	235	QPSK	65	1.41/0.98	100
This Work	130nm SiGe	295 300	QPSK BPSK	40 20	1.98/1.44	60

Chapter 7

Conclusions and Outlook

7.1 Conclusion

This thesis describes the design, analysis and measurement of a comunication link operating at carrier frequencies up to 300 GHz, including the complete implementation of TX, RX and the broadband packaging. From Shannon's definition of the channel capacity, it is derived that increasing the bandwidth directly leads to increased channel capacity and thereby data rate. To realize respective RF frontend circuits maximizing the bandwidth while reducing circuit complexity, size and power consumption, a direct-conversion RX and its respective counterpart, the TX was designed. For higher bandwidth, it was also concluded that an increased carrier frequency is necessary that allows for broadband communication. Such potential channels are proposed by the respective IEEE standard [4] for THz communication.

As this generation of communication systems in silicon operates at unprecedented carrier frequencies, the respective components for the transmitter and receiver were designed using an advanced 0.13 µm SiGe BiCMOS technology. In Chapter 3, the required building blocks for both TX and RX were introduced. Here it was shown that especially for the RF components namely power amplifier and LO frequency multiplication stages, the operating frequencies could be increased above 300 GHz. Both circuits showed a 3-dB bandwidth >60 GHz, with the multiplication stages including the power amplifier having a bandwidth spanning from 239 GHz to 304 GHz, whereas the power amplifier alone covers the frequency range between 239 and 302 GHz.

In the individual RF characterizations of both TX and RX, it was shown that both provide a high RF/LO 3-dB bandwidth spanning from 243-305 GHz for the receiver and 243-295 GHz for the transmitter allowing for carrier frequency allocation in the entire band. For both TX and RX, an average IF bandwidth of 8 GHz for different LO frequencies was measured. As both TX and RX exhibit the same IF bandwidth it is concluded that this is contributed by the insertion loss generated by the PCB.

For the receiver, the measured single sideband noise figure was below 14 dB for the majority of the observed frequency range. This noise figure is similar to the noise figure seen in communications systems operating aroud 240 GHz, despite its increased carrier frequency. Thereby, it is expected that an amplifier-first implementation of an equivalent RX will not improve its performance.

In the transmitter, it was shown that the output power of the transmitter is limited by the upconversion mixers that cannot generate enough output power to saturate the following power amplifier. As the TX baseband input can be saturated for high input powers, the saturated RF bandwidth was extracted for different LO frequencies, which is >40 GHz for the majority of chosen LO frequencies. The upconverted bandwidth is larger than the RF/LO bandwidth, spanning from 235 to 297 GHz.

In the back-to-back link measurements, communication was shown for carrier frequencies up to 300 GHz. In the current setup, the link is limited to BPSK (up to 30 GBit/s) and QPSK (40 GBit/s). The main contributor of this modulation limit is the insufficient frequency locking capability in the modulator. In the observed measurement, another concurrent constellations appear to coexist with the demodulator constantly locking to either of the possible constellations. The contributor for this constellation was not found in the course of this dissertation.

It is assumed that the additional constellation is caused by an additional mixing with a parasitic LO tone which is either generated through reflections at the PCB to chip interface or inside the receiver. The on-chip parasitic LO tone cannot be isolated as both polarizations have to run concurrently to achieve symmetric termination of the passive structures. Therefore the propagation path of the second LO tone cannot be identified at this point. The following outlook proposes solutions for better link performance which should not be limited by the current modulation limit or bandwidth limitation.

The presented communication link is the first fundamentally driven communication link operating at 300 GHz in silicon with a maximum data rate of 20 Gbit/s in BPSK modulation.

7.2 Outlook

The thesis identifies several bottlenecks for broadband communication. Some limitations can be easily removed with minimal effort and time, while others are a result of circuit implementation and cannot be easily solved. The potential improvements and their expected impact will be discussed in the following sections, based on the anticipated time schedule for their resolution.

7.2.1 Short-term outlook

Chapter 4 showed that broadband, high-frequency PCB design (up to 30 GHz) becomes challenging when faced with a high interconnect density as presented by the implemented transmitter and receiver. This dissertation revealed that the use of coupled lines for size reduction of broadband baseband connections on the PCB, in combination with the surface finish required for gold bonding, results in additional insertion loss that was not anticipated during the initial design process. Chapter 4 introduces DIG as a potential surface finish removing the less conductive, ferromagnetic Nickel from the copper traces. Additional simulations and measurements for transmission lines demonstrate that it is possible to avoid the sharp roll-off that is visible in the RF and link measurements presented in this dissertation.

Additionally, the improper connector implementation caused problems in both the RF characterization and link measurements. For this, again Chapter 4 offers an improved version of this connector section, under the condition that these can be fabricated by the PCB manufacturer which was not the case for the used PCB in the presented measurements.

By removing potential constraints, it is possible to achieve a 'transparent' packaging that reflects only the performance of the integrated circuits in the measurement. Such a 'transparent' packaging is needed to isolate the problems shown in Chapter 6, which has limited the frequency locking of the transmitter and receiver in the link measurement.

To address the frequency locking issues mentioned earlier, a short-term solution is to apply digital high-pass filters to the received signals in the oscilloscopes. The perceived frequency locking manifests itself similarly to phase noise in LO generation. By applying a high-pass filter before the demodulation, the 'noisy' LO reference that is centered around 0 Hz can be removed. This was already applied for free-running TX and RX, where the LO frequency and phase offset creates phase noise which - again - prohibits frequency locking.

The used Tektronix oscilloscopes include capabilities to apply Matlab generated functions on the received traces, however during the measurement of the link, this functionality was unavailable due to software version incompatibility.

The used DC blocks in the measurement setup at the mixers' inputs and outputs present a high-pass behavior. In principle, the 'noisy' LO input reference can also be removed by selecting the correct cut-off frequency of this filter, however the cut-off frequency of the available DC blocks was too low to remove the LO disturbance.

7.2.2 Long-term outlook

For PCB design, the turnaround time from re-design over fabrication to delivery and assembly is relatively short (months) and reasonably priced. For integrated circuits however, the time scale between re-design, tapeout and delivery plus the required assembly can take close to a year. With the total silicon area of 10 mm^2, the projected costs for a redesign are about 8000 € per 1 mm^2 in a SiGe BiCMOS technology process. Therefore, changes to the circuit and layout are not readily available and can be tested rapidly.

As shown in the simulations of the implemented TIA in Chapter 3, the TIA's performance suffers from multiple effects, the design of the feedback-loop reduced the power-handling as well as the achievable bandwidth for high LO power levels. Chapter 3 presents an improved TIA design which is fully layouted and simulated using 3D-solvers, in this design the previous 'large-signal' RF bandwidth of 16 GHz was extended to 66 GHz. In addition, the routing of the baseband outputs in the RX was improved to reduce the insertion loss and phase difference between the I and Q paths. The simulated RF bandwidth matches the 3-dB bandwidth of the RF power amplifier (63 GHz).

Both RF power amplifier and the improved TIA show an RF bandwidth that is at least twice as high as communication chipset implementations operating at 240 GHz [21]. In an ideal communication link that is only dependent on the available bandwidth, the expected data rate could directly be improved by a factor of 2 in comparison to [6], which would again be theoretically doubled for ideal dual-polarized operation given perfect isolation between the polarizations. In addition, the baseband bandwidth of the proposed improved TIA matches the input bandwidth of the used Tektronix oscilloscopes and therefore would reach the limit of available measurment equipment.

In general, both the frequency multiplication stages as well as the power amplifier are limited to frequencies close to 300 GHz. For the proposed upper limit of 325 GHz [4], the frequency response of these circuits has to be improved. The measurements of the power amplifier (Chapter 3) showed a gain roll-off starting at 280 GHz which was larger than expected from the simulations. Similar behaviour was seen for other circuits in this technology [32]. Here, the validity of the provided transistor models at these frequencies can be improved or if the gain roll-off must be recovered by pre-compensation in the transformer design.

Both TX and RX showed decreasing conversion gain with increasing frequency, while this can partially be contributed to the decreased switching capabilites of the used transistors, the output power generated by the frequency multiplier stages was not sufficently high enough to saturate the following power amplifier and therefore also not the switching quads of TX and RX. Due to the dual-polarized design of the transmitter and receiver, the generated LO signal is split immediately after the last tripler. Therefore, additional loss is added due to the required power-combiner. For single-polarization TX and RX, this problem should be non existent.

Similar to the insufficient LO power, the RF characterization of the transmitter showed that the simultaneous operation of both mixers does not generate enough power to saturate the RF power amplifier. In the presented design, the upconverted I and Q passband signals were combined using a Gysel power combiner (Chapter 3). The added insertion loss limits the input power at the power amplifier. In the link measurements, the effect of the added isolation from the Gysel power combiner could not be extracted. I/Q mixers using current combining could reduce the added insertion loss and thereby potentially saturate the power amplifiers allowing to access the extended saturated RF bandwidth.

The cause of the problematic frequency locking could not be clearly contributed to the circuit implementation or faulty packaging. While the packaging can be improved without a full re-design of the TX and RX, it cannot be expected that this immediately solves the problem and makes higher data rates and QAM available. In previous MIMO implementations [56], similar effects of two concurrent constellations were observed caused by two independent LO generation paths in the receiver. By potentially reducing the here presented dual-polarized TX and RX to a single-polarized communication system, the influence of the LO power splitting can be isolated.

From a more global perspective, this dissertation opens up the exploration of communication systems operating close to 300 GHz using silicon technologies. However, the presented dissertation limits this exploration to the RF frontend without additional

implementations of baseband processing or on-chip LO generation/carrier recovery. For more practical prototypes, the baseband generation and demodulation should be integrated on the same chip [47], [105], [106]. In a similar direction, the LO generation is dependent on broadband signal generators. In this dissertation, this feature is required to show that the TX and RX can operate for different LO frequencies over a wide frequency range. An on-chip LO generation would limit the carrier allocation.

In Chapter 3, it was briefly discussed that frequency and phase locking is necessary for optimum communication link conditions. Again here, the implementation of phase-locked loops would limit the LO frequency generation to the locking range of the PLL while a costas loop limits the operation to BPSK/QPSK modulation. As a potential step for improved phase-locking, a LO phase shifter with continous 360°phase resolution was proposed in Chapter 3. Such phase shifters could potentially also be used for in-air signal combination in the form of phased array and allow beam-steering to facilitate the TX and RX alignment in highly directive communication links.

Overall, the presented transmitter and receiver demonstrate that silicon-integrated communication will be possible at 300 GHz. While the current implementation is limited by the packaging and RX baseband implementation, the achieved frequency upconversion and downconversion show the feasibility of communication in this frequency range. The implemented frequency multiplier stages as well as the power amplifier with their measured 3-dB bandwidth exceeding 60 GHz show the potential for broadband circuits, while the transmitted output power and achieved SNR >20 dB implies that the communication link will not be SNR-limited for future operation. The TIA simulates without the implemented baseband routing also indicates that the active circuits in the RX and TX will exceed the performance set by the previous generation of silicon-based communication systems operating at 240 GHz.

Bibliography

Own Publications

[own1] T. Bucher, J. Grzyb, P. Hillger, H. Rucker, B. Heinemann, and U. R. Pfeiffer, "A Broadband 300 GHz Power Amplifier in a 130 nm SiGe BiCMOS Technology for Communication Applications," *IEEE Journal of Solid-State Circuits*, vol. 57, no. 7, pp. 2024–2034, Jul. 2022.

[own2] M. M. Tarar, T. Beucher, S. Qayyum, and R. Negra, "Efficient 2–16 GHz flat-gain stacked distributed power amplifier in 0.13µm CMOS using uniform distributed topology," in *2017 IEEE MTT-S International Microwave Symposium (IMS)*, IEEE, Jun. 2017.

[own3] T. Bücher, J. Grzyb, P. Hillger, H. Rücker, B. Heinemann, and U. R. Pfeiffer, "A 239–298 GHz Power Amplifier in an Advanced 130 nm SiGe BiCMOS Technology for Communications Applications," in *ESSCIRC 2021 - IEEE 47th European Solid State Circuits Conference (ESSCIRC)*, IEEE, Sep. 2021.

[own4] S. Malz, P. Hillger, T. Bücher, R. Jain, and U. R. Pfeiffer, "A 108 GHz Up-Conversion Mixer in 22 nm FDSOI," in *2020 German Microwave Conference (GeMiC)*, 2020, pp. 84–87.

[own5] T. Buecher, S. Malz, K. Aufinger, and U. R. Pfeiffer, "A 210–291-GHz (8x) Frequency Multiplier Chain With Low Power Consumption in 0.13-μm SiGe," *IEEE Microwave and Wireless Components Letters*, pp. 1–4, 2020.

[own6] A. Chandra Prabhu, P. Hillger, J. Grzyb, T. Bücher, H. Rücker, and U. R. Pfeiffer, "A 300 GHz x9 Multiplier Chain With 9.6 dBm Output Power in SiGe Technology," in *2024 IEEE Radio & Wireless Week (RWW)*, IEEE, Jan. 2024.

Cited References

[1] "Ericsson Mobility Report," Telefonaktiebolaget LM Ericsson, Tech. Rep., 2023.

[2] "6G The Next Hyper-Connected Experience for All," Samsung, Tech. Rep., May 2020.

[3] M. Fujishima, "Key Technologies for THz Wireless Link by Silicon CMOS Integrated Circuits," *Photonics*, vol. 5, no. 4, p. 50, Nov. 2018.

[4] "IEEE standard for high data rate wireless multi-media networks–amendment 2: 100 Gb/s wireless switched point-to-point physical layer," *IEEE Std 802.15.3d-2017 (Amendment to IEEE Std 802.15.3-2016 as amended by IEEE Std 802.15.3e-2017)*, pp. 1–55, Oct. 2017.

[5] H. Wang, K. Choi, B. Abdelaziz, *et al.*, *Power Amplifiers Performance Survey 2000-Present*, 2023.

[6] P. Rodrıguez-Vázquez, J. Grzyb, B. Heinemann, and U. R. Pfeiffer, "A 16-QAM 100 Gbps 1-Meter Wireless Link at 230 GHz with an EVM of 17% in a SiGe Technology," *IEEE Microwave and Wireless Components Letters*, 2019.

[7] M. H. Eissa, A. Malignaggi, and D. Kissinger, "A 13.5-dBm 200–255-GHz 4-Way Power Amplifier and Frequency Source in 130-nm BiCMOS," *IEEE Solid-State Circuits Letters*, vol. 2, no. 11, pp. 268–271, Nov. 2019.

[8] X. Li, W. Chen, P. Zhou, Y. Wang, F. Huang, S. Li, J. Chen, and Z. Feng, "A 250-310 GHz Power Amplifier with 15-dB Peak Gain in 130-nm SiGe BiCMOS Process for Terahertz Wireless System," *IEEE Trans. THz Sci. Technol. Transactions on Terahertz Science and Technology*, pp. 1–1, 2021.

[9] H. Li, J. Chen, D. Hou, Z. Li, P. Zhou, and W. Hong, "A 230-GHz SiGe Amplifier With 21.8-dB Gain and 3-dBm Output Power for Sub-THz Receivers," *IEEE Microw. Wireless Compon. Lett. Microwave and Wireless Components Letters*, vol. 31, no. 8, pp. 1004–1007, Aug. 2021.

[10] D. Yoon, M.-G. Seo, K. Song, M. Kaynak, B. Tillack, and J.-S. Rieh, "260-GHz differential amplifier in SiGe heterojunction bipolar transistor technology," *Electronics Letters*, vol. 53, no. 3, pp. 194–196, 2017.

[11] H. Bameri and O. Momeni, "An Embedded 200 GHz Power Amplifier with 9.4 dBm Saturated Power and 19.5 dB Gain in 65 nm CMOS," in *2020 IEEE Radio Frequency Integrated Circuits Symposium (RFIC)*, IEEE, Aug. 2020.

[12] S. Ghosh, F. Zhang, H. Guo, and K. K. O, "305-GHz Cascode Power Amplifier Using Capacitive Feedback Fabricated Using SiGe HBT's with fmax of 450 GHz," in *2023 IEEE Radio Frequency Integrated Circuits Symposium (RFIC)*, IEEE, Jun. 2023.

[13] R. Zhou, J. Chen, Z. Li, J. Yu, D. Tang, and W. Hong, "A 260-GHz Power Amplifier With 12.5-dBm P_{sat} and 21.4-dB Peak Gain Utilizing a Modified Coupled-Line-Balun Network," *IEEE Transactions on Microwave Theory and Techniques*, pp. 1–15, 2023.

[14] Z. Li, J. Chen, H. Li, Z. Wang, D. Hou, P. Yan, Z. Chen, and W. Hong, "A 220-GHz Power Amplifier with 22.5-dB Gain and 9-dBm Psat in 130-nm SiGe," vol. 31, no. 10, pp. 1166–1169, Aug. 2021.

[15] S. Hara, K. Katayama, K. Takano, *et al.*, "A 32Gbit/s 16QAM CMOS receiver in 300GHz band," in *2017 IEEE MTT-S International Microwave Symposium (IMS)*, IEEE, Jun. 2017.

[16] S. Lee, S. Hara, T. Yoshida, S. Amakawa, R. Dong, A. Kasamatsu, J. Sato, and M. Fujishima, "An 80-Gb/s 300-GHz-Band Single-Chip CMOS Transceiver," *IEEE Journal of Solid-State Circuits*, vol. 54, no. 12, pp. 3577–3588, Dec. 2019.

[17] D. Fritsche, P. Stärke, C. Carta, and F. Ellinger, "A Low-Power SiGe BiCMOS 190-GHz Transceiver Chipset With Demonstrated Data Rates up to 50 Gbit/s Using On-Chip Antennas," vol. 65, no. 9, pp. 3312–3323, Sep. 2017.

[18] S. Hara, K. Katayama, K. Takano, *et al.*, "A 32Gbit/s 16QAM CMOS Receiver in 300GHz Band," in *2017 IEEE MTT-S International Microwave Symposium (IMS)*, Jun. 2017, pp. 1703–1706.

[19] P. Rodrıguez-Vázquez, J. Grzyb, B. Heinemann, and U. R. Pfeiffer, "Performance Evaluation of a 32-QAM 1-Meter Wireless Link Operating at 220–260 GHz with a Data-Rate of 90 Gbps," in *2018 Asia-Pacific Microwave Conference (APMC)*, Nov. 2018, pp. 723–725.

[20] M. H. Eissa, A. Malignaggi, R. Wang, M. Elkhouly, K. Schmalz, A. C. Ulusoy, and D. Kissinger, "Wideband 240-GHz Transmitter And Receiver in BiCMOS Technology With 25-Gbit/s Data Rate," pp. 1–11, 2018.

[21] P. Rodriguez-Vazquez, J. Grzyb, N. Sarmah, B. Heinemann, and U. R. Pfeiffer, "A 65 Gbps QPSK one meter wireless link operating at a 225–255 GHz tunable carrier in a SiGe HBT technology," in *IEEE Radio and Wireless Symp.*, Anaheim, CA, USA, 2018, pp. 146–149.

[22] V.-S. Trinh, J.-M. Song, and J.-D. Park, "A 260–300-GHz Mixer-First IQ Receiver With Fundamental LO Driver in 130-nm SiGe Process," *IEEE Microwave and Wireless Technology Letters*, vol. 33, no. 4, pp. 435–438, Apr. 2023.

[23] J.-M. Song, V.-S. Trinh, S. Kim, and J.-D. Park, "275 GHz Quadrature Receivers for THz-Band 6G Indoor Network in 130-nm SiGe Technology," *IEEE Access*, vol. 11, pp. 138 540–138 548, 2023.

[24] C. Shannon, "Communication in the Presence of Noise," *Proceedings of the IRE*, vol. 37, no. 1, pp. 10–21, Jan. 1949.

[25] A. Georgiadis, "Gain, Phase Imbalance, and Phase Noise Effects on Error Vector Magnitude," vol. 53, no. 2, pp. 443–449, Mar. 2004.

[26] H. Mahmoud and H. Arslan, "Error vector magnitude to SNR conversion for nondata-aided receivers," *IEEE Transactions on Wireless Communications*, vol. 8, no. 5, pp. 2694–2704, May 2009.

[27] B. Razavi, "Design considerations for direct-conversion receivers," vol. 44, no. 6, pp. 428–435, Jun. 1997.

[28] H. T. Friis, "Noise Figures of Radio Receivers," *Proceedings of the IRE*, vol. 32, no. 7, pp. 419–422, Jul. 1944.

[29] Y. Mao, K. Schmalz, J. Borngraber, and J. C. Scheytt, "245-GHz LNA, Mixer, and Subharmonic Receiver in SiGe Technology," *IEEE Transactions on Microwave Theory and Techniques*, vol. 60, no. 12, pp. 3823–3833, Dec. 2012.

[30] K. Schmalz, J. Borngraber, Y. Mao, H. Rücker, and R. Weber, "A 245 GHz LNA in SiGe Technology," *IEEE Microwave and Wireless Components Letters*, vol. 22, no. 10, pp. 533–535, Oct. 2012.

[31] P. Stärke, D. Fritsche, C. Carta, and F. Ellinger, "A 24.7 dB low noise amplifier with variable gain and tunable matching in 130 nm SiGe at 200 GHz," in *2017 12th European Microwave Integrated Circuits Conference (EuMIC)*, Oct. 2017, pp. 5–8.

[32] M. Andree, J. Grzyb, B. Heinemann, and U. Pfeiffer, "A D-Band to J-Band Low-Noise Amplifier with High Gain-Bandwidth Product in an Advanced 130 nm SiGe BiCMOS Technology," in *2023 IEEE Radio Frequency Integrated Circuits Symposium (RFIC)*, IEEE, Jun. 2023.

[33] J. Grzyb, P. Rodriguez-Vazquez, S. Malz, M. Andree, and U. R. Pfeiffer, "A SiGe HBT 215–240 GHz DCS IQ TX/RX Chipset with Built-In Test of USB/LSB RF Asymmetry for 100+Gb/s Data Rates," Early Access, 2021.

[34] P. Rodriguez Vazquez, "6G Wireless Communication Links Operating at Frequencies beyond 200 GHz: an Analysis of their Performance and Main Limitations," en, 2022.

[35] M. Peffers, *Get Connected: Differential Signaling*, 2014.

[36] D. M. Pozar, *Microwave Engineering*. 111 River Street, Hoboken, New Jersey: Wiley, 2011.

[37] V. K. Tripathi, "Asymmetric Coupled Transmission Lines in an Inhomogeneous Medium," vol. 23, no. 9, pp. 734–739, Sep. 1975.

[38] R. Speciale, "Fundamental Even- and Odd-Mode Waves for Nonsymmetrical Coupled Lines in Non-Homogeneous Media," in *S-MTT International Microwave Symposium Digest*, MTT004, 1974.

[39] E. Cristal, "Coupled-Transmission-Line Directional Couplers with Coupled Lines of Unequal Characteristic Impedances," *IEEE Transactions on Microwave Theory and Techniques*, vol. 14, no. 7, pp. 337–346, Jul. 1966.

[40] C. Sharpe, "An Equivalence Principle for Nonuniform Transmission-Line Directional Couplers," *IEEE Transactions on Microwave Theory and Techniques*, vol. 15, no. 7, pp. 398–405, Jul. 1967.

[41] M. Steer, *Microwave and RF Design: Radio Systems, Volume 1*. NC State University, Jul. 2019.

[42] C. A. Balanis, *Antenna theory: analysis and design*. New York, NY, USA: Wiley, 2005.

[43] L. John, A. Tessmann, A. Leuther, P. Neininger, T. Merkle, and T. Zwick, "Broadband 300-GHz Power Amplifier MMICs in InGaAs mHEMT Technology," *Transactions on Terahertz Science and Technology*, vol. 10, no. 3, pp. 309–320, May 2020.

[44] H. Khatibi, S. Khiyabani, and E. Afshari, "A 173 GHz Amplifier With a 18.5 dB Power Gain in a 130 nm SiGe Process: A Systematic Design of High-Gain Amplifiers Above $f_{\max}/2$," *IEEE Transactions on Microwave Theory and Techniques*, vol. 66, no. 1, pp. 201–214, Jan. 2018.

[45] S. Ong, L. Chan, K. Chew, *et al.*, "22nm FD-SOI Technology with Back-biasing Capability Offers Excellent Performance for Enabling Efficient, Ultra-low Power Analog and RF/Millimeter-Wave Designs," in *2019 IEEE Radio Frequency Integrated Circuits Symposium (RFIC)*, IEEE, Jun. 2019.

[46] H.-J. Lee, S. Callender, S. Rami, W. Shin, Q. Yu, and J. M. Marulanda, "Intel 22nm Low-Power FinFET (22FFL) Process Technology for 5G and Beyond," in *2020 IEEE Custom Integrated Circuits Conference (CICC)*, IEEE, Mar. 2020.

[47] C. D'heer and P. Reynaert, "A Fully Integrated 135-GHz Direct-Digital 16-QAM Wireless and Dielectric Waveguide Link in 28-nm CMOS," *IEEE Journal of Solid-State Circuits*, pp. 1–, 2023.

[48] Y. Yang, O. D. Gurbuz, and G. M. Rebeiz, "An eight-element 370–410-GHz phased-array transmitter in 45-nm CMOS SOI with peak EIRP of 8–8.5 dBm," *IEEE Trans. THz Sci. Technol.*, vol. 64, no. 12, pp. 4241–4249, Dec. 2016.

[49] M. H. Eissa et al., "Frequency Interleaving IF Transmitter and Receiver for 240-GHz Communication in SiGe:C BiCMOS," vol. 68, no. 1, pp. 239–251, Jan. 2020.

[50] N. Sarmah, P. R. Vazquez, J. Grzyb, W. Foerster, B. Heinemann, and U. R. Pfeiffer, "A wideband fully integrated SiGe chipset for high data rate communication at 240 GHz," in *2016 11th European Microwave Integrated Circuits Conference (EuMIC)*, Oct. 2016, pp. 181–184.

[51] M. Elkhouly, Y. Mao, S. Glisic, C. Meliani, F. Ellinger, and J. C. Scheytt, "A 240 GHz direct conversion IQ receiver in 0.13 μm SiGe BiCMOS technology," in *2013 IEEE Radio Frequency Integrated Circuits Symposium (RFIC)*, IEEE, Jun. 2013, pp. 305–308.

[52] B. Heinemann, H. Rucker, R. Barth, *et al.*, "SiGe HBT with f_T/f_{max} of 505 GHz /720 GHz," in *IEEE Int. Electron Devices Meeting*, San Francisco, CA, USA, 2016, pp. 3.1.1–3.1.4.

[53] H. Rücker and B. Heinemann, "Device Architectures for High-speed SiGe HBTs," in *2019 IEEE BiCMOS and Compound semiconductor Integrated Circuits and Technology Symposium (BCICTS)*, IEEE, Nov. 2019.

[54] Y. Zhang, W. Liang, X. Jin, M. Krattenmacher, S. Falk, P. Sakalas, B. Heinemann, and M. Schroter, "3.2-mW Ultra-Low-Power 173-207-GHz Amplifier With 130-nm SiGe HBTs Operating in Saturation," *IEEE J. Solid-State Circuits Journal of Solid-State Circuits*, pp. 1–11, 2020.

[55] N. Sarmah, K. Aufinger, R. Lachner, and U. R. Pfeiffer, "A 200-225 GHz SiGe Power Amplifier with peak P_{sat} of 9.6 dBm using wideband power combination," in *ESSCIRC Conference 2016: 42nd European Solid-State Circuits Conference*, Sep. 2016, pp. 193–196.

[56] P. Rodriguez-Vazquez, J. Grzyb, B. Heinemann, and U. R. Pfeiffer, "A QPSK 110 GB/S Polarization-Diversity MIMO Wireless Link with a 220–255 GHz Tunable LO in a SiGe HBT Technology," vol. 68, no. 9, pp. 3834–3851, Sep. 2020.

[57] D. Filipovic, S. Gearhart, and G. Rebeiz, "Double-slot antennas on extended hemispherical and elliptical silicon dielectric lenses," *IEEE Transactions on Microwave Theory and Techniques*, vol. 41, no. 10, pp. 1738–1749, 1993.

[58] J. Grzyb, K. Statnikov, N. Sarmah, and U. R. Pfeiffer, "A wideband 240 GHz lens-integrated circularly polarized on-chip annular slot antenna for a FMCW radar transceiver module in SiGe technology," in *SBMO/IEEE MTT-S Int. Microwave and Optoelectronics Conf.*, Porto de Galinhas, Brazil, Nov. 2015, pp. 1–4.

[59] B. Gilbert, "A Precise Four-Quadrant Multiplier with Subnanosecond Response," *IEEE Solid-State Circuits Newsletter*, vol. 12, no. 4, pp. 29–37, 2007.

[60] P. Rodriguez Vazquez, J. Grzyb, N. Sarmah, B. Heinemann, and U. Pfeiffer, "A 219–266 GHz LO-tunable direct-conversion IQ receiver module in a SiGe HBT technology," *Int. J. Microwave and Wireless Technologies*, vol. 10, no. 5–6, pp. 587–595, May 2018.

[61] N. Sarmah, J. Grzyb, K. Statnikov, S. Malz, P. Rodriguez Vazquez, W. Foerster, B. Heinemann, and U. R. Pfeiffer, "A fully integrated 240-GHz direct-conversion quadrature transmitter and receiver chipset in SiGe technology," *IEEE Trans. Microw. Theory Techn.*, vol. 64, no. 2, pp. 562–574, Feb. 2016.

[62] E. Sackinger, "The Transimpedance Limit," *IEEE Transactions on Circuits and Systems I: Regular Papers*, vol. 57, no. 8, pp. 1848–1856, Aug. 2010.

[63] E. Johnson, "Physical limitations on frequency and power parameters of transistors," in *1958 IRE International Convention Record*, vol. 13, New York, NY, USA, Mar. 1965, pp. 27–34.

[64] J. Cusack, S. Perlow, and B. Perlman, "Automatic Load Contour Mapping for Microwave Power Transistors," *IEEE Transactions on Microwave Theory and Techniques*, vol. 22, no. 12, pp. 1146–1152, Dec. 1974.

[65] N. Sarmah, P. Chevalier, and U. R. Pfeiffer, "160-GHz Power Amplifier Design in Advanced SiGe HBT Technologies With P_{sat} in Excess of 10 dBm," *IEEE Transactions on Microwave Theory and Techniques*, vol. 61, no. 2, pp. 939–947, Feb. 2013.

[66] H. Asada, K. Matsushita, K. Bunsen, K. Okada, and A. Matsuzawa, "A 60GHz CMOS power amplifier using capacitive cross-coupling neutralization with 16 % PAE," in *2011 6th European Microwave Integrated Circuit Conference*, Oct. 2011, pp. 554–557.

[67] D. Simic and P. Reynaert, "Analysis and Design of Lossy Capacitive Over-Neutralization Technique for Amplifiers Operating Near fMAX," *IEEE Transactions on Circuits and Systems I: Regular Papers*, vol. 68, no. 5, pp. 1945–1955, May 2021.

[68] J. Kim, C.-G. Choi, K. Lee, K. Kim, S.-U. Choi, and H.-J. Song, "Analysis and Design of Dual-Peak Gmax-Core CMOS Amplifier in D-Band Embedding a T-Shaped Network," in *2022 IEEE Radio Frequency Integrated Circuits Symposium (RFIC)*, IEEE, Jun. 2022.

[69] S. Sadlo, M. De Matos, A. Cathelin, and N. Deltimple, "One stage gain boosted power driver at 184 GHz in 28 nm FD-SOI CMOS," in *2021 IEEE Radio Frequency Integrated Circuits Symposium (RFIC)*, IEEE, Jun. 2021.

[70] H. Li, J. Chen, D. Hou, *et al.*, "A 250-GHz Differential SiGe Amplifier With 21.5-dB Gain for Sub-THz Transmitters," *IEEE Trans. THz Sci. Technol. Transactions on Terahertz Science and Technology*, vol. 10, no. 6, pp. 624–633, Nov. 2020.

[71] Y. Yoon, Y. Lu, R. Frye, M. Lau, P. Smith, L. Ahlquist, and D. Kossives, "Design and characterization of multilayer spiral transmission-line baluns," *IEEE Transactions on Microwave Theory and Techniques*, vol. 47, no. 9, pp. 1841–1847, 1999.

[72] H.-R. Ahn and M. M. Tentzeris, "Novel Generic Asymmetric and Symmetric Equivalent Circuits of 90°Coupled Transmission-Line Sections Applicable to Marchand Baluns," *IEEE Transactions on Microwave Theory and Techniques*, vol. 65, no. 3, pp. 746–760, Mar. 2017.

[73] C.-M. Tsai and K. C. Gupta, "A Generelized Model for Coupled Lines and its Applications to Two-Layer Planar Circuits," vol. 42, no. 12, pp. 2190–2199, Dec. 1992.

[74] K. Sachse, "The Scattering Paramters and Directional Coupler Analysis of Characteristically Terminated Asymmetric Coupled Transmission Lines in an Inhomogneous Medium," vol. 38, no. 4, pp. 417-425–739, Apr. 1990.

[75] D. Gunton and E. Paige, "An analysis of the general asymmetric directional coupler with non-mode-converting terminations," *IEE J. Microw. Opt. Acoust. UK Journal on Microwaves, Optics and Acoustics*, vol. 2, no. 1, p. 31, 1978.

[76] N. Sarmah, B. Heinemann, and U. R. Pfeiffer, "235-275 GHz (x16) frequency multiplier chains with up to 0 dBm peak output power and low DC power consumption," in *2014 IEEE Radio Frequency Integrated Circuits Symposium*, Jun. 2014, pp. 181–184.

[77] C. Bredendiek, N. Pohl, K. Aufinger, and A. Bilgic, "Differential signal source chips at 150 GHz and 220 GHz in SiGe bipolar technologies based on Gilbert-Cell frequency doublers," in *2012 IEEE Bipolar/BiCMOS Circuits and Technology Meeting (BCTM)*, Sep. 2012, pp. 1–4.

[78] S. Kueppers, K. Aufinger, and N. Pohl, "A fully differential 100-140 GHz frequency quadrupler in a 130 nm SiGe:C technology for MIMO radar applications using the bootstrapped Gilbert-Cell doubler topology," in *2017 IEEE 17th Topical Meeting on Silicon Monolithic Integrated Circuits in RF Systems (SiRF)*, Jan. 2017, pp. 37–39.

[79] V. Ries, C. Carta, and F. Ellinger, "Frequency Multiplication With Adjustable Waveform Shaping Demonstrated at 200 GHz," *IEEE Transactions on Microwave Theory and Techniques*, vol. 67, no. 4, pp. 1544–1555, Apr. 2019.

[80] S. Shopov, A. Balteanu, J. Hasch, P. Chevalier, A. Cathelin, and S. P. Voinigescu, "A 234–261-GHz 55-nm SiGe BiCMOS Signal Source with 5.4–7.2 dBm Output Power, 1.3% DC-to-RF Efficiency, and 1-GHz Divided-Down Output," *IEEE Journal of Solid-State Circuits*, vol. 51, no. 9, pp. 2054–2065, Sep. 2016.

[81] H. Lin and G. M. Rebeiz, "A SiGe Multiplier Array With Output Power of 5–8 dBm at 200–230 GHz," *IEEE Transactions on Microwave Theory and Techniques*, vol. 64, no. 7, pp. 2050–2058, Jul. 2016.

[82] A. Guner, T. Mausolf, J. Wessel, D. Kissinger, and K. Schmalz, "A 440–540-GHz Transmitter in 130-nm SiGe BiCMOS," *IEEE Microwave and Wireless Components Letters*, vol. 31, no. 6, pp. 779–782, Jun. 2021.

[83] E. Öjefors, B. Heinemann, and U. R. Pfeiffer, "Active 220- and 325-GHz Frequency Multiplier Chains in an SiGe HBT Technology," *IEEE Transactions on Microwave Theory and Techniques*, vol. 59, no. 5, pp. 1311–1318, May 2011.

[84] A. Chandra-Prabhu, J. Grzyb, P. Hillger, B. Heinemann, H. Rücker, and U. Pfeiffer, "A Wideband W-Band Frequency Tripler With a Novel Mode-Selective Filter for High Harmonic Rejection," in *2023 18th European Microwave Integrated Circuits Conference (EuMIC)*, IEEE, Sep. 2023.

[85] U. Madhow, *Introduction to Communication Systems*. Cambridge University Press, Nov. 2014.

[86] M. Seo, M. Urteaga, M. Rodwell, and M.-J. Choe, "A 300 GHz PLL in an InP HBT technology," in *2011 IEEE MTT-S International Microwave Symposium*, IEEE, Jun. 2011.

[87] P. Y. Chiang, Z. Wang, O. Momeni, and P. Heydari, "A 300GHz frequency synthesizer with 7.9% locking range in 90nm SiGe BiCMOS," in *Digest of Technical Papers - IEEE International Solid-State Circuits Conference*, 2014.

[88] S. Lee, S. Hara, R. Dong, K. Takano, S. Amakawa, T. Yoshida, and M. Fujishima, "A 272-GHz CMOS Analog BPSK/QPSK Demodulator for IEEE 802.15.3d," in *ESSCIRC 2021 - IEEE 47th European Solid State Circuits Conference (ESSCIRC)*, IEEE, Sep. 2021.

[89] Y. Kim, S. Kim, I. Lee, M. Urteaga, and S. Jeon, "A 220–320-GHz Vector-Sum Phase Shifter Using Single Gilbert-Cell Structure With Lossy Output Matching," *IEEE Trans. Microwave Theory Techn. Transactions on Microwave Theory and Techniques*, vol. 63, no. 1, pp. 256–265, Jan. 2015.

[90] T. Hirota, A. Minakawa, and M. Muraguchi, "Reduced-size branch-line and rat-race hybrids for uniplanar MMIC's," *IEEE Trans. Microwave Theory Techn. Transactions on Microwave Theory and Techniques*, vol. 38, no. 3, pp. 270–275, Mar. 1990.

[91] V. Petrov, T. Kurner, and I. Hosako, "IEEE 802.15.3d: First Standardization Efforts for Sub-Terahertz Band Communications toward 6G," *IEEE Commun. Mag. Communications Magazine*, vol. 58, no. 11, pp. 28–33, Nov. 2020.

[92] R. Al Hadi, H. Sherry, J. Grzyb, *et al.*, "A 1 k-pixel video camera for 0.7–1.1 terahertz imaging applications in 65-nm CMOS," *IEEE J. Solid-State Circuits*, vol. 47, no. 12, pp. 2999–3012, Dec. 2012.

[93] U. R. Pfeiffer, Y. Zhao, J. Grzyb, R. Al Hadi, N. Sarmah, W. Förster, H. Rücker, and B. Heinemann, "A 0.53 THz reconfigurable source module with up to 1 mW radiated power for diffuse illumination in terahertz imaging applications," *IEEE J. Solid-State Circuits*, vol. 49, no. 12, pp. 2938–2950, Dec. 2014.

[94] E. Hammerstad and O. Jensen, "Accurate Models for Microstrip Computer-Aided Design," in *MTT-S International Microwave Symposium Digest*, MTT006.

[95] P. Rodrıguez-Vázquez, J. Grzyb, N. Sarmah, B. Heinemann, and U. R. Pfeiffer, "Towards 100 Gbps: A Fully Electronic 90 Gbps One Meter Wireless Link at 230 GHz," in *2018 48th European Microwave Conference (EuMiC)*, Sep. 2018, pp. 1389–1392.

[96] J. Grzyb, P. Rodriguez-Vazquez, S. Malz, M. Andree, and U. R. Pfeiffer, "A SiGe HBT 215–240 GHz DCA IQ TX/RX Chipset With Built-In Test of USB/LSB RF Asymmetry for 100+ Gb/s Data Rates," *IEEE Transactions on Microwave Theory and Techniques*, vol. 70, no. 3, pp. 1696–1714, Mar. 2022.

[97] Y. Tao and F. Scharf, "Revisiting the Effect of Nickel Characteristics on High-Speed Interconnect Performance," *IEEE Transactions on Microwave Theory and Techniques*, vol. 64, no. 8, pp. 2447–2453, 2016.

[98] S. V. Thyagarajan, S. Kang, and A. M. Niknejad, "A 240 GHz fully integrated wideband QPSK receiver in 65 nm CMOS," *IEEE J. Solid-State Circuits*, vol. 50, no. 10, pp. 2268–2280, Oct. 2015.

[99] U. Alakusu, M. S. Dadash, S. Shopov, P. Chevalier, A. Cathelin, and S. P. Voinigescu, "A 210–284-GHz I–Q Receiver With On-Chip VCO and Divider Chain," *IEEE Microwave and Wireless Components Letters*, vol. 30, no. 1, pp. 50–53, Jan. 2020.

[100] Z. Li, J. Chen, H. Li, J. Yu, Y. Lu, R. Zhou, Z. Chen, and W. Hong, "A 220-GHz Sliding-IF Quadrature Transmitter and Receiver Chipset for High Data Rate Communication in 0.13-μ m SiGe BiCMOS," *IEEE Journal of Solid-State Circuits*, vol. 58, no. 7, pp. 1913–1927, Jul. 2023.

[101] C. Jiang, A. Cathelin, and E. Afshari, "A high-speed efficient 220-GHz spatial-orthogonal ASK transmitter in 130-nm SiGe BiCMOS," vol. 52, no. 9, pp. 2321–2334, Sep. 2017.

[102] K. Takano, S. Amakawa, K. Katayama, *et al.*, "A 105Gb/s 300GHz CMOS Transmitter," in *2017 IEEE International Solid-State Circuits Conference (ISSCC)*, Feb. 2017, pp. 308–309.

[103] S. Kang, S. V. Thyagarajan, and A. M. Niknejad, "A 240 GHz Fully Integrated Wideband QPSK Transmitter in 65 nm CMOS," vol. 50, no. 10, pp. 2256–2267, Oct. 2015.

[104] J. Yu, J. Chen, P. Zhou, Z. Li, H. Li, P. Yan, D. Hou, and W. Hong, "A 300-GHz Transmitter Front End With -4.1-dBm Peak Output Power for Sub-THz Communication Using 130-nm SiGe BiCMOS Technology," *IEEE Transactions on Microwave Theory and Techniques*, vol. 69, no. 11, pp. 4925–4936, Nov. 2021.

[105] S. Shopov, O. D. Gurbuz, G. M. Rebeiz, and S. P. Voinigescu, "A 13.2-dBm, 138-GHz I/Q RF-DAC with 64-QAM and OFDM free-space constellation formation," in *ESSCIRC 2017 - 43rd IEEE European Solid State Circuits Conference*, IEEE, Sep. 2017.

[106] O. Hanay, E. Bayram, S. Muller, M. Saeed, A. Hamed, and R. Negra, "Fourier-Domain DAC-Based Wireless Transmitter With Up To 2-GHz Modulation Bandwidth," *IEEE Transactions on Microwave Theory and Techniques*, vol. 69, no. 6, pp. 2870–2884, Jun. 2021.